Andrei-Viorel Man, BSc

Destructive quantum interference out of equilibrium

MASTER'S THESIS

to achieve the university degree of

Diplom-Ingenieur

Master's degree programme: Technical Physics

submitted to

Graz University of Technology

Supervisor

Univ.-Prof. Dipl.-Phys. Dr.rer.nat. Wolfgang von der Linden

Institute of Theoretical and Computational Physics

Graz, September 2019

AFFIDAVIT

I declare that I have authored this thesis independently, that I have not used other than the declared sources/resources, and that I have explicitly indicated all material which has been quoted either literally or by content from the sources used. The text document uploaded to TUGRAZonline is identical to the present master‘s thesis.

Date

Signature

Abstract

The trend of increasing processing power in combination with the reduction of the component's size in electronics requires the miniaturization of the individual electronic devices. This ongoing trend will eventually reach its limit when devices are downscaled to sizes at which quantum effects become dominating. Being small functional units, single molecules are considered as molecular electronic devices to further reduce this size limitation. Molecular electronics takes advantage of quantum effects yielding devices displaying certain desired properties.

The aim of this work is to study destructive quantum interference (DQI) which is a quantum effect that may be used in future electronic devices. We study DQI using benzenedithiolate (BDT) in two different configurations: benzene-1,3-dithiolate (meta-BDT) and benzene-1,4-dithiolate (para-BDT). For molecular electronics the electrodes play a crucial role. The impact of the electrodes on the transport properties is analyzed by considering two sets of electrodes: planar electrodes and pointed ones. Additionally, we drive these systems out of equilibrium by introducing bias voltage.

In the first step, we study DQI at the example of a Hückel model with parameters taken from literature to get an idea of how DQI affects the model system. Afterwards, we calculate transport properties of the different transport systems, e.g. the transmission, in and out of equilibrium by means of first-principles calculations using a density functional theory and non-equilibrium Green's function (DFT+NEGF) approach. In a further step, we map the Hamiltonian matrices generated in the DFT+NEGF approach onto simple models to gain a deeper understanding of DQI in BDT contacted with realistic electrodes in and out of equilibrium.

While DQI is observed in the Hückel model, different effects of the more realistic systems mask DQI. We find that additional transport channels not displaying DQI contribute to the electron transport. Also the electrode coupling is important for observing DQI. Our calculations also show that a bias voltage up to 3 V does not destroy DQI.

Kurzfassung

Der Trend zunehmender Prozessorleistung in Kombination mit der Reduktion der Komponentengröße in der Elektronik erfordert das Miniaturisieren der einzelnen elektronischen Bauteile. Dieser Trend wird letztendlich seine Grenzen erreichen, sobald Bauteile Größen erreicht haben, bei welchen quantenmechanische Effekte dominant werden. Einzelne Moleküle, welche kleine funktionale Einheiten darstellen, werden als elektronische Bauteile in Betracht gezogen, um diese Größenlimitation weiter zu reduzieren. Molekularelektronik nutzt das Auftreten solcher quantenmechanischer Effekte aus, um elektronische Komponenten mit bestimmten Eigenschaften zu erhalten.

Ziel dieser Arbeit ist es, destruktive Quanteninterferenz (DQI) zu untersuchen, welche ein Beispiel eines solchen quantenmechanischen Effektes darstellt, welcher in zukünftigen elektronischen Geräten Anwendung finden könnte. Wir untersuchen DQI anhand von Benzoldithiolat (BDT) in unterschiedlichen Konfigurationen: Benzol-1,3-dithiolat (meta-BDT) und Benzol-1,4-dithiolat (para-BDT). In der Molekularelektronik spielen die Elektroden eine entscheidende Rolle. Der Einfluss der Elektroden auf die Transporteigenschaften wird untersucht, indem zwei Elektrodenformen betrachtet werden: flache und spitze Elektroden. Zusätzlich bringen wir diese Systeme durch Anlegen einer Biasspannung ins Nichtgleichgewicht.

Zunächst untersuchen wir DQI am Beispiel eines Hückel Modells mit Parametern aus der Literatur, um eine Vorstellung der Auswirkungen von DQI auf das Modellsystem zu bekommen. Danach berechnen wir Transporteigenschaften der verschiedenen Transportsysteme wie z.B. die Transmission mithilfe von first-principles Berechnungen unter Verwendung von Dichtefunktionaltheorie und Greenscher Funktionen (DFT+NEGF) im Gleichgewicht und Nichtgleichgewicht. In einem weiteren Schritt projizieren wir die mit der DFT+NEGF Methode gewonnenen Hamiltonmatrizen auf Modellsysteme, welche wir studieren, um ein tieferes Verständnis von DQI in BDT kontaktiert an realistische Elektroden im Gleichgewicht und Nichtgleichgewicht zu erhalten.

Während DQI in einem Hückel-Modell beobachtet wird, überlagern verschiedene Effekte eines realistischen Systems DQI. Wir finden, dass zusätzliche Transportkanäle, welche keine DQI aufweisen, zum Elektronentransport beitragen. Außerdem ist die Kopplung der Elektroden wichtig für die Beobachtung von DQI. Unsere Berechnungen zeigen außerdem, dass eine Biasspannung bis zu 3 V die DQI nicht zerstört.

Acknowledgements

I want to thank my supervisor Prof. Dr. Wolfgang von der Linden and Michael Rumetshofer for introducing me to this topic and their dedication in helping me to understand and interpret the results. I also want to thank them for the guidance and also giving me the possibility to pursue my own ideas. A special thanks goes to Michael, who devoted time and effort in helping me to understand and apply the DFT code and also provided parts of the transport code.

I also want to thank Alexander Schossmann for many productive discussions, which opened new perspectives on different topics due to the different approaches in tackling the same problem.

Many thanks also go to Andreas Hirczy, who helped me accessing the computer resources and dealing with technical problems, and Brigitte Schwarz, who helped me with bureaucratic matters whenever possible.

My thanks go also to my colleagues and friends at university, who often ensured a good mood and made the workday fun, especially Alexander Schossmann and Rene Vötter, who created a good working climate in the office.

But most of all I want to thank my parents and my sister, who supported me all along, encouraged me to follow my goals and helped me whenever possible. I want to thank my relatives and friends too, who encouraged and motivated me during all this time.

Contents

Chapter 1

Introduction

Theoretical studies show that various molecules can in principle display properties of a wide variety of electronic components like switches, diodes or transistors [1]. As an impressive example, *Stadler et al.* [2] showed that, by taking advantage of destructive quantum interference (DQI), XOR gates, AND gates and even half-adders could be created out of a single dinitrobenzene molecule. The 1,3-dinitrobenzene shown in Fig. 1.1 results in a XOR gate if electrodes are contacted to the carbon atoms at positions *2* and *4*. The inputs *0/1* correspond to the nitro groups (NO_2) being either in-plane with the benzene ring or perpendicular to this plane, respectively. If either both or none of the two NO_2 groups are in-plane with the benzene ring the system will display DQI. In the case of DQI there will be a lower current flow (output *0*) and in the case of no DQI there will be a larger current flow (output *1*). A half-adder is realized by contacting a third electrode at position *5* and an AND gate by using two electrodes contacted to 1,2-dinitrobenzene at sites *4* and *5*.

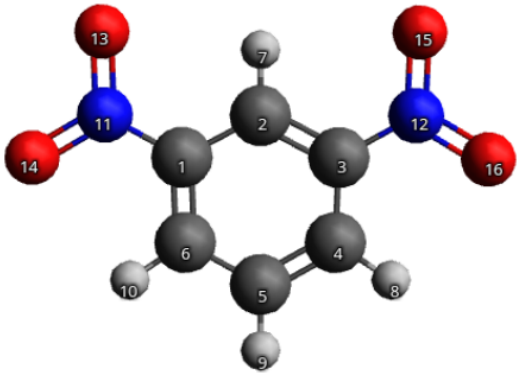

Fig. 1.1. 1,3-dinitrobenzene.
The molecule is drawn with Avogadro [3].
Color code: carbon (gray), hydrogen (white), nitrogen (blue), oxygen (red).

An example of an even simpler molecule displaying DQI is benzene, where the observation of DQI is determined by the sites the electrodes are contacted to. Unfortunately, benzene is unsuited in molecular electronic devices for several reasons, e.g. the Fermi energy lying in the middle of the large HOMO-LUMO gap. Due to benzene being unsuited in molecular electronic devices its derivatives, like benzenedithiolate, are considered instead. Using 1,4-benzenedithiolate (BDT), a molecular transport system has been realized in 1997 [4]. Meanwhile, BDT has been investigated extensively experimentally and theoretically.

To deduce whether a given molecule, like dinitrobenzene or BDT, has the properties necessary to serve as a replacement of a specific electronic component quantum mechanical calculations can be done. For solving the underlying equation, the time-independent Schrödinger equation, in a reasonable amount of CPU time, approximations are unavoidable. State-of-the-art methods like density functional theory combined with non-equilibrium Green's functions (DFT+NEGF) can be used to predict tendencies of physically relevant properties quite well, e.g. Ref. [5]. In general these methods are computationally expensive and do not always allow for simple physical interpretations.

To reduce the computational cost one can resort to models that describe the relevant physics reliably. By limiting oneself to the Hückel model, a graphical scheme can be derived [6] allowing the prediction of DQI through visual assessment of a molecule's conjugated π orbitals: In the first step one draws a graphical representation of the molecule's conjugated π orbitals. Then two electrodes are contacted at a single site each. For predicting DQI one needs, for all possible combinations, to connect the two sites of the molecule contacted to the electrodes by a continuous path and group nearest-neighboring sites not part of this path into loops or pairs, where each site can be part of a single loop or pair. If none of the possible paths allows the grouping of all sites in this manner, DQI occurs. Fig. 1.2 shows the application of this scheme.

Fig. 1.2. Two diagrams resulting from the application of the graphical scheme discussed in the main text to a benzene molecule. The stars indicate the sites contacted to the electrodes.

Although this graphical scheme holds only in the case of the Hückel model, it has been applied also for molecules not describable by the Hückel model, in many cases predicting the occurrence of DQI correctly. Using this scheme, one can show that the logical circuits mentioned above and proposed by Stadler et al. [2] display the desired properties. When the NO_2 groups are in-plane with the carbon ring, they are conjugated to the π orbitals of the benzene ring and have to be paired together with the carbon atoms according to above scheme. By rotating one nitro group by 90° about the CN-bond, the nitrogen of this functional group is no longer conjugated and therefore must not be paired with the carbon atoms. Also DQI in the case of benzene can be determined using this graphical scheme (see Fig.1.2).

Model parameters depend strongly on the environment of a system and the geometric details of the molecule, which leads to limiting transferability. Therefore, in this thesis, we study the transmission of the four systems shown in Fig. 1.3 separately and for different bias voltages using the DFT+NEGF code TRANSIESTA [7,8] and its post-processing tool TBTRANS [8]. We use the parameters gained from these calculations to obtain models containing different approximations, e.g. Hückel model or tight-binding model, and examine the impact of approximations on the DQI. We compare the results obtained from the different models to each other as well as to the results from the first-principles calculations.

This thesis is structured as follows: Chapter 2 addresses the theory required for the different calculations. In chapter 3, we discuss the codes used for the first-principles calculations and the approximations in the models. In Chapter 4, we present the results gained from the DFT calculations and the different models.

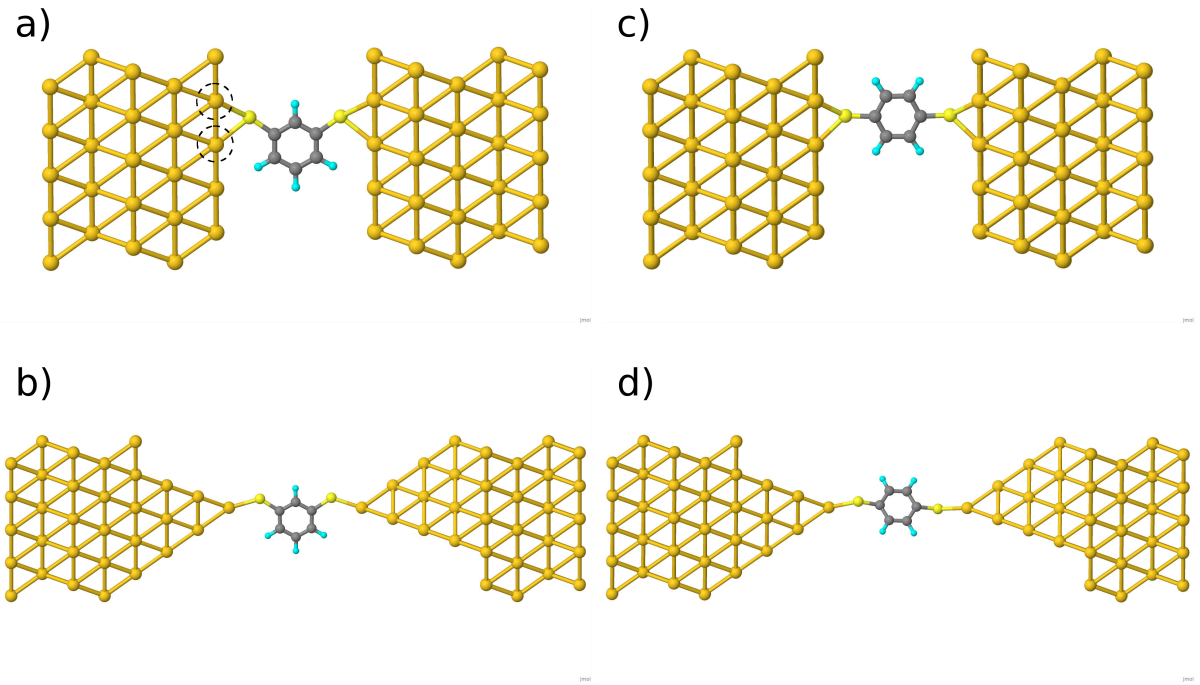

Fig. 1.3. Central regions of the studied transport systems:
(**a**) benzene-1,3-dithiolate contacted to planar electrodes
(**b**) benzene-1,3-dithiolate contacted to pointed electrodes
(**c**) benzene-1,4-dithiolate contacted to planar electrodes
(**d**) benzene-1,4-dithiolate contacted to pointed electrodes
The BDT is contacted to Au(111). In the case of planar electrodes the sulfur is positioned on the fcc hollow site as indicated by the dotted circles in (**a**). The tips of the pointed electrodes lie on a line parallel to the transport direction. The systems were built with Avogadro [3] and drawn with Jmol [9].
Color code : Carbon (gray), Hydrogen (cyan), sulfur (yellow), gold (gold).

Chapter 2

Theory

In this chapter we address the theoretical concepts required to simulate transport systems. Sec. 2.1 describes how systems are calculated using DFT. We introduce the Hamiltonian in second quantization in Sec. 2.2 and discuss several approximations. In Sec. 2.3 we introduce the concept of Green's functions and derive their connection to the Hamiltonian. We discuss in Sec. 2.4 a formalism allowing the treatment of infinitely extended systems. In Sec. 2.5 we explain how transport systems are driven out of equilibrium. Additionally, Sec. 2.6 will treat the derivation of the graphical scheme and show how using this scheme DQI can be predicted through visual assessment.

2.1 Density Functional Theory

On the scale of molecular transport systems classical physics breaks down and is no longer applicable. For a correct description of these systems the Schrödinger equation has to be solved. Time-independent non-relativistic systems are described by the time-independent Schrödinger equation

$$\hat{H}\Psi(\mathbf{r}_1, ..., \mathbf{r}_\mathrm{N}, \mathbf{R}_1, ..., \mathbf{R}_\mathrm{M}) = E\Psi(\mathbf{r}_1, ..., \mathbf{r}_\mathrm{N}, \mathbf{R}_1, ..., \mathbf{R}_\mathrm{M}) \ , \tag{2.1}$$

where $\Psi(\mathbf{r}_1, ..., \mathbf{r}_\mathrm{N}, \mathbf{R}_1, ..., \mathbf{R}_\mathrm{M})$ is a many-body wavefunction and the $\mathbf{r}_\mathrm{i}$ and $\mathbf{R}_\mathrm{j}$ are the position vectors of the electrons and nuclei, respectively. The many-body Hamiltonian has the form

$$\begin{aligned}\hat{H} = &- \sum_i \frac{\hbar^2}{2m_\mathrm{e}} \Delta_i + \sum_{\substack{i,j \\ i<j}} V_\text{e-e}\left(|\mathbf{r}_i - \mathbf{r}_j|\right) - \sum_{i,A} V_\text{e-n}\left(|\mathbf{r}_i - \mathbf{R}_A|\right) \\ &- \sum_A \frac{\hbar^2}{2m_A} \Delta_A + \sum_{\substack{A,B \\ A<B}} V_\text{n-n}\left(|\mathbf{R}_A - \mathbf{R}_B|\right) \ . \end{aligned} \tag{2.2}$$

e denotes the electrons, while n denotes the nuclei. The first two terms describe the kinetic energy and the Coulomb repulsion of the electrons, while the fourth and the fifth term describe the kinetic energy and the Coulomb repulsion of the nuclei. The third term describes the Coulomb attraction between nuclei and electrons. Due to the large difference in mass, the nuclei move

slowly compared to the electrons and the fourth and last term in Eq. (2.2) can be neglected in the calculations of the electronic part of the many-body wavefunction. This is the so-called Born-Oppenheimer approximation.

The dimension of the Hilbert space of a many-body system grows exponentially. Therefore, solving directly Eq. (2.1) is computationally very demanding. To allow for the treatment of "larger" systems, one can consider the electron density of a system instead of its many-body wavefunction. Hohenberg and Kohn [10] showed that the ground state electron density of an arbitrary number of electrons, which interact with each other through Coulomb repulsion and move influenced by an external potential, determines this potential uniquely. The first term on the right-hand side of Eq. (2.2) describes the motion of the electrons, the second one the Coulomb repulsion between them and the third term can be interpreted as the external potential assumed in Ref. [10]. Now the ground state energy can be calculated from this electron density

$$\begin{aligned} E[n] &= \big\langle \Psi[n] \big| \left(-\sum_i \frac{\hbar^2}{2m_\mathrm{e}} \Delta_i - \sum_{i,A} V_{\text{e-n}} \left(|\mathbf{r}_i - \mathbf{R}_A| \right) + \sum_{\substack{i,j \\ i<j}} V_{\text{e-e}} \left(|\boldsymbol{r_i} - \boldsymbol{r_j}| \right) \right) \big| \Psi[n] \big\rangle \\ &= G[n] + \int v_\mathrm{ext}(\mathbf{r}) n(\mathbf{r}) d\mathbf{r} + \frac{1}{2} \int \int \frac{n(\mathbf{r}) n(\mathbf{r}')}{|\mathbf{r} - \mathbf{r}'|} d\mathbf{r} d\mathbf{r}' \,, \end{aligned} \tag{2.3}$$

where the functional $G[n]$ contains the kinetic and exchange-correlation energy of the electrons and is treated in more detail later on. The second term describes the influence of the external potential, i.e. the potential created by the nuclei, on the electrons. The last term describes the classical Coulomb energy of the electrons. As Ref. [10] shows, the minimization of the energy in Eq. (2.3) with respect to the electron density leads to the correct ground state electron density.

The formalism derived up to now simplifies the problem of finding a wavefunction of 3^N variables for solving the Schrödinger equation to finding an electron density of only 3 variables minimizing the energy functional. Using this formalism, Kohn and Sham [11] developed a way to calculate the ground state electron density of a system. In the first step, the functional G[n] is split into a term containing the kinetic energy of non-interacting electrons $T_\mathrm{S}[n]$ and an exchange-correlation term $E_\mathrm{xc}[n]$ resulting in the following expression for the energy functional

$$E[n] = T_\mathrm{S}[n] + E_\mathrm{xc}[n] + \int v_\mathrm{ext}(\mathbf{r}) n(\mathbf{r}) d\mathbf{r} + \frac{1}{2} \int \int \frac{n(\mathbf{r}) n(\mathbf{r}')}{|\mathbf{r} - \mathbf{r}'|} d\mathbf{r} d\mathbf{r}' \,. \tag{2.4}$$

To solve this equation we require suitable expressions for the kinetic energy of the non-interacting electrons $T_\mathrm{S}[n]$ and the exchange-correlation term $E_\mathrm{xc}[n]$. A wide variety of functionals exists for the exchange-correlation term $E_\mathrm{xc}[n]$ following different philosophies and approaches. The choice of the exchange-correlation functional depends on the system and the properties one wants to study. At this point, we refer the reader to the literature for more information on exchange-correlation functionals. It will be easier to give an expression for the kinetic energy term $T_\mathrm{S}[n]$ at a later point. Therefore we continue at this point without an explicit expression for the functional $T_\mathrm{S}[n]$. Due to the interest in the ground state electron density the functional derivative of the energy with respect to the electron density has to vanish

$$\frac{\delta E[n]}{\delta n} \stackrel{!}{=} 0 \,. \tag{2.5}$$

Using this condition Eq. (2.4) becomes

$$\frac{\delta T_{\mathrm{S}}[n]}{\delta n} + \underbrace{\frac{\delta E_{\mathrm{xc}}[n]}{\delta n}}_{=:v_{\mathrm{xc}}} + v_{\mathrm{ext}}(\mathbf{r}) + \underbrace{\int \frac{n(\mathbf{r}')}{|\mathbf{r}-\mathbf{r}'|} d\mathbf{r}'}_{=:v_{\mathrm{H}}} = \frac{\delta T_{\mathrm{S}}[n]}{\delta n} + \tilde{v}_{\mathrm{eff}}(\mathbf{r}) = 0 \,, \tag{2.6}$$

where the so-called exchange-correlation potential v_{xc}, the external potential v_{ext} and the so-called Hartree potential v_{H} are combined into an effective potential $\tilde{v}_{\mathrm{eff}}(\mathbf{r})$. We see from this equation, that the initial problem can be mapped onto a fictive system of non-interacting electrons moving within an effective potential $\tilde{v}_{\mathrm{eff}}(\mathbf{r})$. The functional derivative of $T_{\mathrm{S}}[n]$ in terms of this system of non-interacting electrons has the form

$$\frac{\delta T_{\mathrm{S}}[n]}{\delta n} = \sum_i \int d\mathbf{r}\ \psi_i^*(\mathbf{r}) \left(-\frac{\hbar}{2m_{\mathrm{e}}} \Delta \right) \psi_i(\mathbf{r}) \tag{2.7}$$

with $\psi_i(\mathbf{r})$ being the wavefunctions of these non-interacting electrons. The $\psi_i(\mathbf{r})$ and the electron density of the initial system are related by

$$\boxed{n(\mathbf{r}) = \sum_i |\psi_i(\mathbf{r})|^2} \,. \tag{2.8}$$

Now the Kohn-Sham equations of this system of non-interacting electrons have to be solved

$$\boxed{\hat{H}_{\mathrm{KS}} \psi_i(\mathbf{r}) = \left\{ -\frac{\hbar}{2m_{\mathrm{e}}} \Delta + \tilde{v}_{\mathrm{eff}}(\mathbf{r}) \right\} \psi_i(\mathbf{r}) = \varepsilon_i^{\mathrm{KS}} \psi_i(\mathbf{r})} \,, \tag{2.9}$$

where $\hat{H}_{\mathrm{KS}}$ is the Kohn-Sham Hamiltonian. The $\psi_i(\mathbf{r})$ are called Kohn-Sham wavefunctions and the $\varepsilon_i^{\mathrm{KS}}$ are the corresponding eigenenergies.

2.2 Tight-binding model

By introducing a suitable basis, we can write the Kohn-Sham Hamiltonian in second quantization, which in the case of a localized basis allows the usage of the tight-binding (TB) model. For more information on second quantization we refer the reader to the literature, e.g. Ref. [12]. A detailed treatment of the tight-binding model is found in Ref. [13].

We write now the Kohn-Sham Hamiltonian in second quantization and get

$$\boxed{\hat{H}_{\mathrm{KS}} = \sum_{i,j} t_{ij} \hat{a}_i^\dagger \hat{a}_j = \sum_{\substack{i,j \\ i \neq j}} t_{ij} \hat{a}_i^\dagger \hat{a}_j + \sum_i \underbrace{t_{ii}}_{\varepsilon_i} \underbrace{\hat{a}_i^\dagger \hat{a}_i}_{\hat{n}_i}} \tag{2.10}$$

with the parameters

$$t_{ij} = \int d\mathbf{r}\ \psi_i^*(\mathbf{r}) \left[-\frac{\hbar}{2m_\mathrm{e}} \Delta + \tilde{v}_\mathrm{eff}(\mathbf{r}) \right] \psi_j(\mathbf{r}) \quad . \tag{2.11}$$

The $\psi_i(\mathbf{r})$ and $\psi_j^*(\mathbf{r})$ are the Kohn-Sham wavefunctions and the $\hat{a}_i^\dagger$ and $\hat{a}_j$ are fermionic creation and annihilation operators, respectively, and fulfill the anticommutator relations

$$\begin{aligned} \{\hat{a}_i, \hat{a}_j^\dagger\} &= \delta_{ij} \\ \{\hat{a}_i, \hat{a}_j\} &= 0 \\ \{\hat{a}_i^\dagger, \hat{a}_j^\dagger\} &= 0 \,. \end{aligned} \tag{2.12}$$

In the second step in Eq. (2.10) we rearranged the Hamiltonian into a more common form. The first term on the right-hand side describes the hopping of electrons between different orbitals. The second term describes the onsite energy of the electrons in the corresponding orbital with $\hat{a}_i^\dagger \hat{a}_i = \hat{n}_i$ being the particle number operator.

In TB the electrons are assumed to be tightly bound to atoms and thus the t_{ij} are in general very small if the sites i and j are locally well separated. Therefore only up to the n-nearest neighbors are relevant, while the remaining terms in Eq. (2.10) are negligible. The TB Hamiltonian has the form

$$\boxed{\hat{H}_\mathrm{TB} = \sum_{\langle i,j \rangle_n} t_{ij} \hat{a}_i^\dagger \hat{a}_j + \sum_i \varepsilon_i \hat{n}_i} \,, \tag{2.13}$$

with $\langle i,j \rangle_n$ denoting the summation over the nearest to n-nearest neighbors.

In the case of hydrocarbons with delocalized π bonds we can further simplify Eq. (2.13) using the Hückel model. More details on the Hückel model are found in e.g. Ref [14]. The Hückel model considers only electrons within π orbitals (π electrons) explicitly and treats electrons within σ orbitals as an additional contribution to the potential the π electrons feel.

For the Hückel model to be reasonable the π-electron approximation [15] has to be justified. According to Ref. [15] the π-electron approximation is an especially good approximation for planar hydrocarbons, like benzene, limiting the Hückel model to planar or nearly planar systems. Furthermore, the Hückel model considers only nearest-neighbor hopping and assumes a single hopping parameter t and a single onsite energy ε and the Hamiltonian simplifies to

$$\boxed{\hat{H}_\mathrm{Hückel} = t \sum_{\langle i,j \rangle_1} \hat{a}_i^\dagger \hat{a}_j + \varepsilon \sum_i \hat{n}_i} \,. \tag{2.14}$$

2.2.1 Basis functions

To write the Hamiltonian in second quantization we have to introduce a suitable basis. Atomic or molecular orbitals are a natural choice. Molecular orbitals can be approximated using a linear

combination of atomic orbitals (LCAO)

$$\chi_r(\mathbf{r}) = \sum_i c_{ri}\phi_i(\mathbf{r}) \,, \tag{2.15}$$

where $\chi_r(\mathbf{r})$ are molecular orbitals and the $\phi_i(\mathbf{r})$ are atomic orbitals. Similarly, it is possible to approximate the atomic orbitals by a linear combination of basis functions, which allow an easier evaluation of the parameters t_{ij} in Eq. (2.10). By introducing such a basis the problem shifts from finding the eigenfunctions of the Hamiltonian to finding the coefficients of the basis functions. In the case of non-interacting electrons the eigenvalue problem can be written as a matrix equation of the form

$$\boxed{\mathbf{H}\vec{c} = E\mathbf{S}\vec{c}} \tag{2.16}$$

with the entries of the Hamiltonian matrix $\mathbf{H}$ being the parameters t_{ij}. $\mathbf{S}$ and $\vec{c}$ are the overlap matrix and coefficient vector of the introduced basis functions, respectively.

In general the overlap matrix will not be the identity matrix (non-orthogonal TB). The generalized eigenvalue problem (2.16) can be reduced to a standard one by transforming the basis, and in further consequence the Hamiltonian matrix accordingly,

$$\boxed{\mathbf{O}_{\mathrm{S}}^{\mathrm{L}}\mathbf{S}\mathbf{O}_{\mathrm{S}}^{\mathrm{R}} = \mathbf{I}} \,. \tag{2.17}$$

The transformation matrices $\mathbf{O}_{\mathrm{S}}^{\mathrm{L}}$ and $\mathbf{O}_{\mathrm{S}}^{\mathrm{R}}$ depend on the chosen orthogonalization scheme. An example of such a scheme is the Löwdin orthogonalization [16], where

$$\boxed{\mathbf{O}_{\mathrm{S}}^{\mathrm{L}} = \mathbf{O}_{\mathrm{S}}^{\mathrm{R}} = \mathbf{S}^{-\frac{1}{2}}} \,. \tag{2.18}$$

Such orthogonalization also has its drawbacks. Due to the mixing of orbitals belonging to different atoms the new orbitals are less localized. This generally requires the consideration of hopping processes towards additional neighbors. Moreover, the transformation matrices $\mathbf{O}_{\mathrm{S}}^{\mathrm{L}}$ and $\mathbf{O}_{\mathrm{S}}^{\mathrm{R}}$ depend on the details of the system's geometry, like interatomic distances, limiting the transferability between different systems.

2.3 Green's functions

Green's functions are a convenient tool for our purposes. Once the Green's function is obtained properties like correlations, particle currents, transmissions and densities of states can be accessed easily. Due to their importance we will give a short introduction to Green's functions in this section. The following concepts and Green's functions in general are treated in more details in Ref. [12].

Due to the presence of operators within different *quantum mechanical pictures* we will give a short overview of these pictures:

- Schrödinger picture: The time evolution occurs in the states. The operators are either constant in time or depend explicitly on time. Operators and states within the Schrödinger picture are denoted with a subscript S.

- Heisenberg picture: The time evolution occurs in the operators. The states are constant in time. Operators and states are generally denoted with a subscript H, but for a shorter notation we will leave out the subscript in the following if not necessary.

We also introduce the following notation for the commutator and anticommutator

$$\begin{aligned} \{A, B\} &= AB + BA \\ [A, B] &= AB - BA \, . \end{aligned}$$

The retarded and advanced Green's functions of two operators $\hat{A}$ and $\hat{B}$ in the case of fermions are defined as

$$G^{\mathrm{R}}_{AB}(t, t') := -i\Theta(t - t') \left\langle \left\{ \hat{A}(t), \hat{B}(t') \right\} \right\rangle \tag{2.19}$$

$$G^{\mathrm{A}}_{AB}(t, t') := +i\Theta(t' - t) \left\langle \left\{ \hat{A}(t), \hat{B}(t') \right\} \right\rangle \, . \tag{2.20}$$

The angle brackets appearing on the right-hand side of Eqs. (2.19) and (2.20) denote the expectation value of the anticommutator of the operators $\hat{A}$ and $\hat{B}$. $\Theta(t - t')$ is the Heaviside function, which is defined in the following way

$$\Theta(t - t') = \begin{cases} 1 & \text{if } \; t > t' \\ 0 & \text{if } \; t' > t \end{cases} \, . \tag{2.21}$$

The operators $\hat{A}$ and $\hat{B}$ are depicted in the Heisenberg picture and are defined as

$$\hat{A}(t) = \hat{U}_{\mathrm{S}}^{-1}(t, t_0) \hat{A}_{\mathrm{S}}(t) \hat{U}_{\mathrm{S}}(t, t_0) \, . \tag{2.22}$$

$\hat{U}_{\mathrm{S}}(t, t_0)$ is the time-evolution operator, which fulfills the relations

$$\begin{aligned} &\hat{U}_{\mathrm{S}}(t_0, t) = \hat{U}_{\mathrm{S}}^{\dagger}(t, t_0) = \hat{U}_{\mathrm{S}}^{-1}(t, t_0) \\ &\hat{U}_{\mathrm{S}}(t_0, t_0) = \hat{I} \\ &\hat{U}_{\mathrm{S}}(t, t_0) = \hat{U}_{\mathrm{S}}(t, t') \hat{U}_{\mathrm{S}}(t', t_0) \, . \end{aligned} \tag{2.23}$$

By using the time-ordering operator $\hat{T}$

$$\hat{T}\hat{A}(t)\hat{B}(t') = \begin{cases} \hat{A}(t)\hat{B}(t') & \text{if } t > t' \\ \hat{B}(t')\hat{A}(t) & \text{if } t' > t \end{cases} \tag{2.24}$$

the time-evolution operator can be written as

$$\hat{U}_{\mathrm{S}}(t, t_0) = \hat{T} e^{-\frac{i}{\hbar}\int_{t_0}^{t} dt' \hat{H}(t')} . \tag{2.25}$$

2.3.1 Matrix Green's functions

We use the definitions (2.19) and (2.20) and show in this section, that we can calculate the one-particle Green's functions of non-interacting electrons from the Hamiltonian matrix and overlap matrix of the system by

$$\mathbf{G}^{\mathrm{R/A}}(E) = \left[(E \pm i0^+)\mathbf{S} - \mathbf{H}\right]^{-1} \tag{2.26}$$

with 0^+ being a positive infinitesimal. The positive sign is chosen for retarded Green's functions and the negative sign for advanced Green's functions.

From here on we will use atomic units, in which $\hbar = m_{\mathrm{e}} = \mathrm{e} = 1$.

For simplicity we consider an orthonormal basis and generalize the results at the end to a non-orthonormal basis. In the case of an effective one-particle Hamiltonian, it is enough to study *one-particle Green's functions*, i.e. Green's functions of the operators

$$\hat{A}(t) = \hat{a}_j(t) \quad \text{and} \quad \hat{B}(t) = \hat{a}_l^\dagger(t) , \tag{2.27}$$

where $\hat{a}_j$ and $\hat{a}_l^\dagger$ are annihilation and creation operators at sites j and l, respectively.

In this work we will study only steady states, which are described by time-independent Hamiltonians. This allows us to write the Green's functions (2.19) and (2.20) in terms of a time difference instead of two distinct times and simplifies the following derivations.

In the case of a time-independent Hamiltonian the time-evolution operator (2.25) becomes

$$\hat{U}_{\mathrm{S}}(t, t_0) = e^{-i\hat{H}(t-t_0)} . \tag{2.28}$$

We also introduce the identity operator

$$\hat{I} = \sum_m \left|m\right\rangle\left\langle m\right| , \tag{2.29}$$

which is valid for any complete, orthonormal basis.

We use now Eqs. (2.28) and (2.29) and take advantage of the operators having no explicit time-dependency to write the expectation value of Eqs. (2.19) and (2.20) in terms of a time difference. We consider the first term of the anticommutator and get

$$\begin{aligned}\left\langle \hat{A}(t)\hat{B}(t')\right\rangle &= \frac{1}{Z}\sum_{n,m}\left\langle n|e^{-\beta\hat{H}}e^{i\hat{H}t}\hat{A}_{\mathrm{S}}e^{-i\hat{H}t}e^{i\hat{H}t'}\hat{B}_{\mathrm{S}}|m\right\rangle\left\langle m|e^{-i\hat{H}t'}|n\right\rangle \\ &= \frac{1}{Z}\sum_{n,m}\left\langle m|e^{-i\hat{H}t'}|n\right\rangle\left\langle n|e^{-\beta\hat{H}}e^{i\hat{H}t}\hat{A}_{\mathrm{S}}e^{-i\hat{H}t}e^{i\hat{H}t'}\hat{B}_{\mathrm{S}}|m\right\rangle \\ &= \frac{1}{Z}\sum_{m}\left\langle m|e^{-\beta\hat{H}}e^{-i\hat{H}t'}e^{i\hat{H}t}\hat{A}_{\mathrm{S}}e^{-i\hat{H}t}e^{i\hat{H}t'}\hat{B}_{\mathrm{S}}|m\right\rangle = \left\langle \hat{A}(t-t')\hat{B}\right\rangle , \end{aligned} \tag{2.30}$$

where $\beta = \frac{1}{k_{\mathrm{B}}T}$ with k_{B} being the Boltzmann constant and T the temperature. We used the third relation from Eq. (2.23) and that the density operator $\frac{e^{-\beta\hat{H}}}{Z}$ and the time-evolution operator commute. This calculation can be repeated for the second term of the anticommutator.

Using the result from Eq. (2.30) we write Eqs. (2.19) and (2.20) as functions of time differences

$$G^{\mathrm{R}}_{AB}(t,t') = G^{\mathrm{R}}_{AB}(t-t') = -i\Theta(t-t')\left\langle\left\{\hat{A}(t-t'),\hat{B}\right\}\right\rangle \tag{2.31}$$

$$G^{\mathrm{A}}_{AB}(t,t') = G^{\mathrm{A}}_{AB}(t-t') = +i\Theta(t'-t)\left\langle\left\{\hat{A}(t-t'),\hat{B}\right\}\right\rangle . \tag{2.32}$$

Without loss of generality we set $t' = 0$.

We are interested in the energy-dependent Green's function, which can be calculated from the time-dependent one by performing a Fourier transformation:

$$G^{\mathrm{R/A}}_{AB}(E) = \int_{-\infty}^{+\infty} dt\; G^{\mathrm{R/A}}_{AB}(t)e^{iEt} . \tag{2.33}$$

From now on, we limit ourselves to the retarded Green's function for the moment and consider the advanced Green's function later on.

The retarded and advanced Green's functions can be obtained in different ways. One way is the equation of motion method (EOM method). We differentiate Eq. (2.31) with respect to time and multiply it by i

$$\begin{aligned} i\frac{d}{dt}G^{\mathrm{R}}_{AB}(t) &= \frac{d\Theta(t)}{dt}\left\langle\left\{\hat{A}(t),\hat{B}\right\}\right\rangle + \Theta(t)\left\langle\left\{\frac{d\hat{A}(t)}{dt},\hat{B}\right\}\right\rangle \\ &= \delta(t)\left\langle\left\{\hat{A}(t),\hat{B}\right\}\right\rangle - i\Theta(t)\left\langle\left\{\left[\hat{A}(t),\hat{H}\right],\hat{B}\right\}\right\rangle \\ &= \delta(t)\left\langle\left\{\hat{A}(t),\hat{B}\right\}\right\rangle + G^{\mathrm{R}}_{[A,H]B}(t) , \end{aligned} \tag{2.34}$$

where we used Heisenberg's equation of motion for operators

$$i\frac{d\hat{A}_{\mathrm{H}}(t)}{dt} = [\hat{A}_{\mathrm{H}}(t), \hat{H}_{\mathrm{H}}] + i\left(\frac{\partial \hat{A}_{\mathrm{S}}}{\partial t}\right)_{\mathrm{H}} \tag{2.35}$$

to describe the derivative of the operator $\hat{A}(t)$. In our case $\hat{A}_{\mathrm{S}} = \hat{a}_j$ is time-independent and therefore its derivative with respect to time vanishes.

In the first step, we calculate the Fourier transformation of the term on the left-hand side of Eq. (2.34). To ensure convergence at the upper integration limit a positive infinitesimal δ has to be introduced, which we will send to zero at the end of the calculation. Now we integrate the left-hand side of Eq. (2.34) by parts and get

$$\begin{aligned}
&\lim_{\delta\to 0^+} \int_{-\infty}^{+\infty} dt\; i\frac{d}{dt} G^{\mathrm{R}}_{AB}(t) e^{i(E+i\delta)t} \\
&\quad = \lim_{\delta\to 0^+} \left[iG^{\mathrm{R}}_{AB}(t) e^{iEt} e^{-\delta t}\Big|_{-\infty}^{+\infty} + (E+i\delta) \int_{-\infty}^{+\infty} dt\; G^{\mathrm{R}}_{AB}(t) e^{i(E+i\delta)t} \right] \\
&\quad = \underbrace{\left(E + i0^+\right)}_{E^+} G^{\mathrm{R}}_{AB}(E^+) \,,
\end{aligned} \tag{2.36}$$

where the first term in the second line vanishes at the upper limit due to the introduced infinitesimal and at the lower one due to the Heaviside function. The Fourier transformation of the first term on the right-hand side of Eq. (2.34) gives

$$\int_{-\infty}^{+\infty} dt\; \delta(t) \Big\langle \Big\{ \hat{A}(t), \hat{B} \Big\} \Big\rangle e^{iEt} = \Big\langle \Big\{ \hat{A}(t), \hat{B} \Big\} \Big\rangle e^{iEt} \Big|_{t=0} = \Big\langle \Big\{ \hat{A}, \hat{B} \Big\} \Big\rangle \,. \tag{2.37}$$

The Fourier transformation of the last term on the right-hand side of Eq. (2.34) is per definition the Green's function in dependence of the energy. Nevertheless, we simplify this term before Fourier transforming it by limiting the operators to one-particle ones. We choose the operators $\hat{A}$ and $\hat{B}$ according to Eq. (2.27). Additionally, we will shorten the notation by denoting the one-particle Green's functions in the following way

$$G^{\mathrm{R}}_{a_i a_j^\dagger}(t) = G^{\mathrm{R}}_{ij}(t) \,. \tag{2.38}$$

Before evaluating the second term on the right-hand side of Eq. (2.34) we calculate the commutator of the annihilation operator and the Hamiltonian, in our case the Kohn-Sham Hamiltonian. We do so by using Eqs. (2.10) and (2.12)

$$\begin{aligned}
\left[\hat{a}_i, \hat{H}_{\mathrm{KS}}\right] &= \sum_{jk} t_{jk} \left(\hat{a}_i \hat{a}_j^\dagger \hat{a}_k - \hat{a}_j^\dagger \hat{a}_k \hat{a}_i \right) \\
&= \sum_{jk} t_{jk} \left(\left(\delta_{ij} - \hat{a}_j^\dagger \hat{a}_i\right) \hat{a}_k - \hat{a}_j^\dagger \hat{a}_k \hat{a}_i \right) \\
&= \sum_{jk} t_{jk} \Big(\delta_{ij} \hat{a}_k + \hat{a}_j^\dagger \hat{a}_k \hat{a}_i - \hat{a}_j^\dagger \hat{a}_k \hat{a}_i \Big) = \sum_k t_{ik} \hat{a}_k \,.
\end{aligned} \tag{2.39}$$

We use this result to simplify the Green's function on the right-hand side of Eq. (2.34) and get

$$\begin{aligned} G^{\mathrm{R}}_{[a_i,H_{\mathrm{KS}}]a_j^\dagger}(t) &= G^{\mathrm{R}}_{\sum_k t_{ik}a_k a_j^\dagger}(t) \\ &= -i\Theta(t)\Big\langle \Big\{ \sum_k t_{ik}\hat{a}_k(t), \hat{a}_j^\dagger \Big\} \Big\rangle \\ &= \sum_k t_{ik}\Big(-i\Theta(t)\Big\langle \Big\{ \hat{a}_k(t), \hat{a}_j^\dagger \Big\} \Big\rangle \Big) \\ &= \sum_k t_{ik} G^{\mathrm{R}}_{kj}(t) \; . \end{aligned} \tag{2.40}$$

Now we calculate the Fourier transformation of Eq. (2.40) and get

$$G^{\mathrm{R}}_{[a_i,H_{\mathrm{KS}}]a_j^\dagger}(E^+) = \sum_k t_{ik} G^{\mathrm{R}}_{kj}(E^+) \; , \tag{2.41}$$

where we once again introduced a convergence-ensuring infinitesimal.

Now we use the results from Eqs. (2.36), (2.37) and (2.41) to calculate the Fourier transformation of Eq. (2.34) and get

$$E^+ G^{\mathrm{R}}_{ij}(E^+) = \delta_{ij} + \sum_k t_{ik} G^{\mathrm{R}}_{kj}(E^+) \; , \tag{2.42}$$

where we simplified the anticommutator in Eq. (2.37) using the anticommutator relations (2.12). We identify the last term on the right-hand side of Eq. (2.42) as a product of a Hamilton matrix with the matrix elements t_{ik} and a matrix Green's function with the matrix elements $G^{\mathrm{R}}_{kj}(E^+)$. We will distinguish the Hamilton matrix and matrix Green's functions in the orthonormal basis from the ones in the non-orthonormal basis by adding a tilde to the former ones. We write Eq. (2.42) in terms of matrices and solve it for the matrix Green's function. We get

$$\tilde{\mathbf{G}}^{\mathrm{R}}(E^+) = \Big[E^+ \mathbf{I} - \tilde{\mathbf{H}} \Big]^{-1} \; . \tag{2.43}$$

We generalize Eq. (2.43) to a non-orthonormal basis by applying the inverse transformation of Eq. (2.17) and we get

$$\boxed{\mathbf{G}^{\mathrm{R}}(E^+) = \big[E^+ \mathbf{S} - \mathbf{H} \big]^{-1}} \, , \tag{2.44}$$

with

$$\mathbf{H} = \left(\mathbf{O}_{\mathrm{S}}^{\mathrm{L}}\right)^{-1} \tilde{\mathbf{H}} \left(\mathbf{O}_{\mathrm{S}}^{\mathrm{R}}\right)^{-1} \tag{2.45}$$

$$\mathbf{G}(E^+) = \mathbf{O}_{\mathrm{S}}^{\mathrm{R}} \tilde{\mathbf{G}}(E^+) \mathbf{O}_{\mathrm{S}}^{\mathrm{L}} \; , \tag{2.46}$$

where $\mathbf{S}$ is once again the overlap matrix. The advanced matrix Green's function can be derived in the same way. The only difference in the derivation of the advanced and retarded matrix Green's function is that we have to ensure convergence at the lower integration limit and therefore we require the introduction of a negative infinitesimal $(-\delta)$. By doing so we get

$$\mathbf{G}^{\mathrm{A}}(E^{-}) = \left[E^{-}\mathbf{S} - \mathbf{H}\right]^{-1} \tag{2.47}$$

with $E^{-} = E - i0^{+}$. While we introduced the positive and negative infinitesimal for mathematical reasons, we can give them also physical meaning. The positive infinitesimal describes the propagation forward in time, while the negative one describes the propagation backward in time. The superscripts A and R make clear, whether the Green's function is a function of E^{+} or E^{-}. Therefore we will write the Green's functions in the following as functions of E only. By comparing Eqs. (2.44) and (2.47) and taking advantage of the hermiticity of the overlap matrix and the Hamiltonian matrix ($\mathbf{S} = \mathbf{S}^{\dagger}$, $\mathbf{H} = \mathbf{H}^{\dagger}$) we get following relation for the advanced and retarded matrix Green's function

$$\boxed{\mathbf{G}^{\mathrm{A}}(E) = \left(\mathbf{G}^{\mathrm{R}}(E)\right)^{\dagger}}. \tag{2.48}$$

2.4 Transport systems

DFT allows the treatment of finite or periodic systems but does not allow the calculation of transport systems containing semi-infinite electrodes. Thus other approaches have to be chosen for this kind of problems. In the case of localized orbitals one possibility is the DFT+NEGF approach as described in Ref. [7].

Within the DFT+NEGF approach the system is split into three parts as depicted in Fig. 2.1: the left electrode (L), the central region (C), also called extended molecule, and the right electrode (R). The central region has to contain all the electrode parts influenced by the molecule (darker in color), while the electrode parts not contained in the central region must show bulk behavior (lighter in color).

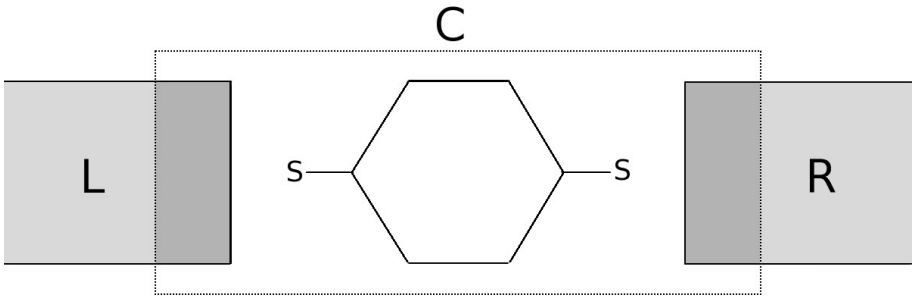

Fig. 2.1. Transport system. Within the DFT+NEGF approach the transport system is split into: left electrode (L), central region (C) and right electrode (R). The central region has to contain all electrode parts influenced by the molecule in the central region (darker in color), while the left and right electrode must show only bulk behaviour.

Per construction the left and right electrodes do not interact with each other and the system can be described by the Hamiltonian matrix

$$\mathbf{H}_{\text{system}} = \begin{pmatrix} \mathbf{H}_{\text{L}} & \mathbf{V}_{\text{LC}} & \mathbf{0} \\ \mathbf{V}_{\text{CL}} & \mathbf{H}_{\text{C}} & \mathbf{V}_{\text{CR}} \\ \mathbf{0} & \mathbf{V}_{\text{RC}} & \mathbf{H}_{\text{R}} \end{pmatrix} . \tag{2.49}$$

$\mathbf{H}_{\text{L}}$, $\mathbf{H}_{\text{C}}$ and $\mathbf{H}_{\text{R}}$ are the Hamiltonian matrices describing the left electrode, the central region and the right electrode, respectively. The $\mathbf{V}_{\text{ij}}$ describe the coupling of the central region to the corresponding electrode, where $\text{i}, \text{j} \in \{\text{L}, \text{C}, \text{R}\}$ and $\text{i} \neq \text{j}$.

We show in Sec. 2.4.1 how to treat the central region and in Sec. 2.4.2 we deal with the Hamiltonian matrices $\mathbf{H}_{\text{L}}$ and $\mathbf{H}_{\text{R}}$, which are in fact Hamiltonian matrices of infinite size.

2.4.1 Matrix Green's function of the central region

We will leave out the superscripts R and A and also the energy-dependency of the Green's functions to shorten the notation in the following. We will denote the advanced Green's functions by a dagger and leave out the dagger for the retarded Green's functions.

The following derivation is based on Ref. [17]. Using Eq. (2.44) and splitting up the system into L, C and R, we calculate the matrix Green's function of the system from

$$\left[E^{+} \begin{pmatrix} \mathbf{S}_{\text{L}} & \mathbf{S}_{\text{LC}} & \mathbf{0} \\ \mathbf{S}_{\text{CL}} & \mathbf{S}_{\text{C}} & \mathbf{S}_{\text{CR}} \\ \mathbf{0} & \mathbf{S}_{\text{RC}} & \mathbf{S}_{\text{R}} \end{pmatrix} - \begin{pmatrix} \mathbf{H}_{\text{L}} & \mathbf{V}_{\text{LC}} & \mathbf{0} \\ \mathbf{V}_{\text{CL}} & \mathbf{H}_{\text{C}} & \mathbf{V}_{\text{CR}} \\ \mathbf{0} & \mathbf{V}_{\text{RC}} & \mathbf{H}_{\text{R}} \end{pmatrix} \right] \begin{pmatrix} \mathbf{G}_{\text{L}} & \mathbf{G}_{\text{LC}} & \mathbf{0} \\ \mathbf{G}_{\text{CL}} & \mathbf{G}_{\text{C}} & \mathbf{G}_{\text{CR}} \\ \mathbf{0} & \mathbf{G}_{\text{RC}} & \mathbf{G}_{\text{R}} \end{pmatrix} = \mathbf{I} . \tag{2.50}$$

In this section, we are interested in the matrix Green's function $\mathbf{G}_{\text{C}}$ of the central region. We consider the second column of the matrix Green's function of the transport system and the identity matrix in Eq. 2.50, which produces the equations

$$\begin{aligned} \text{I} &: \mathbf{0} = \left(E^{+}\mathbf{S}_{\text{L}} - \mathbf{H}_{\text{L}}\right)\mathbf{G}_{\text{LC}} + \left(E^{+}\mathbf{S}_{\text{LC}} - \mathbf{V}_{\text{LC}}\right)\mathbf{G}_{\text{C}} \\ \text{II} &: \mathbf{I} = \left(E^{+}\mathbf{S}_{\text{CL}} - \mathbf{V}_{\text{CL}}\right)\mathbf{G}_{\text{LC}} + \left(E^{+}\mathbf{S}_{\text{C}} - \mathbf{H}_{\text{C}}\right)\mathbf{G}_{\text{C}} + \left(E^{+}\mathbf{S}_{\text{CR}} - \mathbf{V}_{\text{CR}}\right)\mathbf{G}_{\text{RC}} \\ \text{III} &: \mathbf{0} = \left(E^{+}\mathbf{S}_{\text{RC}} - \mathbf{V}_{\text{RC}}\right)\mathbf{G}_{\text{C}} + \left(E^{+}\mathbf{S}_{\text{R}} - \mathbf{H}_{\text{R}}\right)\mathbf{G}_{\text{RC}} . \end{aligned} \tag{2.51}$$

We solve Eqs. I and III to determine $\mathbf{G}_{\text{LC}}$ and $\mathbf{G}_{\text{RC}}$,

$$\begin{aligned} \mathbf{G}_{\text{LC}} &= -\left(E^{+}\mathbf{S}_{\text{L}} - \mathbf{H}_{\text{L}}\right)^{-1}\left(E^{+}\mathbf{S}_{\text{LC}} - \mathbf{V}_{\text{LC}}\right)\mathbf{G}_{\text{C}} \\ \mathbf{G}_{\text{RC}} &= -\left(E^{+}\mathbf{S}_{\text{R}} - \mathbf{H}_{\text{R}}\right)^{-1}\left(E^{+}\mathbf{S}_{\text{RC}} - \mathbf{V}_{\text{RC}}\right)\mathbf{G}_{\text{C}} \quad , \end{aligned} \tag{2.52}$$

and insert into Eq. II to obtain

$$\boxed{\mathbf{G}_{\text{C}} = \left[E^{+}\mathbf{S}_{\text{C}} - \mathbf{H}_{\text{C}} - \mathbf{\Sigma}_{\text{L}} - \mathbf{\Sigma}_{\text{R}}\right]^{-1}} . \tag{2.53}$$

Here, we introduced the so-called *hybridization matrices*

$$\mathbf{\Sigma}_{\text{L}} = \left(E^{+}\mathbf{S}_{\text{CL}} - \mathbf{V}_{\text{CL}}\right)\left(E^{+}\mathbf{S}_{\text{L}} - \mathbf{H}_{\text{L}}\right)^{-1}\left(E^{+}\mathbf{S}_{\text{LC}} - \mathbf{V}_{\text{LC}}\right) \tag{2.54}$$

$$\mathbf{\Sigma}_{\text{R}} = \left(E^{+}\mathbf{S}_{\text{CR}} - \mathbf{V}_{\text{CR}}\right)\left(E^{+}\mathbf{S}_{\text{R}} - \mathbf{H}_{\text{R}}\right)^{-1}\left(E^{+}\mathbf{S}_{\text{RC}} - \mathbf{V}_{\text{RC}}\right) . \tag{2.55}$$

By using Eq. (2.44) the hybridization matrices become

$$\mathbf{\Sigma}_{\mathrm{L}} = \left(E^{+}\mathbf{S}_{\mathrm{CL}} - \mathbf{V}_{\mathrm{CL}}\right) \mathbf{G}_{\mathrm{L}} \left(E^{+}\mathbf{S}_{\mathrm{LC}} - \mathbf{V}_{\mathrm{LC}}\right) \tag{2.56}$$

$$\mathbf{\Sigma}_{\mathrm{R}} = \left(E^{+}\mathbf{S}_{\mathrm{CR}} - \mathbf{V}_{\mathrm{CR}}\right) \mathbf{G}_{\mathrm{R}} \left(E^{+}\mathbf{S}_{\mathrm{RC}} - \mathbf{V}_{\mathrm{RC}}\right) \ . \tag{2.57}$$

2.4.2 Surface Green's functions

Eq. (2.53) provides a way to evaluate the matrix Green's function of a finite subsystem, the central region, including the influence of the leads L and R in terms of the hybridization matrix. The hybridization matrices appearing in that equation still require the evaluation of the semi-infinite electrodes. This can be avoided using the concept of surface Green's functions (SGF). SGFs are treated in more detail in e.g. Ref [17].

We take advantage of the periodicity of the electrodes and split them up into identical clusters. The clusters $\mathbf{cl}_{\mathrm{L}}$ and $\mathbf{cl}_{\mathrm{R}}$ in Fig. 2.2 build up the left and right electrode, respectively.

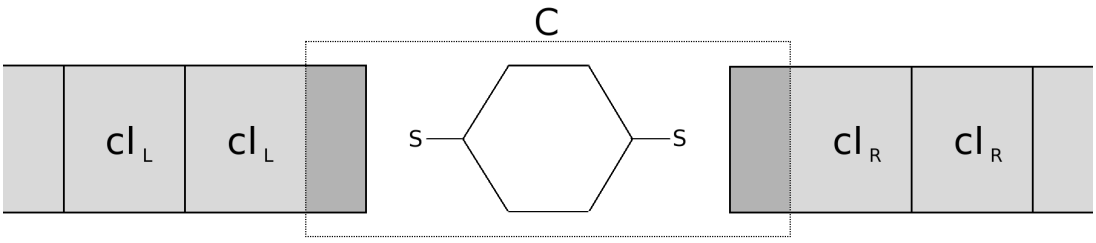

Fig. 2.2. Partitioning of the electrodes into clusters. For treating a transport system containing semi-infinite electrodes within the SGF approach we split the left electrode into identical clusters cl_{L} and the right electrode into identical clusters cl_{R}.

Using localized orbitals we can split up the electrodes into clusters, which couple only to nearest-neighboring clusters. By doing so, the Hamiltonian matrix in Eq. (2.49) becomes

$$\mathbf{H}_{\mathrm{system}} = \begin{pmatrix}
\cdot & \cdot & & & & & & & \\
\cdot & \cdot & \mathbf{V}_{\mathrm{cl_L}} & & & & 0 & & \\
 & (\mathbf{V}_{\mathrm{cl_L}})^{\dagger} & \mathbf{H}_{\mathrm{cl_L}} & \mathbf{V}_{\mathrm{cl_L}} & & & & & \\
 & & (\mathbf{V}_{\mathrm{cl_L}})^{\dagger} & \mathbf{H}_{\mathrm{cl_L}} & \mathbf{V}_{\mathrm{cl_L C}} & & & & \\
 & & & \mathbf{V}_{\mathrm{C cl_L}} & \mathbf{H}_{\mathrm{C}} & \mathbf{V}_{\mathrm{C cl_R}} & & & \\
 & & & & \mathbf{V}_{\mathrm{cl_R C}} & \mathbf{H}_{\mathrm{cl_R}} & \mathbf{V}_{\mathrm{cl_R}} & & \\
 & & & & & (\mathbf{V}_{\mathrm{cl_R}})^{\dagger} & \mathbf{H}_{\mathrm{cl_R}} & \mathbf{V}_{\mathrm{cl_R}} & \\
 & & 0 & & & & (\mathbf{V}_{\mathrm{cl_R}})^{\dagger} & \cdot & \cdot \\
 & & & & & & & \cdot & \cdot
\end{pmatrix} , \tag{2.58}$$

where the $\mathbf{H}_{\mathrm{cl_i}}$ are the Hamiltonian matrices of the electrode clusters and the matrices $\mathbf{V}_{\mathrm{cl_i}}$ describe the coupling of neighboring electrode clusters with $\mathrm{i} \in \{\mathrm{L}, \mathrm{R}\}$. We split the overlap matrix in the same way. $\mathbf{S}_{\mathrm{cl_i}}$ contains the overlap of orbitals centered around atoms of the same cluster and $\mathbf{s}_{\mathrm{cl_i}}$ contains the overlap of orbitals centered around atoms part of neighboring clusters.

We calculate $\mathbf{G}_\mathrm{C}$ in the same way as in Sec. 2.4.1 using the Hamiltonian matrix (2.58). We get a similar result as in Eq. (2.53) with the hybridization matrices being

$$\boxed{\mathbf{\Sigma}_\mathrm{i} = \left(E^+\mathbf{s}_{\mathrm{C}\mathrm{cl}_\mathrm{i}} - \mathbf{V}_{\mathrm{C}\mathrm{cl}_\mathrm{i}}\right) \mathbf{G}^{\mathrm{SGF}}_{\mathrm{cl}_\mathrm{i}} \left(E^+\mathbf{s}_{\mathrm{cl}_\mathrm{i}\mathrm{C}} - \mathbf{V}_{\mathrm{cl}_\mathrm{i}\mathrm{C}}\right)} \,. \tag{2.59}$$

The matrix Green's functions $\mathbf{G}^{\mathrm{SGF}}_{\mathrm{cl}_\mathrm{i}}$ are the matrix Green's functions of the clusters at the electrode surfaces. In contrast to Eq. (2.53) only the matrix Green's functions of the surface clusters, the surface Green's functions, enter in the hybridization matrices.

Next, we discuss an iterative procedure to calculate $\mathbf{G}^{\mathrm{SGF}}_{\mathrm{cl}_\mathrm{i}}$. We distinguish the matrix Green's functions of the coupled and isolated electrode clusters by the following notation

$$\mathbf{g}_{\mathrm{cl}_\mathrm{i}}(E) = \left[E^+\mathbf{S}_{\mathrm{cl}_\mathrm{i}} - \mathbf{H}_{\mathrm{cl}_\mathrm{i}}\right]^{-1} \tag{2.60}$$

$$\mathbf{G}_{\mathrm{cl}_\mathrm{i}}(E) = \left[E^+\mathbf{S}_{\mathrm{cl}_\mathrm{i}} - \mathbf{H}_{\mathrm{cl}_\mathrm{i}} - \mathbf{\Sigma}_{\mathrm{cl}_\mathrm{i}}\right]^{-1} \,, \tag{2.61}$$

where $\mathbf{\Sigma}_{\mathrm{cl}_\mathrm{i}}$ describes the influence of the nearest-neighbor clusters. We build the semi-infinite electrodes now by successively coupling clusters. We start from a single cluster of the left electrode and couple a second one towards it. We calculate the SGF of this two-cluster electrode similarly to Eq. (2.53) and get

$$\mathbf{G}^{\mathrm{SGF}}_{\mathrm{cl}_\mathrm{L}(1)} = \left[E^+\mathbf{S}_{\mathrm{cl}_\mathrm{L}} - \mathbf{H}_{\mathrm{cl}_\mathrm{L}} - \underbrace{\left(E^+\mathbf{s}_{\mathrm{cl}_\mathrm{L}} - \mathbf{V}_{\mathrm{cl}_\mathrm{L}}\right)^\dagger \mathbf{g}_{\mathrm{cl}_\mathrm{L}} \left(E^+\mathbf{s}_{\mathrm{cl}_\mathrm{L}} - \mathbf{V}_{\mathrm{cl}_\mathrm{L}}\right)}_{\mathbf{\Sigma}_{\mathrm{cl}_\mathrm{L}\mathbf{(1)}}}\right]^{-1} \,, \tag{2.62}$$

where the subscript (1) denotes the first iteration step. In the next step, we couple a third cluster to the two-cluster electrode. Like in Eq. (2.59), only the SGF of the two-cluster electrode enters the hybridization matrix

$$\mathbf{G}^{\mathrm{SGF}}_{\mathrm{cl}_\mathrm{L}(2)} = \left[E^+\mathbf{S}_{\mathrm{cl}_\mathrm{L}} - \mathbf{H}_{\mathrm{cl}_\mathrm{L}} - \underbrace{\left(E^+\mathbf{s}_{\mathrm{cl}_\mathrm{L}} - \mathbf{V}_{\mathrm{cl}_\mathrm{L}}\right)^\dagger \mathbf{G}^{\mathrm{SGF}}_{\mathrm{cl}_\mathrm{L}(1)} \left(E^+\mathbf{s}_{\mathrm{cl}_\mathrm{L}} - \mathbf{V}_{\mathrm{cl}_\mathrm{L}}\right)}_{\mathbf{\Sigma}_{\mathrm{cl}_\mathrm{L}\mathbf{(2)}}}\right]^{-1} \,. \tag{2.63}$$

We see from this equation that the SGF of an n-cluster electrode is calculated by

$$\mathbf{G}^{\mathrm{SGF}}_{\mathrm{cl}_\mathrm{L}(n-1)} = \left[E^+\mathbf{S}_{\mathrm{cl}_\mathrm{L}} - \mathbf{H}_{\mathrm{cl}_\mathrm{L}} - \underbrace{\left(E^+\mathbf{s}_{\mathrm{cl}_\mathrm{L}} - \mathbf{V}_{\mathrm{cl}_\mathrm{L}}\right)^\dagger \mathbf{G}^{\mathrm{SGF}}_{\mathrm{cl}_\mathrm{L}(n-2)} \left(E^+\mathbf{s}_{\mathrm{cl}_\mathrm{L}} - \mathbf{V}_{\mathrm{cl}_\mathrm{L}}\right)}_{\mathbf{\Sigma}_{\mathrm{cl}_\mathrm{L}\mathbf{(n-1)}}}\right]^{-1} \,. \tag{2.64}$$

The coupling of additional electrode clusters has to be repeated until $\mathbf{G}^{\mathrm{SGF}}_{\mathrm{cl}_\mathrm{L}(n)}$ is sufficiently well converged. The SGF $\mathbf{G}^{\mathrm{SGF}}_{\mathrm{cl}_\mathrm{R}(n)}$ of the right electrode is calculated in the same way, where the hybridization matrix has the form

$$\mathbf{\Sigma}_{\mathrm{cl}_\mathrm{R}\mathbf{(n-1)}} = \left(E^+\mathbf{s}_{\mathrm{cl}_\mathrm{R}} - \mathbf{V}_{\mathrm{cl}_\mathrm{R}}\right) \mathbf{G}^{\mathrm{SGF}}_{\mathrm{cl}_\mathrm{R}(n-2)} \left(E^+\mathbf{s}_{\mathrm{cl}_\mathrm{R}} - \mathbf{V}_{\mathrm{cl}_\mathrm{R}}\right)^\dagger \,. \tag{2.65}$$

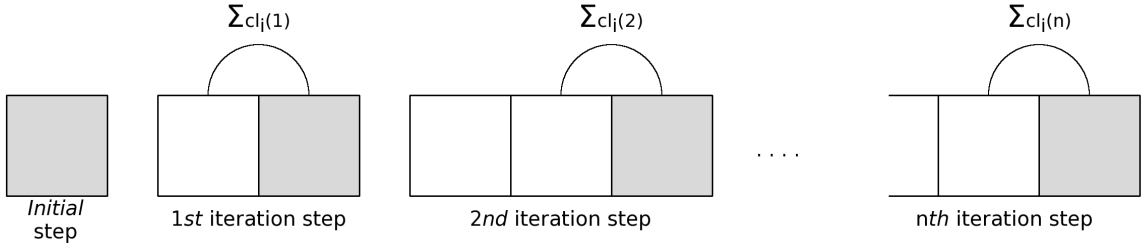

Fig. 2.3. Iteration scheme using the concept of surface Green's functions. One starts by a single cluster and couples in each iteration step an additional cluster (gray) until the SGF is sufficiently well converged. The semicircles indicate the coupling of the clusters (squares) towards one another.

2.4.2.1 Sancho-Rubio method

The iteration scheme discussed above requires generally many iteration steps until convergence is reached. The Sancho-Rubio method [18] is an improved iteration scheme. We derive the Sancho-Rubio method according to Ref. [18].

For deriving the Sancho-Rubio method, we use a different formalism to couple the electrode clusters. The derivation of this formalism occurs according to Ref. [19]. We start by splitting up the Hamiltonian matrix of the semi-infinite electrode and its overlap matrix into

$$\mathbf{H}_\mathrm{i} = \mathbf{H}_\mathrm{i}^\mathrm{cl} + \mathbf{V}_\mathrm{i}^\mathrm{cl} \tag{2.66}$$

$$\mathbf{S}_\mathrm{i} = \mathbf{S}_\mathrm{i}^\mathrm{cl} + \mathbf{s}_\mathrm{i}^\mathrm{cl}\,, \tag{2.67}$$

where $\mathbf{H}_\mathrm{i}^\mathrm{cl}$ contains all Hamiltonian matrices of the electrode clusters and $\mathbf{V}_\mathrm{i}^\mathrm{cl}$ all coupling matrix elements between these clusters. Likewise, $\mathbf{S}_\mathrm{i}^\mathrm{cl}$ contains all overlaps of orbitals within the same cluster and $\mathbf{s}_\mathrm{i}^\mathrm{cl}$ all overlaps between orbitals within different clusters.

In Sec. 2.3.1 we have seen that the Hamiltonian matrices of one-particle Hamiltonians fulfill Eq. (2.44). Due to $\mathbf{H}_\mathrm{i}$ and $\mathbf{H}_\mathrm{i}^\mathrm{cl}$ being Hamiltonian matrices of one-particle Hamiltonians we get

$$\left[E^+\mathbf{S}_\mathrm{i}^\mathrm{cl} - \mathbf{H}_\mathrm{i}^\mathrm{cl}\right]\mathbf{g}_\mathrm{i}^\mathrm{cl} = \mathbf{I} \tag{2.68}$$

$$\left[E^+\mathbf{S}_\mathrm{i} - \mathbf{H}_\mathrm{i}\right]\mathbf{G}_\mathrm{i} = \mathbf{I}\,, \tag{2.69}$$

where $\mathbf{g}_\mathrm{i}^\mathrm{cl}$ is a block-diagonal matrix containing the matrix Green's functions of the clusters (2.60) and $\mathbf{G}_\mathrm{i}$ is the full electrode Green's function. We rewrite Eq. (2.69) using Eqs. (2.66) and (2.67)

$$\left[E^+\mathbf{S}_\mathrm{i} - \mathbf{H}_\mathrm{i}\right]\mathbf{G}_\mathrm{i} = \underbrace{\left[E^+\mathbf{S}_\mathrm{i}^\mathrm{cl} - \mathbf{H}_\mathrm{i}^\mathrm{cl}\right]}_{\left(\mathbf{g}_\mathrm{i}^\mathrm{cl}\right)^{-1}}\mathbf{G}_\mathrm{i} + \underbrace{\left(E^+\mathbf{s}_\mathrm{i}^\mathrm{cl} - \mathbf{V}_\mathrm{i}^\mathrm{cl}\right)}_{\mathbf{V}'}\mathbf{G}_\mathrm{i} = \mathbf{I} \tag{2.70}$$

and multiply it from the left by $\mathbf{g}_\mathrm{i}^\mathrm{cl}$. To shorten the notation we will omit the subscripts i and superscripts cl in the following. After rearranging the resulting equation we get

$$\boxed{\mathbf{G} = \mathbf{g} - \mathbf{g}\mathbf{V}'\mathbf{G}}\,. \tag{2.71}$$

Using Eq. (2.71) we calculate the surface Green's functions and get

$$\mathbf{G}^{\mathrm{SGF}} = \mathbf{G}^{11} = \mathbf{g}^{11} - \sum_{\gamma,\delta} \mathbf{g}^{1\gamma}\mathbf{V}'^{\gamma\delta}\mathbf{G}^{\delta 1} = \mathbf{g}^{11} - \mathbf{g}^{11}\mathbf{V}'^{12}\mathbf{G}^{21} \ . \tag{2.72}$$

The remaining terms in Eq. (2.72) vanish due to $\mathbf{g}^{1\gamma} = \mathbf{0}$ for $\gamma \neq 1$ and $\mathbf{V}'^{\gamma\delta} = \mathbf{0}$ for $\gamma \neq \delta \pm 1$.

We calculate the matrix Green's function $\mathbf{G}^{21}$ using Eq. (2.71)

$$\mathbf{G}^{21} = -\mathbf{g}^{22}\mathbf{V}'^{21}\mathbf{G}^{11} - \mathbf{g}^{22}\mathbf{V}'^{23}\mathbf{G}^{31} = -\mathbf{t}_0\mathbf{G}^{11} - \mathbf{t}_0^\dagger\mathbf{G}^{31} \ , \tag{2.73}$$

where we introduced the matrices

$$\mathbf{t}_0 = \mathbf{g}^{22}\mathbf{V}'^{21} \tag{2.74}$$

$$\mathbf{t}_0^\dagger = \mathbf{g}^{22}\mathbf{V}'^{23} \tag{2.75}$$

to simplify the notation in the following derivation. We take in the following derivation advantage of the electrode clusters being identical and therefore $\mathbf{g}^{ii} = \mathbf{g}^{jj}$ and $\mathbf{V}'^{i,i+1} = \mathbf{V}'^{j,j+1}$. Due to the hermiticity of the overlap matrix and Hamiltonian matrix we have additionally $\mathbf{V}'^{i,i+1} = \left(\mathbf{V}'^{i,i-1}\right)^\dagger$. Now we are able to derive the Sancho-Rubio method.

1st iteration step

Starting point of the Sancho-Rubio method is Eq. (2.73). We calculate the matrix Green's function $\mathbf{G}^{31}$ appearing in Eq. (2.73) in the same way as $\mathbf{G}^{21}$ and get

$$\mathbf{G}^{31} = -\mathbf{t}_0\mathbf{G}^{21} - \mathbf{t}_0^\dagger\mathbf{G}^{41} \ . \tag{2.76}$$

Now we write $\mathbf{G}^{21}$ and $\mathbf{G}^{41}$ in Eq. (2.76) in the same way as $\mathbf{G}^{31}$ itself

$$\mathbf{G}^{31} = -\mathbf{t}_0\left(-\mathbf{t}_0\mathbf{G}^{11} - \mathbf{t}_0^\dagger\mathbf{G}^{31}\right) - \mathbf{t}_0^\dagger\left(-\mathbf{t}_0\mathbf{G}^{31} - \mathbf{t}_0^\dagger\mathbf{G}^{51}\right) \ . \tag{2.77}$$

In the next step we group all terms containing the matrix Green's function $\mathbf{G}^{31}$ together

$$\left(\mathbf{I} - \mathbf{t}_0\mathbf{t}_0^\dagger - \mathbf{t}_0^\dagger\mathbf{t}_0\right)\mathbf{G}^{31} = \mathbf{t}_0\mathbf{t}_0\mathbf{G}^{11} + \mathbf{t}_0^\dagger\mathbf{t}_0^\dagger\mathbf{G}^{51} \ . \tag{2.78}$$

We multiply this equation by $\left(\mathbf{I} - \mathbf{t}_0\mathbf{t}_0^\dagger - \mathbf{t}_0^\dagger\mathbf{t}_0\right)^{-1}$ and get

$$\mathbf{G}^{31} = \mathbf{t}_1\mathbf{G}^{11} + \mathbf{t}_1^\dagger\mathbf{G}^{51} \ , \tag{2.79}$$

with

$$\mathbf{t}_1 = \left(\mathbf{I} - \mathbf{t}_0\mathbf{t}_0^\dagger - \mathbf{t}_0^\dagger\mathbf{t}_0\right)^{-1}\mathbf{t}_0\mathbf{t}_0 \tag{2.80}$$

$$\mathbf{t}_1^\dagger = \left(\mathbf{I} - \mathbf{t}_0\mathbf{t}_0^\dagger - \mathbf{t}_0^\dagger\mathbf{t}_0\right)^{-1}\mathbf{t}_0^\dagger\mathbf{t}_0^\dagger \,. \tag{2.81}$$

The newly appearing matrices $\mathbf{t}_1$ and $\mathbf{t}_1^\dagger$ can be interpreted as an effective coupling towards next-nearest-neighbor clusters. Now we insert Eq. (2.79) into Eq. (2.73) and get

$$\mathbf{G}_{(1)}^{21} = -\left(\mathbf{t}_0 + \mathbf{t}_0^\dagger\mathbf{t}_1\right)\mathbf{G}^{11} - \mathbf{t}_0^\dagger\mathbf{t}_1^\dagger\mathbf{G}^{51} \,, \tag{2.82}$$

2.4.2.2 2nd iteration step

We rewrite the matrix Green's function $\mathbf{G}^{51}$ using Eq. (2.79) and get

$$\mathbf{G}^{51} = \mathbf{t}_1\mathbf{G}^{31} + \mathbf{t}_1^\dagger\mathbf{G}^{71} \,. \tag{2.83}$$

Now we apply Eq. (2.79) to the matrix Green's functions $\mathbf{G}^{31}$ and $\mathbf{G}^{71}$ and get

$$\mathbf{G}^{51} = \mathbf{t}_1\left(\mathbf{t}_1\mathbf{G}^{11} + \mathbf{t}_1^\dagger\mathbf{G}^{51}\right) + \mathbf{t}_1^\dagger\left(\mathbf{t}_1\mathbf{G}^{51} + \mathbf{t}_1^\dagger\mathbf{G}^{91}\right) \,, \tag{2.84}$$

which can be treated in the same way as Eq. (2.77)

$$\mathbf{G}^{51} = \mathbf{t}_2\mathbf{G}^{11} + \mathbf{t}_2^\dagger\mathbf{G}^{91} \tag{2.85}$$

with

$$\mathbf{t}_2 = \left(\mathbf{I} - \mathbf{t}_1\mathbf{t}_1^\dagger - \mathbf{t}_1^\dagger\mathbf{t}_1\right)^{-1}\mathbf{t}_1\mathbf{t}_1 \tag{2.86}$$

$$\mathbf{t}_2^\dagger = \left(\mathbf{I} - \mathbf{t}_1\mathbf{t}_1^\dagger - \mathbf{t}_1^\dagger\mathbf{t}_1\right)^{-1}\mathbf{t}_1^\dagger\mathbf{t}_1^\dagger \,. \tag{2.87}$$

We insert this result into Eq. (2.82) and get

$$\mathbf{G}_{(2)}^{21} = -\left(\mathbf{t}_0 + \mathbf{t}_0^\dagger\mathbf{t}_1 + \mathbf{t}_0^\dagger\mathbf{t}_1^\dagger\mathbf{t}_2\right)\mathbf{G}^{11} - \mathbf{t}_0^\dagger\mathbf{t}_1^\dagger\mathbf{t}_2^\dagger\mathbf{G}^{91} \,, \tag{2.88}$$

nth iteration step

We see that we can generalize the above procedure and calculate the matrix Green's function $\mathbf{G}^{2^n+1,1}$ with $n = 1, 2, 3, ...$ by

$$\begin{aligned}\mathbf{G}^{2^n+1,1} &= \mathbf{t}_{n-1}\mathbf{G}^{2^n-2^{n-1}+1,1} + \mathbf{t}_{n-1}^\dagger\mathbf{G}^{2^n+2^{n-1}+1,1} \\ &= \mathbf{t}_{n-1}\left(\mathbf{t}_{n-1}\mathbf{G}^{11} + \mathbf{t}_{n-1}^\dagger\mathbf{G}^{2^n+1,1}\right) + \mathbf{t}_{n-1}^\dagger\left(\mathbf{t}_{n-1}\mathbf{G}^{2^n+1,1} + \mathbf{t}_{n-1}^\dagger\mathbf{G}^{2^{n+1}+1,1}\right) \,.\end{aligned} \tag{2.89}$$

This equation can be treated in the same way as Eqs. (2.77) and (2.84) and we get

$$\mathbf{G}^{2^n+1,1} = \mathbf{t}_n \mathbf{G}^{11} + \mathbf{t}_n^\dagger \mathbf{G}^{2^{n+1}+1,1} \,, \tag{2.90}$$

where

$$\mathbf{t}_n = \left(\mathbf{I} - \mathbf{t}_{n-1}\mathbf{t}_{n-1}^\dagger - \mathbf{t}_{n-1}^\dagger \mathbf{t}_{n-1}\right)^{-1} \mathbf{t}_{n-1}\mathbf{t}_{n-1} \tag{2.91}$$

$$\mathbf{t}_n^\dagger = \left(\mathbf{I} - \mathbf{t}_{n-1}\mathbf{t}_{n-1}^\dagger - \mathbf{t}_{n-1}^\dagger \mathbf{t}_{n-1}\right)^{-1} \mathbf{t}_{n-1}^\dagger \mathbf{t}_{n-1}^\dagger \,. \tag{2.92}$$

After n iterations we get

$$\mathbf{G}_{(n)}^{21} = -\underbrace{\left(\mathbf{t}_0^\dagger + \mathbf{t}_0^\dagger\mathbf{t}_1 + \mathbf{t}_0^\dagger\mathbf{t}_1^\dagger\mathbf{t}_2 + ... + \mathbf{t}_0^\dagger\mathbf{t}_1^\dagger\mathbf{t}_2^\dagger ... \mathbf{t}_{n-1}^\dagger\mathbf{t}_n\right)}_{=:\mathbf{T}_{(n)}} \mathbf{G}^{11} - \mathbf{t}_0^\dagger\mathbf{t}_1^\dagger\mathbf{t}_2^\dagger ... \mathbf{t}_{n-1}^\dagger\mathbf{t}_n^\dagger \mathbf{G}^{2^{n+1}+1,1} \,, \tag{2.93}$$

where we introduced the transfer matrix $\mathbf{T}$. The matrix Green's function $\mathbf{G}_{(n)}^{21}$ has to be iterated until the last term of Eq. (2.93) is negligible

$$\mathbf{G}_{(n)}^{21} \approx -\mathbf{T}_{(n)}\mathbf{G}^{11} \,. \tag{2.94}$$

We insert Eq. (2.94) into Eq. (2.72)

$$\mathbf{G}_{(n)}^{11} = \mathbf{g}^{11} + \mathbf{g}^{11}\mathbf{V}'^{12}\mathbf{T}_{(n)}\mathbf{G}^{11} \,. \tag{2.95}$$

We group all terms containing $\mathbf{G}^{11}$ and multiply this equation by $\mathbf{g}^{11}$ from the left

$$\left(\left(\mathbf{g}^{11}\right)^{-1} - \mathbf{V}'^{12}\mathbf{T}_{(n)}\right)\mathbf{G}_{(n)}^{11} = \mathbf{I} \,. \tag{2.96}$$

We multiple now the inverse of the expression within brackets from the left and express the inverse of $\mathbf{g}^{11}$ using Eq. (2.60). We get

$$\boxed{\mathbf{G}_{(n)}^{11} = \left(E^+\mathbf{S}_{\mathrm{cl_i}} - \mathbf{H}_{\mathrm{cl_i}} - \mathbf{V}'^{12}\mathbf{T}_{(n)}\right)^{-1}} \,, \tag{2.97}$$

where $\mathrm{i} \in \{\mathrm{L}, \mathrm{R}\}$.

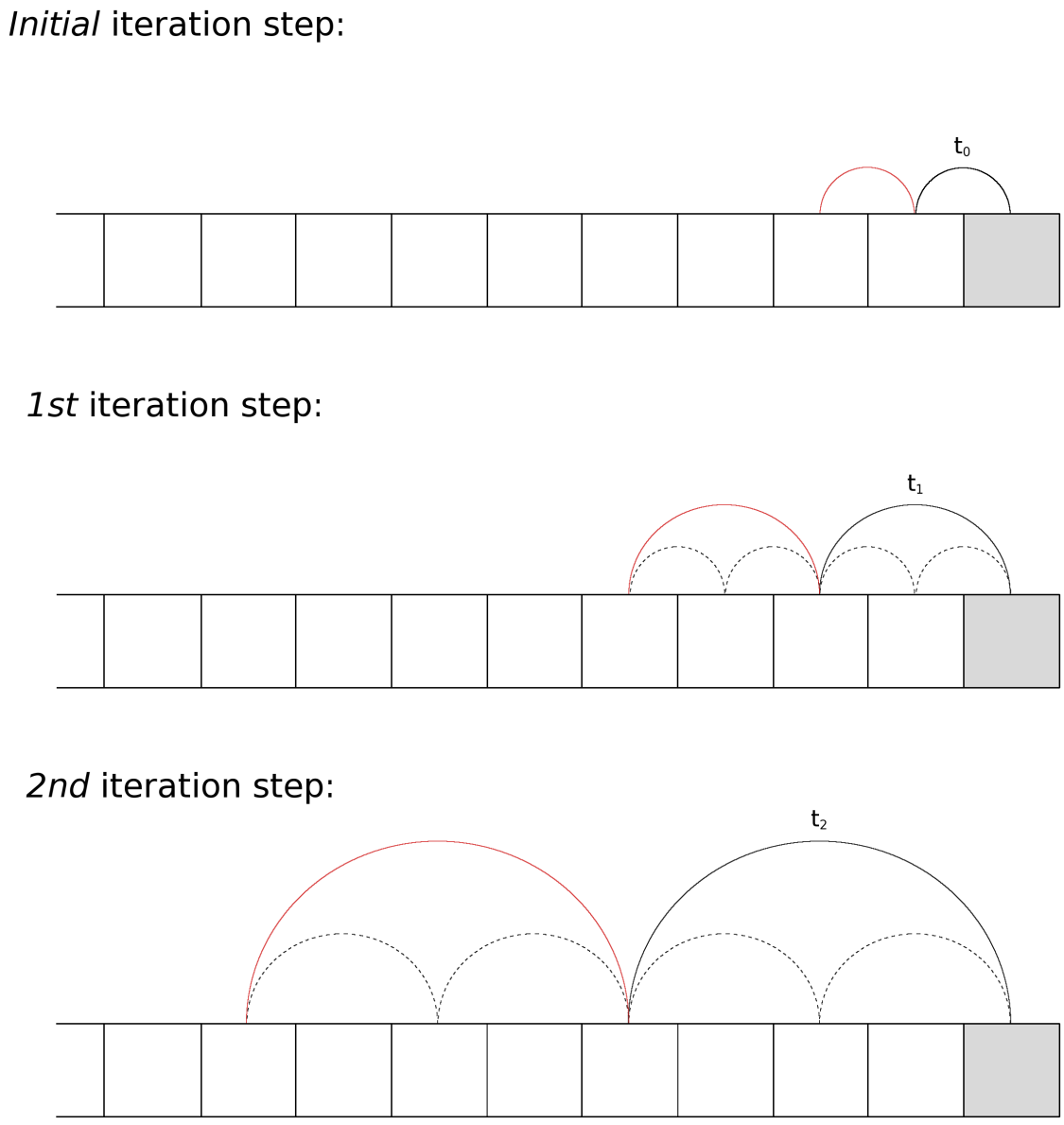

Fig. 2.4. Scheme of the Sancho-Rubio method.
Initial iteration step: The contribution of the surface Green's function (solid black semicircle) to the matrix Green's function $\mathbf{G}^{21}$ is considered, while the contribution from the left neighboring cluster (red semicircle) is neglected.
1st iteration step: We couple the 3rd cluster to the 1st and 5th cluster using the matrix $\mathbf{t}_1$. We neglect the contributions from the 5th cluster and consider the remaining contribution to the matrix Green's function $\mathbf{G}^{21}$ trough the transfer matrix $\mathbf{T}_{(1)}$
2nd iteration step: We repeat the previous step. We couple the 5th cluster to the 1st and 9th cluster using the matrix $\mathbf{t}_2$. We neglect the coupling towards the 9th cluster and consider the remaining contribution to the matrix Green's function $\mathbf{G}^{21}$ trough the transfer matrix $\mathbf{T}_{(2)}$.
This procedure is repeated until $\mathbf{G}^{21}$ is sufficiently well converged.

2.4.3 Current and transmission

Using the Hamiltonian matrix (2.49) formulas for calculating the transmission and current of the transport system can be derived [17, 20, 21]. The idea is to treat incoming wavefunctions as a perturbation and to view the reflected part of this wavefunction and the wavefunctions in the remaining subsystems as a response to this perturbation.

For the moment, we will consider only an incoming wavefunction at the left electrode, which is an eigenfunction of the Hamiltonian matrix $\mathbf{H}_\mathrm{L}$, and generalize the results at the end to any incoming wavefunction from any of the electrodes. The ansatz for the wavefunction $\big|\Psi_\mathrm{L}\big\rangle$ is

$$\big|\Psi_\mathrm{L}\big\rangle = \big|\psi_\mathrm{L}\big\rangle + \big|\psi^\mathrm{r}\big\rangle \,, \tag{2.98}$$

where $\big|\psi_\mathrm{L}\big\rangle$ is an eigenfunction of $\mathbf{H}_\mathrm{L}$ and $\big|\psi^\mathrm{r}\big\rangle$ is the left electrode's response to the incoming wavefunction. We have to solve the eigenvalue problem

$$\begin{pmatrix} \mathbf{H}_\mathrm{L} & \mathbf{V}_\mathrm{LC} & \mathbf{0} \\ \mathbf{V}_\mathrm{CL} & \mathbf{H}_\mathrm{C} & \mathbf{V}_\mathrm{CR} \\ \mathbf{0} & \mathbf{V}_\mathrm{RC} & \mathbf{H}_\mathrm{R} \end{pmatrix} \begin{pmatrix} \big|\Psi_\mathrm{L}\big\rangle \\ \big|\Psi_\mathrm{C}\big\rangle \\ \big|\Psi_\mathrm{R}\big\rangle \end{pmatrix} = E \begin{pmatrix} \mathbf{S}_\mathrm{L} & \mathbf{S}_\mathrm{LC} & \mathbf{0} \\ \mathbf{S}_\mathrm{CL} & \mathbf{S}_\mathrm{C} & \mathbf{S}_\mathrm{CR} \\ \mathbf{0} & \mathbf{S}_\mathrm{RC} & \mathbf{S}_\mathrm{R} \end{pmatrix} \begin{pmatrix} \big|\Psi_\mathrm{L}\big\rangle \\ \big|\Psi_\mathrm{C}\big\rangle \\ \big|\Psi_\mathrm{R}\big\rangle \end{pmatrix} . \tag{2.99}$$

Thus the following three equations have to be solved

$$\begin{aligned} \mathrm{I} &: \mathbf{H}_\mathrm{L}\big|\Psi_\mathrm{L}\big\rangle + \mathbf{V}_\mathrm{LC}\big|\Psi_\mathrm{C}\big\rangle = E\mathbf{S}_\mathrm{L}\big|\Psi_\mathrm{L}\big\rangle + E\mathbf{S}_\mathrm{LC}\big|\Psi_\mathrm{C}\big\rangle \\ \mathrm{II} &: \mathbf{V}_\mathrm{CL}\big|\Psi_\mathrm{L}\big\rangle + \mathbf{H}_\mathrm{C}\big|\Psi_\mathrm{C}\big\rangle + \mathbf{V}_\mathrm{CR}\big|\Psi_\mathrm{R}\big\rangle = E\mathbf{S}_\mathrm{CL}\big|\Psi_\mathrm{L}\big\rangle + E\mathbf{S}_\mathrm{C}\big|\Psi_\mathrm{C}\big\rangle + E\mathbf{S}_\mathrm{CR}\big|\Psi_\mathrm{R}\big\rangle \\ \mathrm{III} &: \mathbf{V}_\mathrm{RC}\big|\Psi_\mathrm{C}\big\rangle + \mathbf{H}_\mathrm{R}\big|\Psi_\mathrm{R}\big\rangle = E\mathbf{S}_\mathrm{RC}\big|\Psi_\mathrm{C}\big\rangle + E\mathbf{S}_\mathrm{R}\big|\Psi_\mathrm{R}\big\rangle \,. \end{aligned} \tag{2.100}$$

We rearrange them and get

$$\begin{aligned} \mathrm{I} &: (\mathbf{V}_\mathrm{LC} - E\mathbf{S}_\mathrm{LC})\big|\Psi_\mathrm{C}\big\rangle = [E\mathbf{S}_\mathrm{L} - \mathbf{H}_\mathrm{L}]\big|\Psi_\mathrm{L}\big\rangle \\ \mathrm{II} &: (\mathbf{V}_\mathrm{CL} - E\mathbf{S}_\mathrm{CL})\big|\Psi_\mathrm{L}\big\rangle + (\mathbf{V}_\mathrm{CR} - E\mathbf{S}_\mathrm{CR})\big|\Psi_\mathrm{R}\big\rangle = [E\mathbf{S}_\mathrm{C} - \mathbf{H}_\mathrm{C}]\big|\Psi_\mathrm{C}\big\rangle \\ \mathrm{III} &: (\mathbf{V}_\mathrm{RC} - E\mathbf{S}_\mathrm{RC})\big|\Psi_\mathrm{C}\big\rangle = [E\mathbf{S}_\mathrm{R} - \mathbf{H}_\mathrm{R}]\big|\Psi_\mathrm{R}\big\rangle \,. \end{aligned} \tag{2.101}$$

For the sake of readability we introduce

$$(\mathbf{V}_\mathrm{ij} - E\mathbf{S}_\mathrm{ij}) \to \mathbf{V}_\mathrm{ij} \,, \tag{2.102}$$

where $\mathrm{i} \neq \mathrm{j}$ and $\mathrm{i,j} \in \{\mathrm{L,C,R}\}$. The terms in square brackets are again the inverse of the matrix Green's functions of the subsystems. The second term on the left-hand side in Eq. II describes the central region's response to an incoming wavefunction at the right electrode. We have no incoming wavefunction at the right electrode and therefore this term vanishes.

We get

$$\begin{aligned} \text{I} &: \mathbf{G}_\text{L}\mathbf{V}_\text{LC}\big|\Psi_\text{C}\big\rangle = \mathbf{I}\big|\Psi_\text{L}\big\rangle \\ \text{II} &: \mathbf{G}_\text{C}\mathbf{V}_\text{CL}\big|\Psi_\text{L}\big\rangle = \mathbf{I}\big|\Psi_\text{C}\big\rangle \\ \text{III} &: \mathbf{G}_\text{R}\mathbf{V}_\text{RC}\big|\Psi_\text{C}\big\rangle = \mathbf{I}\big|\Psi_\text{R}\big\rangle \,, \end{aligned} \tag{2.103}$$

where we multiplied Eqs. I, II and III by $\mathbf{G}_\text{L}$, $\mathbf{G}_\text{C}$ and $\mathbf{G}_\text{R}$, respectively.

Eq. II responds to the incoming wavefunction $\big|\psi_\text{L}\big\rangle$ and therefore we get

$$\mathbf{G}_\text{C}\mathbf{V}_\text{CL}\big|\psi_\text{L}\big\rangle = \mathbf{I}\big|\Psi_\text{C}\big\rangle \,. \tag{2.104}$$

Inserting the result from Eq. II into Eq. III yields

$$\mathbf{G}_\text{R}\mathbf{V}_\text{RC}\mathbf{G}_\text{C}\mathbf{V}_\text{CL}\big|\psi_\text{L}\big\rangle = \mathbf{I}\big|\Psi_\text{R}\big\rangle \,. \tag{2.105}$$

Now we have to deal with the response $\big|\psi^\text{r}\big\rangle$. We express $\big|\psi^\text{r}\big\rangle$ in terms of the wavefunction $\big|\Psi_\text{C}\big\rangle$ by inserting Eq. (2.98) into Eq. I from Eqs. (2.101)

$$\mathbf{V}_\text{LC}\big|\Psi_\text{C}\big\rangle = [E\mathbf{S}_\text{L} - \mathbf{H}_\text{L}]\left(\big|\psi_\text{L}\big\rangle + \big|\psi^\text{r}\big\rangle\right) = \underbrace{[E\mathbf{S}_\text{L} - \mathbf{H}_\text{L}]\big|\psi_\text{L}\big\rangle}_{\mathbf{0}} + [E\mathbf{S}_\text{L} - \mathbf{H}_\text{L}]\big|\psi^\text{r}\big\rangle \,. \tag{2.106}$$

We identify the expression in brackets once again as the inverse of the matrix Green's function of the left electrode. Multiplying the matrix Green's function from the left and inserting the resulting equation into Eq. (2.98) we get

$$\big|\Psi_\text{L}\big\rangle = \big|\psi_\text{L}\big\rangle + \mathbf{G}_\text{L}\mathbf{V}_\text{LC}\big|\Psi_\text{C}\big\rangle \,. \tag{2.107}$$

We combine the results from Eqs. (2.104), (2.105) and (2.107) and write the wavefunctions $\big|\Psi_\text{L}\big\rangle$, $\big|\Psi_\text{C}\big\rangle$ and $\big|\Psi_\text{R}\big\rangle$ in terms of the eigenfunction of the left electrode

$$\begin{aligned} \text{I} &: \mathbf{I}\big|\Psi_\text{L}\big\rangle = (\mathbf{I} + \mathbf{G}_\text{L}\mathbf{V}_\text{LC}\mathbf{G}_\text{C}\mathbf{V}_\text{CL})\big|\psi_\text{L}\big\rangle \\ \text{II} &: \mathbf{I}\big|\Psi_\text{C}\big\rangle = \mathbf{G}_\text{C}\mathbf{V}_\text{CL}\big|\psi_\text{L}\big\rangle \\ \text{III} &: \mathbf{I}\big|\Psi_\text{R}\big\rangle = \mathbf{G}_\text{R}\mathbf{V}_\text{RC}\mathbf{G}_\text{C}\mathbf{V}_\text{CL}\big|\psi_\text{L}\big\rangle \,. \end{aligned} \tag{2.108}$$

Using these results we calculate the current across the central region. In the case that the central region contains no electron source or drain, the total current has to fulfill the condition

$$0 = j_\text{L} + j_\text{R} \,, \tag{2.109}$$

with

$$j_{\mathrm{l}} = i\Big[\big\langle\Psi_{\mathrm{C}}\big|\mathbf{V}_{\mathrm{Cl}}\big|\Psi_{\mathrm{l}}\big\rangle - \big\langle\Psi_{\mathrm{l}}\big|\mathbf{V}_{\mathrm{Cl}}^{\dagger}\big|\Psi_{\mathrm{C}}\big\rangle\Big] \,, \tag{2.110}$$

where $\mathrm{l} \in \{\mathrm{L},\mathrm{R}\}$. The first term in Eq. (2.110) describes the probability of an electron being initially in the state $\big|\Psi_{\mathrm{l}}\big\rangle$ and "hopping" into the state $\big|\Psi_{\mathrm{C}}\big\rangle$, while the second term describes the probability of an electron being initially in the state $\big|\Psi_{\mathrm{C}}\big\rangle$ and "hopping" into the state $\big|\Psi_{\mathrm{l}}\big\rangle$. Therefore Eq. (2.110) describes the probability of an electron flowing from the electrode into the central region reduced by the probability of an electron flowing from the central region into the electrode.

Using Eqs. (2.108) we calculate j_{L} and j_{R} from the eigenfunction $\big|\psi_{\mathrm{L}}\big\rangle$ only. In the former case we have to consider also the reflected part of the wavefunction $\big|\Psi_{\mathrm{L}}\big\rangle$. Therefore we calculate the current from j_{R}. We get

$$j_{\mathrm{R}} = -j_{\mathrm{L}} = i\Big[\big\langle\Psi_{\mathrm{C}}\big|\mathbf{V}_{\mathrm{CR}}\big|\Psi_{\mathrm{R}}\big\rangle - \big\langle\Psi_{\mathrm{R}}\big|\mathbf{V}_{\mathrm{CR}}^{\dagger}\big|\Psi_{\mathrm{C}}\big\rangle\Big] \,. \tag{2.111}$$

By using Eqs. (2.108) we express $\big|\Psi_{\mathrm{C}}\big\rangle$ and $\big|\Psi_{\mathrm{R}}\big\rangle$ in terms of the left electrode's eigenfunction

$$\begin{aligned} j_{\mathrm{R}} &= i\left[\big\langle\psi_{\mathrm{L}}\big|\mathbf{V}_{\mathrm{CL}}^{\dagger}\mathbf{G}_{\mathrm{C}}^{\dagger}\mathbf{V}_{\mathrm{CR}}\mathbf{G}_{\mathrm{R}}\mathbf{V}_{\mathrm{RC}}\mathbf{G}_{\mathrm{C}}\mathbf{V}_{\mathrm{CL}}\big|\psi_{\mathrm{L}}\big\rangle - \big\langle\psi_{\mathrm{L}}\big|\mathbf{V}_{\mathrm{CL}}^{\dagger}\mathbf{G}_{\mathrm{C}}^{\dagger}\mathbf{V}_{\mathrm{RC}}^{\dagger}\mathbf{G}_{\mathrm{R}}^{\dagger}\mathbf{V}_{\mathrm{CR}}^{\dagger}\mathbf{G}_{\mathrm{C}}\mathbf{V}_{\mathrm{CL}}\big|\psi_{\mathrm{L}}\big\rangle\right] \\ &= i\left[\big\langle\psi_{\mathrm{L}}\big|\mathbf{V}_{\mathrm{CL}}^{\dagger}\mathbf{G}_{\mathrm{C}}^{\dagger}\left(\mathbf{V}_{\mathrm{CR}}\mathbf{G}_{\mathrm{R}}\mathbf{V}_{\mathrm{RC}} - \mathbf{V}_{\mathrm{RC}}^{\dagger}\mathbf{G}_{\mathrm{R}}^{\dagger}\mathbf{V}_{\mathrm{CR}}^{\dagger}\right)\mathbf{G}_{\mathrm{C}}\mathbf{V}_{\mathrm{CL}}\big|\psi_{\mathrm{L}}\big\rangle\right] \\ &= \left[\big\langle\psi_{\mathrm{L}}\big|\mathbf{V}_{\mathrm{CL}}^{\dagger}\mathbf{G}_{\mathrm{C}}^{\dagger}\mathbf{\Gamma}_{\mathrm{R}}\mathbf{G}_{\mathrm{C}}\mathbf{V}_{\mathrm{CL}}\big|\psi_{\mathrm{L}}\big\rangle\right] \,, \end{aligned} \tag{2.112}$$

where we introduced the so-called *level-width function* $\mathbf{\Gamma}_{\mathrm{R}}$

$$\begin{aligned} \mathbf{\Gamma}_{\mathrm{R}} &= i\left(\mathbf{V}_{\mathrm{CR}}\mathbf{G}_{\mathrm{R}}\mathbf{V}_{\mathrm{RC}} - \mathbf{V}_{\mathrm{RC}}^{\dagger}\mathbf{G}_{\mathrm{R}}^{\dagger}\mathbf{V}_{\mathrm{CR}}^{\dagger}\right) \\ &= i\left(\mathbf{V}_{\mathrm{CR}}\mathbf{G}_{\mathrm{R}}\mathbf{V}_{\mathrm{RC}} - \left(\mathbf{V}_{\mathrm{CR}}\mathbf{G}_{\mathrm{R}}\mathbf{V}_{\mathrm{RC}}\right)^{\dagger}\right) \\ &= i\left(\mathbf{\Sigma}_{\mathrm{R}} - \mathbf{\Sigma}_{\mathrm{R}}^{\dagger}\right) \,. \end{aligned} \tag{2.113}$$

Now we allow the incoming electron to originate from any eigenfunction of the left electrode. Therefore we have to calculate j_{R} for each eigenfunction of the left electrode and sum all contributions. At this point we reintroduce the electron charge and the reduced Planck constant $\hbar$. We calculate the total current by

$$I_{\mathrm{R}} = \frac{e}{\hbar}\sum_{\lambda} j_{\mathrm{R}\lambda} f_{\mathrm{L}}(E_{\lambda}, \mu_{\mathrm{L}}, T_{\mathrm{L}}) \,, \tag{2.114}$$

where λ denotes the summation over the eigenfunctions of the left electrode. The Fermi-Dirac distribution

$$f(E,\mu,T) = \frac{1}{1+\mathrm{e}^{\beta(E-\mu)}} \qquad \text{with} \qquad \beta = \frac{1}{k_{\mathrm{B}}T} \tag{2.115}$$

takes into account the population of the eigenfunctions of the left electrode.

Alternatively, the electrical current into the central region can be calculated from the Landauer formula

$$I_{\mathrm{R}} = \frac{e}{2\pi\hbar}\int_{-\infty}^{+\infty} T(E) f_{\mathrm{L}}(E,\mu_{\mathrm{L}},T_{\mathrm{L}})dE\,. \tag{2.116}$$

We use these two expressions for the current to find a relation between the matrix Green's functions and the transmission. The two expressions have to yield the same current and therefore

$$T(E) = 2\pi\sum_{\lambda}\delta(E-E_\lambda)\big\langle\psi_\lambda\big|\mathbf{V}_{\mathrm{CL}}^{\dagger}\mathbf{G}_{\mathrm{C}}^{\dagger}\mathbf{\Gamma}_{\mathrm{R}}\mathbf{G}_{\mathrm{C}}\mathbf{V}_{\mathrm{CL}}\big|\psi_\lambda\big\rangle\,. \tag{2.117}$$

We insert the identity (2.29) of the left electrode subspace in the eigenbasis of the left electrode into Eq. (2.117) and get

$$\begin{aligned} T(E) &= 2\pi\sum_{\lambda}\delta(E-E_\lambda)\big\langle\psi_\lambda\big|\mathbf{V}_{\mathrm{CL}}^{\dagger}\left(\sum_{\gamma}\big|\psi_\gamma\big\rangle\big\langle\psi_\gamma\big|\right)\mathbf{G}_{\mathrm{C}}^{\dagger}\mathbf{\Gamma}_{\mathrm{R}}\mathbf{G}_{\mathrm{C}}\mathbf{V}_{\mathrm{CL}}\big|\psi_\lambda\big\rangle \\ &= 2\pi\sum_{\gamma,\lambda}\delta(E-E_\lambda)\big\langle\psi_\gamma\big|\mathbf{G}_{\mathrm{C}}^{\dagger}\mathbf{\Gamma}_{\mathrm{R}}\mathbf{G}_{\mathrm{C}}\mathbf{V}_{\mathrm{CL}}\big|\psi_\lambda\big\rangle\big\langle\psi_\lambda\big|\mathbf{V}_{\mathrm{CL}}^{\dagger}\big|\psi_\gamma\big\rangle \\ &= \sum_{\gamma}\big\langle\psi_\gamma\big|\mathbf{G}_{\mathrm{C}}^{\dagger}\mathbf{\Gamma}_{\mathrm{R}}\mathbf{G}_{\mathrm{C}}\mathbf{V}_{\mathrm{CL}}\left(2\pi\sum_{\lambda}\delta(E-E_\lambda)\big|\psi_\lambda\big\rangle\big\langle\psi_\lambda\big|\right)\mathbf{V}_{\mathrm{CL}}^{\dagger}\big|\psi_\gamma\big\rangle\,. \end{aligned} \tag{2.118}$$

The expression in brackets is another notation for the difference $i\left(\mathbf{G}_{\mathrm{L}}-\mathbf{G}_{\mathrm{L}}^{\dagger}\right)$ in the eigenbasis of $\mathbf{H}_{\mathrm{L}}$, as we will see in the following section. We use this expression and write

$$\boxed{T(E) = i\big\langle\psi_\gamma\big|\mathbf{G}_{\mathrm{C}}^{\dagger}\mathbf{\Gamma}_{\mathrm{R}}\mathbf{G}_{\mathrm{C}}\mathbf{V}_{\mathrm{CL}}\left(\mathbf{G}_{\mathrm{L}}-\mathbf{G}_{\mathrm{L}}^{\dagger}\right)\mathbf{V}_{\mathrm{CL}}^{\dagger}\big|\psi_\gamma\big\rangle = \mathrm{Tr}\left(\mathbf{G}_{\mathrm{C}}^{\dagger}\mathbf{\Gamma}_{\mathrm{R}}\mathbf{G}_{\mathrm{C}}\mathbf{\Gamma}_{\mathrm{L}}\right)}\,. \tag{2.119}$$

We get formally equivalent results for an incoming wavefunction at the right electrode. We get the total current I_{T} by subtracting the currents I_{L} and I_{R}

$$\boxed{I_{\mathrm{T}} = I_{\mathrm{R}} - I_{\mathrm{L}} = \frac{e}{2\pi\hbar}\int_{-\infty}^{+\infty} T(E)\big[f_{\mathrm{L}}(E,\mu_{\mathrm{L}},T_{\mathrm{L}}) - f_{\mathrm{R}}(E,\mu_{\mathrm{R}},T_{\mathrm{R}})\big]dE}\,. \tag{2.120}$$

2.4.4 Spectral function and Density Of States

Using the retarded and advanced matrix Green's function other helpful functions can be calculated. One of them being the *spectral function*

$$\boxed{A(E) = \frac{i}{2\pi}\mathrm{Tr}\Big(\mathbf{S}\mathbf{G}(E) - \mathbf{G}^{\dagger}(E)\mathbf{S}^{\dagger}\Big) = -\frac{1}{\pi}\mathrm{Tr}\left(\mathrm{Im}\Big(\mathbf{S}\mathbf{G}(E)\Big)\right) = -\frac{1}{\pi}\mathrm{Im}\left(\mathrm{Tr}\Big(\mathbf{S}\mathbf{G}(E)\Big)\right)}\,. \tag{2.121}$$

We show now that the spectral function (2.121) is equivalent to the density of states (DOS) of the system. We start by transforming Eq. (2.43) to the eigenbasis of the Hamiltonian matrix

$$[E^{+}\mathbf{I}-\mathbf{H}_{\mathrm{D}}]\mathbf{G}_{\mathrm{D}}(E)=\mathbf{I} \tag{2.122}$$

with

$$\mathbf{G}_{\mathrm{D}}(E)=\mathbf{U}_{\mathrm{H}}^{-1}\tilde{\mathbf{G}}(E)\mathbf{U}_{\mathrm{H}} \tag{2.123}$$

and $\mathbf{H}_{\mathrm{D}}$ being a diagonal matrix with the matrix elements $(\mathbf{H}_{\mathrm{D}})_{ii}=\varepsilon_i^{\mathrm{H}}$, where the $\varepsilon_i^{\mathrm{H}}$ are the eigenenergies of the Hamiltonian matrix of the system. $\mathbf{U}_{\mathrm{H}}$ is an unitary transformation matrix diagonalizing $\tilde{\mathbf{H}}$. The individual equations in Eq. (2.122) have the form

$$[E^{+}-\varepsilon_i^{\mathrm{H}}]\Big(\mathbf{G}_{\mathrm{D}}\Big)_{ii}=1\,. \tag{2.124}$$

Using Eq. (2.124) the spectral function becomes

$$\begin{aligned}
A(E) &= -\frac{1}{\pi}\sum_i \mathrm{Im}\left(\Big(\mathbf{G}_{\mathrm{D}}\Big)_{ii}\right)\\
&= -\frac{1}{\pi}\sum_i \mathrm{Im}\left(\frac{1}{E-\varepsilon_i^{\mathrm{H}}+i0^{+}}\right)\\
&= -\frac{1}{\pi}\sum_i \mathrm{Im}\left(\frac{E-\varepsilon_i^{\mathrm{H}}-i0^{+}}{(E-\varepsilon_i^{\mathrm{H}})^2+(0^{+})^2}\right)\\
&= \frac{1}{\pi}\sum_i \frac{0^{+}}{(E-\varepsilon_i^{\mathrm{H}})^2+(0^{+})^2}=\sum_i \delta(E-\varepsilon_i^{\mathrm{H}})=\mathrm{DOS}(E)\,.
\end{aligned} \tag{2.125}$$

We identify the sum over the delta distribution as the partition function of the system in the microcanonical ensemble. The spectral function in the eigenbasis of the Hamiltonian matrix is therefore the DOS. We take advantage of the orthonormality of the eigenfunctions ($\mathbf{S}=\mathbf{I}$) and calculate the spectral function in the eigenbasis of the Hamiltonian matrix using the expression within brackets in the last line of Eq. (2.118). By doing so we get the same result as in Eq. (2.125) showing that it is indeed an alternative notation for the difference of the retarded and advanced matrix Green's function. We calculate now the DOS of a non-orthonormal basis. Using the invariance of the trace under cyclic permutations we get

$$\begin{aligned}
\mathrm{DOS}(E) &= -\frac{1}{\pi}\mathrm{Im}\left(\mathrm{Tr}\left(\mathbf{G}_{\mathrm{D}}(E)\right)\right)\\
&= -\frac{1}{\pi}\mathrm{Im}\left(\mathrm{Tr}\Big(\mathbf{U}_{\mathrm{H}}^{-1}\left(\mathbf{O}_{\mathrm{S}}^{\mathrm{R}}\right)^{-1}\mathbf{G}(E)\left(\mathbf{O}_{\mathrm{S}}^{\mathrm{L}}\right)^{-1}\mathbf{U}_{\mathrm{H}}\Big)\right)\\
&= -\frac{1}{\pi}\mathrm{Im}\left(\mathrm{Tr}\Big(\underbrace{\left(\mathbf{O}_{\mathrm{S}}^{\mathrm{L}}\right)^{-1}\left(\mathbf{O}_{\mathrm{S}}^{\mathrm{R}}\right)^{-1}}_{\mathbf{S}}\mathbf{G}(E)\Big)\right)=-\frac{1}{\pi}\mathrm{Im}\Big(\mathrm{Tr}\Big(\mathbf{S}\mathbf{G}(E)\Big)\Big)\,.
\end{aligned} \tag{2.126}$$

We see that the matrix Green's function has to be multiplied by the overlap matrix to get the DOS in the case of a non-orthonormal basis.

2.4.4.1 Spectral function in transport systems

The spectral function of the central region is decomposed in the left spectral function, the right spectral function and a contribution from the bound states [22]

$$\boxed{A_{\mathrm{C}} = A_{\mathrm{L}} + A_{\mathrm{R}} + \sum_{n}^{bound} \alpha_n \delta(E - \varepsilon_n)} \,. \tag{2.127}$$

with $\alpha_n = \langle \phi_n | \mathbf{S}_{\mathrm{C}} | \phi_n \rangle$, where the $|\phi_n\rangle$ are the eigenfunctions of the system. The left and right spectral function are defined as

$$A_{\mathrm{j}} = \frac{i}{2\pi} \mathrm{Tr}\left(\mathbf{G}_{\mathrm{C}} \left(\mathbf{\Sigma}_{\mathrm{j}} - \mathbf{\Sigma}_{\mathrm{j}}^{\dagger} \right) \mathbf{G}_{\mathrm{C}}^{\dagger} \right) = \frac{1}{2\pi} \mathrm{Tr}\left(\mathbf{G}_{\mathrm{C}} \mathbf{\Gamma}_{\mathrm{j}} \mathbf{G}_{\mathrm{C}}^{\dagger} \right) \tag{2.128}$$

with $\mathrm{j} \in \{\mathrm{L}, \mathrm{R}\}$. We show the equality of Eqs. (2.121) and (2.127) according to Ref. [22]

$$\begin{aligned}
A_{\mathrm{C}} - (A_{\mathrm{L}} + A_{\mathrm{R}}) &= \frac{i}{2\pi} \mathrm{Tr}\left(\mathbf{G}_{\mathrm{C}} - \mathbf{G}_{\mathrm{C}}^{\dagger} \right) - \frac{i}{2\pi} \mathrm{Tr}\left(\mathbf{G}_{\mathrm{C}} \left(\mathbf{\Sigma}_{\mathrm{L}} + \mathbf{\Sigma}_{\mathrm{R}} - \left(\mathbf{\Sigma}_{\mathrm{L}}^{\dagger} + \mathbf{\Sigma}_{\mathrm{R}}^{\dagger} \right) \right) \mathbf{G}_{\mathrm{C}}^{\dagger} \right) \\
&= \frac{i}{2\pi} \mathrm{Tr}\left(\mathbf{G}_{\mathrm{C}} - \mathbf{G}_{\mathrm{C}}^{\dagger} \right) \\
&- \frac{i}{2\pi} \mathrm{Tr}\left(\mathbf{G}_{\mathrm{C}} \left(E^{+} \mathbf{S}_{\mathrm{C}} - \mathbf{H}_{\mathrm{C}} - (\mathbf{G}_{\mathrm{C}})^{-1} - \left(E^{-} \mathbf{S}_{\mathrm{C}} - \mathbf{H}_{\mathrm{C}} - \left(\mathbf{G}_{\mathrm{C}}^{\dagger} \right)^{-1} \right) \right) \mathbf{G}_{\mathrm{C}}^{\dagger} \right) \\
&= \frac{i}{2\pi} \mathrm{Tr}\left(\mathbf{G}_{\mathrm{C}} - \mathbf{G}_{\mathrm{C}}^{\dagger} \right) - \frac{i}{2\pi} \mathrm{Tr}\left(\underbrace{(E^{+} - E^{-})}_{2i0^{+}} \mathbf{G}_{\mathrm{C}} \mathbf{S}_{\mathrm{C}} \mathbf{G}_{\mathrm{C}}^{\dagger} + \mathbf{G}_{\mathrm{C}} - \mathbf{G}_{\mathrm{C}}^{\dagger} \right) \\
&= \frac{0^{+}}{\pi} \mathrm{Tr}\left(\mathbf{G}_{\mathrm{C}} \mathbf{S}_{\mathrm{C}} \mathbf{G}_{\mathrm{C}}^{\dagger} \right) \,,
\end{aligned} \tag{2.129}$$

where we substituted the hybridization matrices solving Eq. (2.53) and its complex conjugated for the hybridization matrices. We described the spectral function A_{C} using Eq. (2.121). Now we calculate the trace in the eigenbasis of the system. We insert the identity $\mathbf{I}$ twice and get

$$\begin{aligned}
\frac{0^{+}}{\pi} \sum_{n} \langle \phi_n | \mathbf{G}_{\mathrm{C}} \mathbf{S}_{\mathrm{C}} \mathbf{G}_{\mathrm{C}}^{\dagger} | \phi_n \rangle &= \frac{0^{+}}{\pi} \sum_{n,m,m'} \langle \phi_n | \overbrace{\mathbf{G}_{\mathrm{C}} | \phi_m \rangle}^{\frac{|\phi_m\rangle}{(E+i0^{+})-\varepsilon_m}} \langle \phi_m | \mathbf{S}_{\mathrm{C}} | \phi_{m'} \rangle \langle \phi_{m'} | \overbrace{\mathbf{G}_{\mathrm{C}}^{\dagger} | \phi_n \rangle}^{\frac{|\phi_n\rangle}{(E-i0^{+})-\varepsilon_n}} \\
&= \frac{0^{+}}{\pi} \sum_{n,m,m'} \frac{\delta_{m,n}}{(E + i0^{+}) - \varepsilon_m} \langle \phi_m | \mathbf{S}_{\mathrm{C}} | \phi_{m'} \rangle \frac{\delta_{n,m'}}{(E - i0^{+}) - \varepsilon_n} \\
&= \frac{0^{+}}{\pi} \sum_{n} \langle \phi_n | \mathbf{S}_{\mathrm{C}} | \phi_n \rangle \frac{1}{(E - \varepsilon_n)^2 + (0^{+})^2} = \sum_{n}^{\mathrm{bound}} \alpha_n \delta(E - \varepsilon_n) \,,
\end{aligned} \tag{2.130}$$

where we took advantage of the orthonormality of the eigenfunctions. The α_n on the right-hand side of Eq. (2.130) contains only the parts of the eigenfunctions $|\phi_n\rangle$ within the central region. Only an infinitesimal part of scattering states is within the central region. Therefore scattering states provide only an infinitesimal contribution.

2.5 Transport systems out of equilibrium

In thermodynamical equilibrium, both electrodes have the same temperature and chemical potential and according to Eq. (2.120) the current is zero due to

$$f_{\mathrm{L}}(E,\mu_{\mathrm{L}},T_{\mathrm{L}}) = f_{\mathrm{R}}(E,\mu_{\mathrm{R}},T_{\mathrm{R}}) = f(E,\mu,T)\,, \tag{2.131}$$

where f_{L} and f_{R} are the Fermi-Dirac distributions (2.115) of the left and right electrode, respectively. Fig. 2.5a shows a system in thermodynamical equilibrium at zero temperature. The energy bands of the left and right electrode are occupied up to the chemical potential μ. Similarly, in the central region, only the molecular energy levels lower than μ are filled.

We have two possibilities of driving a system out of equilibrium: the first being a difference in the temperature of the electrodes and the second being a bias voltage. In the former case more electrodes of the hotter electrode are occupying energetically higher states than in the colder electrode resulting in a non-equilibrium. Fig. 2.5b shows a thermal non-equilibrium, where the left electrode has finite temperature, while the right electrode has zero temperature. We discuss the latter case in the following in more detail.

A bias voltage $\mathrm{U_B}$ gives rise to an additional contribution to the potential of the system. Within a simple model this additional electrical potential can be taken into account by shifting the onsite energy accordingly [21]

$$\boxed{\hat{H}^{\mathrm{NEQ}} = \sum_{\substack{i,j\\ i\neq j}} t_{ij}\hat{a}_i^{\dagger}\hat{a}_j + \sum_i \left(\varepsilon_i + e\varphi_i\right)\hat{n}_i}\,, \tag{2.132}$$

where e is the electron charge and φ_i is the electrical potential of the orbital i. Using this model Hamiltonian we calculate now the DOS of a system subject to a bias voltage. For simplicity we assume the contributions of the bias voltage to the potential of the electrodes to be constant along the transport direction, meaning the bias voltage drops entirely in the central region. We also assume the coupling of the electrodes to the central region to be zero. Using this assumptions we calculate the electrode DOS from

$$\mathrm{DOS}_{\mathrm{elec}}(E) = -\frac{1}{\pi}\mathrm{Im}\left(\mathrm{Tr}\left(\left[E\mathbf{I} - \tilde{\mathbf{H}}_{\mathrm{elec}}^{\mathrm{NEQ}}\right]^{-1}\right)\right) = -\frac{1}{\pi}\mathrm{Im}\left(\mathrm{Tr}\left(\left[(E-e\varphi_i)\,\mathbf{I} - \tilde{\mathbf{H}}_{\mathrm{elec}}\right]^{-1}\right)\right)\,. \tag{2.133}$$

We see from this calculation that the bias voltage shifts the electrode DOS and in further consequence the chemical potential. Fig. 2.5c shows a system influenced by a bias voltage.

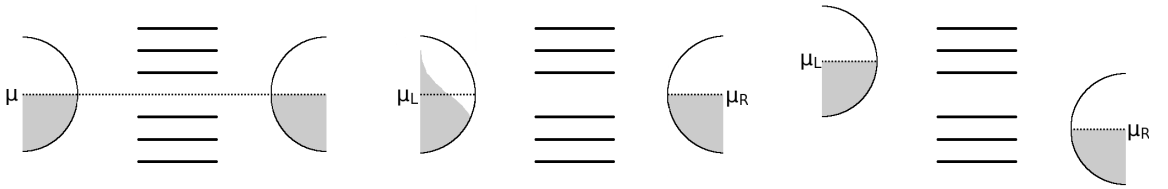

(a) Equilibrium at $T = 0\,\mathrm{K}$ **(b)** Thermal non-equilibrium **(c)** Chemical non-equilibrium

Fig. 2.5. Transport system in and out of equilibrium, where the electrodes are assumed to be semi-infinite 1D chains. The semicircles represent the electrode DOS and the gray areas mark the filled states.

2.6 Destructive quantum interference

Destructive quantum interference is an inherent quantum mechanical effect arising from the geometry of a molecule and its symmetry. By limiting oneself to hydrocarbon molecules and a treatment of these hydrocarbon molecules within the Hückel approximation a set of rules can be derived, which allow a visual assessment of whether destructive quantum interference (DQI) will be observed or not, using the *graphical atomic orbital scheme* (GAOS).

For the GAOS to be applicable, the molecule in question has to

1. couple only through *one* orbital at side l and *one* at side r to the electrodes.
2. be described sufficiently well by a Hückel model.

We derive the GAOS in Sec. 2.6.1 and explain it and its limitations in Sec. 2.6.2 by applying it to benzene, which we contact once at sites *1* and *3* and once at sites *1* and *4*. In Sec. 2.6.3 we discuss the generalization of the GAOS.

2.6.1 Derivation of the GAOS

Using the concepts introduced up to now, we derive the GAOS according to Ref. [6]. We use Eq. (2.102) to shorten the notation in the following. The left electrode couples only at site l and the right electrode only at site r. Therefore the matrix elements of the matrices $\mathbf{V}_{\mathrm{CL}}$ and $\mathbf{V}_{\mathrm{CR}}$, which couple the electrodes and the molecule, are zero except for the lth and rth row, respectively. Likewise, the columns of the matrices $\mathbf{V}_{\mathrm{LC}}$ and $\mathbf{V}_{\mathrm{RC}}$ are zero except for the lth and rth column. We get for the matrix elements of the matrices $\mathbf{V}_{\mathrm{LC}}$ and $\mathbf{V}_{\mathrm{CL}}$, and similarly for the matrices $\mathbf{V}_{\mathrm{RC}}$ and $\mathbf{V}_{\mathrm{CR}}$,

$$(\mathbf{V}_{\mathrm{CL}})_{ij} \propto \delta_{il} \,, \tag{2.134}$$

where δ is the Kronecker-Delta. We calculate now the hybridization matrices according to Eqs. (2.56) and (2.57). We find for the elements of the hybridization matrices

$$(\mathbf{\Sigma}_{\mathrm{L}})_{ij} \propto \delta_{il}\delta_{jl} \tag{2.135}$$

$$(\mathbf{\Sigma}_{\mathrm{R}})_{ij} \propto \delta_{ir}\delta_{jr} \,. \tag{2.136}$$

The only non-zero elements in the hybridization matrices are $(\mathbf{\Sigma}_{\mathrm{L}})_{ll}$ and $(\mathbf{\Sigma}_{\mathrm{R}})_{rr}$ and in consequence the matrix elements $(\mathbf{\Gamma}_{\mathrm{L}})_{ll}$ and $(\mathbf{\Gamma}_{\mathrm{R}})_{rr}$ are the only non-zero elements of the level-width functions. We use this result and Eq. (2.119) to calculate the transmission

$$\begin{aligned} T(E) &= \sum_{i,j,k,m} \left(\mathbf{G}_{\mathrm{C}}^{\dagger}\right)_{ij} (\mathbf{\Gamma}_{\mathrm{R}})_{jk} (\mathbf{G}_{\mathrm{C}})_{km} (\mathbf{\Gamma}_{\mathrm{L}})_{mi} \\ &= (\mathbf{\Gamma}_{\mathrm{L}})_{ll} (\mathbf{\Gamma}_{\mathrm{R}})_{rr} \left(\mathbf{G}_{\mathrm{C}}^{\dagger}\right)_{lr} (\mathbf{G}_{\mathrm{C}})_{rl} \\ &= (\mathbf{\Gamma}_{\mathrm{L}})_{ll} (\mathbf{\Gamma}_{\mathrm{R}})_{rr} \left| (\mathbf{G}_{\mathrm{C}})_{rl} \right|^2 . \end{aligned} \tag{2.137}$$

For the transmission to vanish, either the $\mathbf{\Gamma}_\mathrm{i}$, with $\mathrm{i} \in \{\mathrm{L}, \mathrm{R}\}$, or the Green's function must vanish. We are interested in the case where the transmission vanishes due to quantum mechanical effects arising from the properties of the molecule in the central region. Therefore the Green's function has to vanish and we get the requirement

$$(\mathbf{G}_\mathrm{C})_{rl} \stackrel{!}{=} 0 \quad \text{for DQI} \,. \tag{2.138}$$

We observe that Eq. (2.53) has to be fulfilled column-wise

$$\left[E^+\mathbf{S} - \mathbf{H} - \mathbf{\Sigma}_\mathrm{L} - \mathbf{\Sigma}_\mathrm{R}\right] \vec{\mathbf{G}}_i = \vec{\mathbf{I}}_i \,, \tag{2.139}$$

where $\vec{\mathbf{G}}_i$ and $\vec{\mathbf{I}}_i$ are the ith column of the matrix Green's function and the identity matrix, respectively. *Cramer's rule* provides a way for solving equations of the form

$$\mathbf{A}\vec{x} = \vec{y} \tag{2.140}$$

for the unknown vector $\vec{x}$. According to Cramer's rule the elements of $\vec{x}$ are calculated by

$$x_i = \frac{\det\left(\mathbf{A}_i\right)}{\det(\mathbf{A})} \,, \tag{2.141}$$

where $\mathbf{A}_i$ is the matrix, which results from replacing the ith column of $\mathbf{A}$ by $\vec{y}$. Now we calculate the Green's function $(\mathbf{G}_\mathrm{C})_{rl}$ from Eq. (2.139) using Cramer's rule. We replace the rth column of the matrix $(E^+\mathbf{S} - \mathbf{H} - \mathbf{\Sigma}_\mathrm{L} - \mathbf{\Sigma}_\mathrm{R})$ by the lth column of the identity matrix and get the new matrix $(E^+\mathbf{S} - \mathbf{H} - \mathbf{\Sigma}_\mathrm{L} - \mathbf{\Sigma}_\mathrm{R})_{l\to r}$. Now we have to evaluate

$$(\mathbf{G}_\mathrm{C})_{rl} = \frac{\det\Big(\left(E^+\mathbf{S} - \mathbf{H} - \mathbf{\Sigma}_\mathrm{L} - \mathbf{\Sigma}_\mathrm{R}\right)_{l\to r}\Big)}{\det\left(E^+\mathbf{S} - \mathbf{H} - \mathbf{\Sigma}_\mathrm{L} - \mathbf{\Sigma}_\mathrm{R}\right)} \,. \tag{2.142}$$

We simplify the numerator of Eq. (2.142) using the Laplace expansion

$$\det(\mathbf{A}) = \sum_{j=1}^{n} (-1)^{i+j} a_{ij} A_{ij} \,, \tag{2.143}$$

where the a_{ij} are the matrix elements of the $n \times n$ matrix $\mathbf{A}$ and the minors A_{ij} are the determinants of the matrices, which result from removing the ith row and jth column of the matrix $\mathbf{A}$. We expand the numerator in Eq. (2.142) along the rth column and get

$$\det\Big(\left(E^+\mathbf{S} - \mathbf{H} - \mathbf{\Sigma}_\mathrm{L} - \mathbf{\Sigma}_\mathrm{R}\right)_{l\to r}\Big) = \sum_{i=1}^{n} (-1)^{i+r} \delta_{il}\; M_{ir} = (-1)^{l+r} M_{lr} \,, \tag{2.144}$$

where the Kronecker delta arises from the column substitution done due to Cramer's rule. The M_{ir} are the minors of $(E^+\mathbf{S} - \mathbf{H} - \mathbf{\Sigma}_\mathrm{L} - \mathbf{\Sigma}_\mathrm{R})_{l\to r}$. By removing the lth row and rth column in Eq. (2.144) we also removed the elements $(\mathbf{\Sigma}_\mathrm{L})_{ll}$ and $(\mathbf{\Sigma}_\mathrm{R})_{rr}$ from the minors and therefore the numerator of Eq. (2.142) no longer depends on the electrodes.

We calculate the minor M_{lr} by using the Levi-Civita-symbol $\varepsilon_{i_1 i_2 \ldots i_n}$

$$M_{lr} = \varepsilon_{i_1 i_2 \ldots i_n} t'_{1 i_1} t'_{2 i_2} \ldots t'_{n i_n} \ , \tag{2.145}$$

where the i_j are atomic sites and $t'_{jk} = (E^+ \mathbf{S} - \mathbf{H})_{jk}$. The t'_{jk} can be interpreted as paths from site k to site j. Now we limit ourselves to a Hückel model and an orthonormal basis. Due to the Levi-Civita-symbol being zero if two indices are equal, we get only contributions if each site has exactly one incoming and one outgoing path, except for sites l and r. By expanding along the rth column $t_{r-1,r}$, $t_{r+1,r}$, $t_{l,l-1}$ and $t_{l,l+1}$ have been removed. As a result site l has no incoming and site r no outgoing path. The minor contains one open path and possibly one or more closed loops. Knowing this we write the minor as

$$M_{lr} = \varepsilon_{i_1 i_2 \ldots i_n} l_{\text{open}} l_1 l_2 \ldots l_{n_l} \ , \tag{2.146}$$

where l_{open} is a path connecting the carbon atoms contacted to the electrode and the l_j are closed loops with n_l being the number of closed loops. In the Hückel model each path segment contributes a factor of t and, except for the sign, we get

$$l_{\text{open}} \propto t'_{l i_1} t'_{i_1 i_2} \ldots . t'_{i_{n_{\text{open}}-1}} = (t')^{n_{\text{open}}} \tag{2.147}$$

$$l_j \propto t'_{j_1 j_2} t'_{j_2 j_3} \ldots t'_{j_{n_{l_j}} j_1} = (t')^{n_{l_j}} \ , \tag{2.148}$$

where n_{open} and n_{l_j} are the number of path segments contained in the open path and in the jth loop, respectively. In the case of an unpaired carbon atom the corresponding closed loop provides a factor of $t'_{jj} = E^+ - \varepsilon$, where ε is the onsite energy of the carbon atoms. The infinitesimal we introduced in Eq. (2.36) is close to zero and therefore we write $t'_{jj} \approx E - \varepsilon$. We see that all permutations containing unpaired carbon atoms vanish at $E = \varepsilon$. We see that only terms of the minor containing no unpaired carbon atoms can contribute to the transmission.

Using the results up to now a simple set of rules can be formulated allowing a first assessment whether DQI occurs:

1. Connect the two carbon atoms coupled to the electrodes by a continuous path.
2. Combine nearest-neighboring carbon atoms not part of this path into pairs of two or into closed loops. Each carbon atom can be part of a single loop or pair.
3. Repeat step 1 and 2 for each possible path connecting the sites coupled to the electrodes. If there is **no** path allowing the grouping of **all** carbon atoms in this manner, then DQI occurs for $E = \varepsilon$.

2.6.2 Application and breakdown of the *original* GAOS

In Fig. 2.6a all carbon atoms are either part of the path drawn between the contacted carbon atoms (red) or paired (green). Therefore no DQI should occur and the transmission will be

finite at $E = \varepsilon$. In Fig. 2.6b it is not possible to pair the remaining carbon atom. Also the path $(1 \to 2 \to 3)$ will leave three carbon atoms, which can neither be paired nor combined into a closed loop. Therefore DQI will occur and the transmission at $E = \varepsilon$ will be zero.

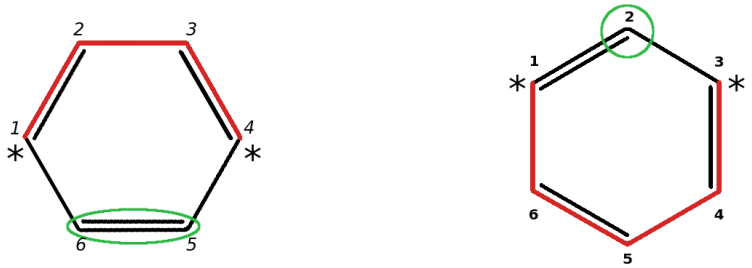

(a) No DQI predicted **(b)** DQI predicted

Fig. 2.6. Application of the original GAOS. The stars indicate the carbon sites contacted to the electrodes. We connect the sites contacted to the electrodes by a continuous path (red). Nearest-neighboring carbon atoms not part of this path have to be grouped into loops or pairs. By contacting the electrodes at sites 1 and 3 no continuous path allows the grouping of all remaining carbon atoms and the GAOS predicts DQI. Contacting the electrodes at sites 1 and 4 allows the grouping of all remaining carbon atoms and according to the GAOS no DQI should be observed.

While these original rules represent an easy way to determine when DQI occurs, they do not allow to determine if the molecular junction has a finite transmission at $E = \varepsilon$. This set of rules considers each term in Eq. (2.146) individually and therefore does not take into account a possible cancellation of different terms in Eq. (2.146).

Ref. [23] deals with molecules, in which this set of rules breaks down due to the cancellation of different terms in Eq. (2.146). One of the molecules treated in Ref. [23] is benzocyclobutadiene (BCB), which we will discuss in more detail. Fig. 2.7 shows a diagram of BCB, where all carbon atoms are either part of the path connecting the carbon atoms coupled to the electrodes or can be paired. Nevertheless, the transmission of this molecule within the Hückel model does vanish at $E = \varepsilon$.

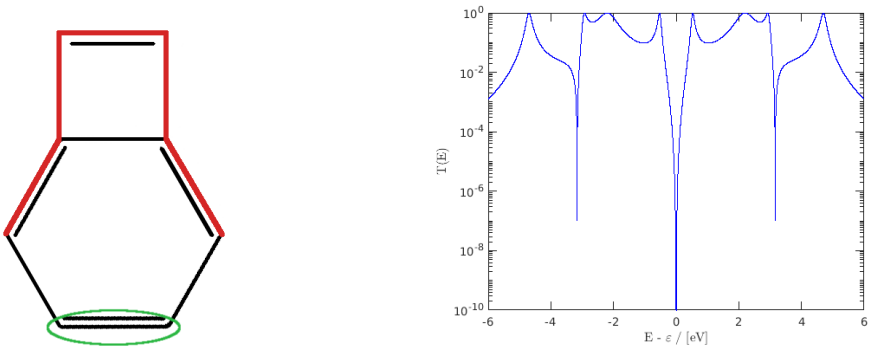

Fig. 2.7. Breakdown of the original GAOS. All remaining carbon atoms can be grouped according to the original GAOS (left) but the transmission within the Hückel model (right) still vanishes. For the calculation of the transmission we assumed an orthonormal basis and used:
$\varepsilon = 0$
$t' = -2$
$0^{+} = 2.5 \cdot 10^{-5}$
$(\mathbf{\Sigma}_{\mathrm{L}})_{\mathrm{ll}} = (\mathbf{\Sigma}_{\mathrm{R}})_{\mathrm{rr}} = -0.5i$

2.6.3 Generalization of the GAOS

While the original GAOS in Sec. 2.6.1 allows a first assessment whether DQI occurs, it does so by observing that all diagrams of the minor vanish individually. By generalizing the GAOS like in Ref. [23] one can calculate the minor from the different diagrams instead. In this generalized GAOS the sign of the diagrams is taken into account. Additionally, the different sites of hydrocarbon molecules are no longer restricted to having the same onsite energy. This allows to calculate the minor (2.146) from the different diagrams in the following way:

1. Connect the two carbon atoms coupled to the electrodes by a continuous path. Nearest-neighboring carbon atoms not part of this path can be either paired or grouped in closed loops, with each carbon atom being part of a single loop or pair.
2. Draw all possible diagrams using:
   - Unpaired carbon atoms provide a factor of $E - \varepsilon_i$
   - Each bond contained in the continuous path provides a factor of t
   - Pairs of two carbon atoms provide a factor of t^2
   - Closed loops containing n carbon atoms (with $n \geq 3$) provide a factor $2t^n$, where the factor 2 takes account for the orientation (clockwise or anticlockwise loop)
3. The sign of each diagram is $(-1)^P$, where P is the number of closed loops, including pairs of carbon atoms.
4. Add the individual contributions of all diagrams together to get the characteristic polynomial and determine its zeros.

It should be stated that there are different conventions regarding the signs of each contribution and therefore P may contain additionally the number of unpaired atoms. We have chosen the sign convention according to Ref. [23]. Fig. 2.8 demonstrates the application of these rules.

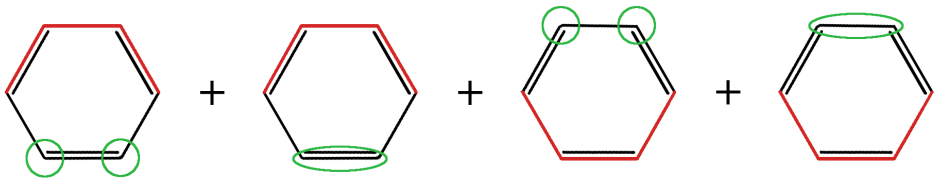

(a) All possible diagrams for benzene contacted in para position

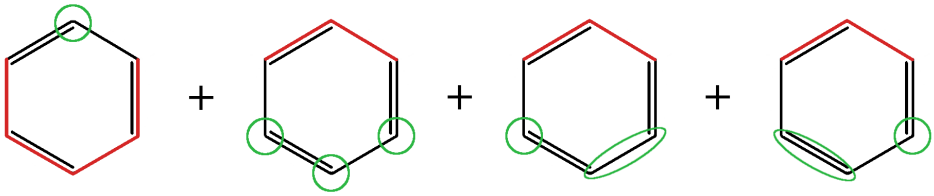

(b) All possible diagrams for benzene contacted in meta position

Fig. 2.8. Application of the generalized GAOS to benzene. We draw all possible diagrams and sum up their contribution to get the characteristic polynomial of the minor. We calculate the contribution of each diagram to the characteristic polynomial by using the generalized GAOS.

Applying the rules as defined above, the minors of the two molecules give following characteristic polynomials

$$M_{14} = (-1)^0 t^3 (E-\varepsilon)^2 + (-1)^1 t^5 + (-1)^0 t^3 (E-\varepsilon)^2 + (-1)^1 t^5 = 2t^3 (E-\varepsilon)^2 - 2t^5 \quad (2.149)$$

$$\begin{aligned} M_{13} &= (-1)^0 t^4 (E-\varepsilon) + (-1)^0 t^2 (E-\varepsilon)^3 + (-1)^1 t^4 (E-\varepsilon) + (-1)^1 t^4 (E-\varepsilon) \\ &= t^2 (E-\varepsilon)^3 - t^4 (E-\varepsilon)\,. \end{aligned} \quad (2.150)$$

It is obvious that for $E = \varepsilon$ the minor M_{13} vanishes, while the minor M_{14} is finite. We see that both minors vanish at $E - \varepsilon = \pm t$.

Using the generalized rules from this section we calculate the full minor of BCB. For simplicity we consider only diagrams explicitly, in which all carbon atoms are paired. Fig. 2.9 shows all possibilities of grouping the remaining carbon atoms into pairs or closed loops.

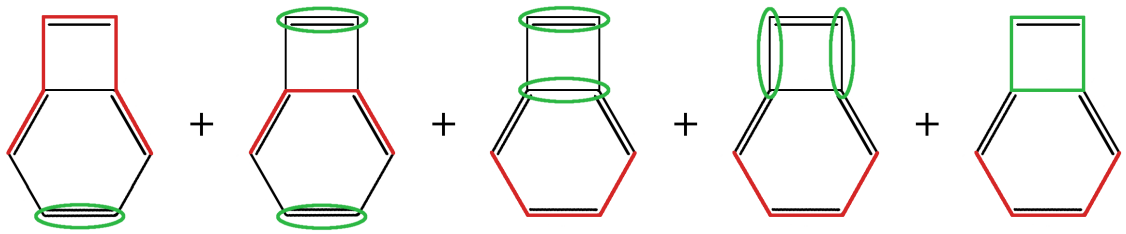

Fig. 2.9. The different diagrams of BCB grouping all carbon atoms not part of the continuous path. By calculating the characteristic polynomial from these diagrams we see that these diagrams cancel leaving only diagrams containing unpaired carbon atoms.

We calculate the minor using the rules described above and get

$$M_{\mathrm{BCB}} = (-1)^1 t^7 + (-1)^2 t^7 + (-1)^2 t^7 + (-1)^2 t^7 + (-1)^1 2t^7 + \text{remaining terms}\,. \quad (2.151)$$

Note that the factor 2 in the fifth term on the right-hand side of Eq. (2.151) results from the closed loop being once clockwise oriented and once anticlockwise. The terms we have written down explicitly cancel leaving only the "remaining terms", which are proportional to $(E - \varepsilon)$. This result solves the apparent contradiction in Fig. 2.7.

The generalizations in this section can be further extended, also allowing different hopping parameters, which will increase the mathematical cost. Also the limitation to nearest-neighbor hopping can be lifted, which will further increase the mathematical cost.

We want to point out that the GAOS does not consider the full Green's function but only the minor M_{lr}, while it leaves out the denominator in Eq. (2.142). Therefore the GAOS should be considered only for first assessment of whether DQI occurs and not as an equivalent replacement of actual calculations.

Chapter 3

Computational Methods

Fig. 3.1 shows the scheme of the procedure we follow in this work. We use for the first-principles calculations the DFT code SIESTA [24], its DFT+NEGF code TranSIESTA [7, 8] and the post-processing tool TBtrans [8]. Using SIESTA, we relax the structures of the systems and calculate the electron density self-consistently, once for the central region and once for the electrodes. Using TranSIESTA, we calculate the electron density of the transport system from the results of the SIESTA calculations. Using TBtrans, we calculate the transport properties of the systems from the results of the TranSIESTA calculations. Additionally, we reduce the Hamiltonian matrices gained from the TranSIESTA calculations to model Hamiltonian matrices, from which we calculate transport properties allowing further insight.

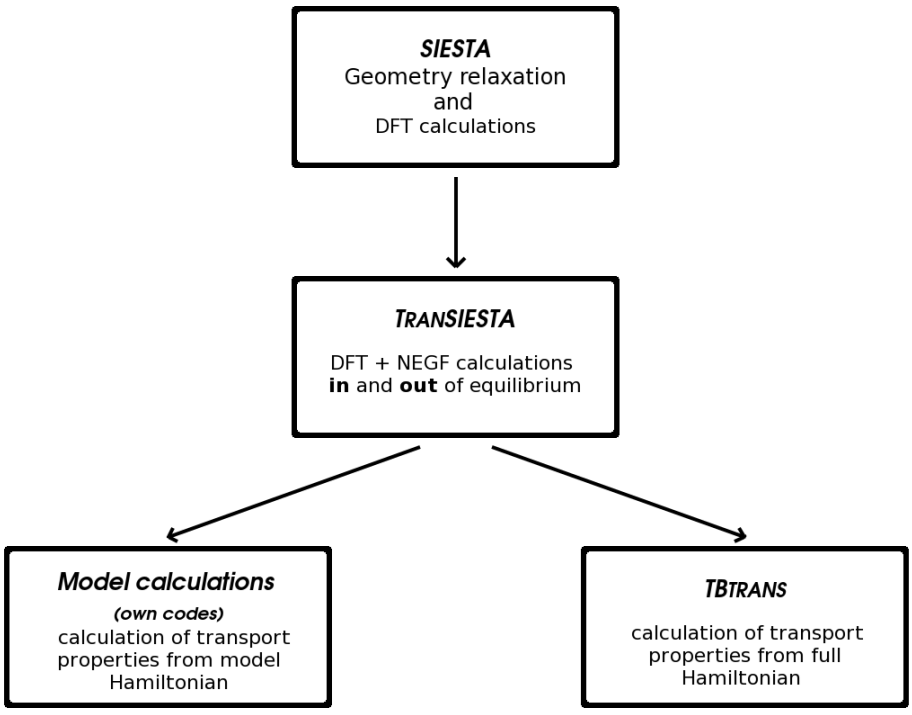

Fig. 3.1. Structure chart of the transport calculations within this thesis.

In Sec. 3.1 we discuss the DFT code SIESTA, the DFT based NEGF code TranSIESTA and the parameters we consider in the calculations. In Sec. 3.2 we will explain the details of the transport calculations using TBtrans and of the model calculations.

3.1 DFT

In Sec. 3.1.1 we discuss the DFT code SIESTA. We explain in Sec. 3.1.2 how the DFT+NEGF code TranSIESTA calculates transport systems from the SIESTA results. Sec. 3.1.3 deals with the parameters we consider in the SIESTA and TranSIESTA calculations.

3.1.1 SIESTA

SIESTA [24] is an open-source code using atomic orbitals. Due to the localization of the atomic orbitals, many entries of the Hamiltonian matrix and the overlap matrix are zero or close to zero. This sparsity of the Hamiltonian matrix and overlap matrix allows the implementation of order-N algorithms and functionals. Moreover the usage of atomic orbitals allows for directly calculating the transport systems being neither periodic nor finite systems. In contrast plane-wave-based codes require the systems to be periodic structures due to the periodicity of the plane waves.

Basis set

By using spherical coordinates an atomic Hamiltonian can be split up into a radial and an angular part allowing a product ansatz for the wavefunction of the form $\Psi(r, \Theta, \phi) = R(r)Y_{lm}(\Theta, \phi)$. The angular part of the solution can be described by spherical harmonics. The radial part is more difficult to calculate and is generally approximated. Two frequently used approximations are *Slater type* orbitals (STOs) and *Gaussian type* orbitals (GTOs). STOs are a good approximation for atomic orbitals but the evaluation of the appearing integrals is computationally demanding. The integrals involved using GTOs can be calculated analytically and therefore are easily dealt with, but GTOs describe atomic orbitals worse than STOs. The solution is to approximate STOs by a linear combination of several GTOs (see Sec. 2.2.1).

STOs and GTOs, per se, do not allow the treatment of some effects, like e.g. polarization effects. Further improvements can be reached by including additional orbitals to describe such effects. In SIESTA this is done by including orbitals of higher orbital angular momentum. In this case the basis set of hydrogen includes p orbitals and the basis set of carbon d orbitals and so on.

Pseudopotentials

In general, the contribution of the core electrons to chemical bonds and to transport properties is small. Therefore SIESTA treats the core electrons and their nucleus by the use of a pseudopotential. We use *norm-conserving* pseudopotential. A wavefunction resulting from such pseudopotentials is equal to the "real" all-electron wavefunction outside a given core radius and, in consequence, the norm of both wavefunctions is equal inside this core radius.

Cutoff radius

The sparsity of the Hamiltonian matrix results from either neglecting small matrix elements or introducing a cutoff radius above which the wavefunctions are strictly zero. In SIESTA the latter approach is implemented. The eigenenergies of wavefunctions confined to a finite volume are higher than in the unconfined case. This *energy shift* is specified in SIESTA and the cutoff radii of the orbitals are calculated from it resulting in different cutoff radii for the different orbitals.

Two-center integrals / grid integrals

Depending on the integrals that have to be evaluated, they are calculated either in Fourier space or in real space. Two-center integrals are calculated in Fourier space, while integrals involving potentials are calculated in real space. Therefore not only the grid in Fourier space has to be converged but also the fineness of the real space grid.

3.1.2 TranSIESTA

Using SIESTA only systems of finite size or periodic systems can be calculated. Therefore, SIESTA does not allow the treatment of typical transport systems being infinite and non-periodic. We calculate transport systems in and out of equilibrium using TranSIESTA [7, 8].

Electrodes and Central region

The transport system is split into three parts: the two electrodes and the central region, as we have discussed in Sec. 2.4. The semi-infinite electrodes are further split into identical clusters and treated using the concept of surface Green's functions presented in Sec. 2.4.2, where the surface Green's functions are calculated using the Sancho-Rubio method from Sec. 2.4.2.1. We want to note here, that according to Sec. 2.4.2 the electrode clusters are allowed to couple only to nearest-neighboring ones. Therefore the cluster size in transport direction and the cutoff radius of the electrode wavefunctions cannot be chosen independently from one another.

The partitioning of the system into electrodes and central region in TranSIESTA differs slightly from the partitioning discussed in Sec. 2.4. Except for the molecule and the electrode parts influenced by this molecule, the supercell of the central region *must* contain also at least one electrode cluster of each electrode.

The Hamiltonian matrices and overlap matrices of the electrode clusters and of the central region required to deal with the transport system using the DFT+NEGF approach (see Sec. 2.4) are gained from SIESTA calculations.

3.1.2.1 Non-equilibrium

TranSIESTA allows to drive the system out of equilibrium by the two possibilities discussed in Sec. 2.5, namely a bias voltage and a difference of the electrode temperatures, but does so in a more advanced way. For more details we refer the reader to Refs. [7, 8, 25]. We drive the systems out of equilibrium by a bias voltage and therefore we discuss this possibility in more detail. In TranSIESTA a system in non-equilibrium is calculated using a non-equilibrium potential in the Kohn-Sham Hamiltonian. This potential is determined by solving the Poisson equation. The bias voltage determines the boundary conditions of the Poisson equation.

From SIESTA to TranSIESTA

TranSIESTA requires the calculations of the electrode clusters within a SIESTA run beforehand. After the electrode clusters have been calculated, TranSIESTA starts by converging the density matrix and Hamiltonian matrix of the central region within a SIESTA calculation

(creates a xyz.DM file) before starting the actual TranSIESTA run (creates a xyz.TSDE file, TranSIESTA equivalent of the xyz.DM file). By starting with the density matrix (xyz.TSDE file) of an already existing TranSIESTA calculation, the SIESTA calculation of the central region will be skipped and the TranSIESTA calculations will start directly. The computation time can be further reduced by using the density matrix (TSDE file) of non-equilibrium situations closest to the current non-equilibrium situation, which we take advantage of in this work.

3.1.3 Parameters considered in the SIESTA and TranSIESTA calculations

SIESTA and TranSIESTA allow a variety of options and parameters to be set. Due to the vast amount of these parameters we discuss only the most important ones.

k-points and MeshCutoff

The k-points determine the fineness of the grid on the unit cell or supercell specified by the user (e.g. the central regions from Fig. 1.3) in k-space (Fourier space). Different numbers of k-points also result in different k-points used for calculations. Thus for a non-converged grid no reliable results can be obtained neither can these results be used for interpolation. The parameter MeshCutoff defines the fineness of the grid in real space. The same considerations as for the grid in k-space are valid.

BasisSize, EnergyShift and SplitNorm

A too small basis will restrict calculations, e.g. geometry relaxation, to much and will result in a bad description of the system. Therefore the basis size has to be converged. The basis size can be specified by SZ, DZ, SZP or DZP. SZ and DZ specify the usage of one basis function (single zeta) or two basis functions (double zeta) per orbital, respectively, where the basis functions are not limited to being linear combinations of Gaussians (see SIESTA manual). The basis sizes SZP (SZ + polarization) and DZP (DZ + polarization) consider additional polarization orbitals.

The parameter EnergyShift determines the cutoff radii. Forces are only present up to the cutoff radius. A too short cutoff radius can therefore yield to wrong results due to the absence of long-range forces. Also the transmission can be wrong due to too many entries in the overlap matrix and in the Hamiltonian matrix being zero.

The parameter SplitNorm determines how much of the norm of the Slater type orbital goes into the second-zeta function. A too low or too high value will result in the atom orbitals being described mainly by one of the two basis functions.

MD.MaxForceTol

MD.MaxForceTol defines the maximum force below which the geometry of the system is considered to be relaxed during structure optimization. A too large force tolerance will cause the geometry optimization to finish before the structure is sufficiently relaxed. A too small force tolerance increases the computation time.

Contour

TRANSIESTA calculates the equilibrium density matrix from the Green's function using a complex contour integral. The Green's function is smoother in the complex plane, which allows an accurate evaluation with less sampling points and also the implementation of numerically efficient methods. In the complex plane one can also take advantage of the residue theorem. For more information we refer the reader to Ref. [7, 8].

Different contours can be chosen for the calculations and depending on the choice different values have to be converged. The contour we use consists of two parts: a circle from E_{Min} to E_{max} and a tail from E_{max} to $+\infty$. To yield correct results it is important that E_{Min} is energetically lower than the lowest eigenvalue of the Hamiltonian. For numerical reasons, the number of points the two contour parts, namely the circle and tail part, are defined on has to be converged.

3.2 Transport calculations

In this section, we discuss some details of the transport calculations. In Sec. 3.2.1 we deal with the transport calculations using TBTRANS, while we explain the details of the model calculations in Sec. 3.2.2.

3.2.1 TBTRANS

TBTRANS [8] is a *post-processing* code allowing the analysis of TB Hamiltonian matrices. We will use it to analyze the results gained from the TRANSIESTA calculations. We will calculate a variety of properties using TBTRANS: the transmission, which is calculated according to Eq. (2.119), the current, which is calculated according to Eq. (2.120) and the DOS of the central region. TBTRANS allows the calculation of the DOS of the central region either by the spectral function from Eq. (2.121) or by the spectral functions of the left and right electrode from Eq. (2.127), where the latter approach is more suited for transport systems, especially in non-equilibrium. Therefore we choose the second approach.

3.2.2 Model calculations

The results from the first-principles calculations contain a large number of parameters, namely the matrix elements of the Hamiltonian matrix and the overlap matrix in the basis of all orbitals used in the calculations. Therefore we map the results onto simple models consisting of a reasonable amount of parameters but still containing the relevant physics. In Sec. 3.2.2.1 we reduce the central region of the model system to include only the parts relevant for the calculations. We describe the modeling of the electrodes in Sec. 3.2.2.2, the procedure by which we gain the parameters of the reduced central region from the TRANSIESTA calculations in Sec. 3.2.2.3 and the approximations of the models in Sec. 3.2.2.4.

3.2.2.1 Reduction of the central region

As we have seen in Sec. 2.6, DQI is a quantum effect resulting from the properties of the benzene ring. Therefore we start by splitting up the central regions of the systems from Fig. 1.3 into

three clusters as shown in Fig. 3.2: one contains all gold atoms to the left of the BDT (C_L), one contains the BDT and one contains all gold atoms to the right of the BDT (C_R).

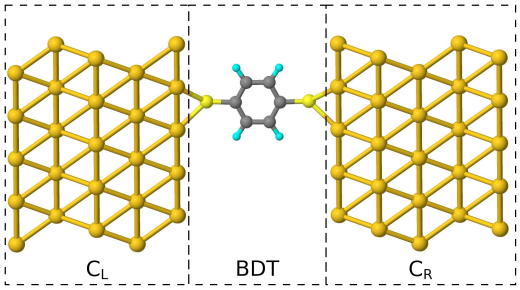

Fig. 3.2. Partitioning of the central region. We are interested in the DQI, which arises from the BDT molecule. Therefore we split the central region into the clusters C_L, BDT and C_R. For the color code see Fig. 1.3.

The Hamiltonian matrix and overlap matrix of the central regions are now of the form

$$\mathbf{H}_C = \begin{pmatrix} \mathbf{H}_{C_L} & \mathbf{V}_{C_L,BDT} & 0 \\ \mathbf{V}_{BDT,C_L} & \mathbf{H}_{BDT} & \mathbf{V}_{BDT,C_R} \\ 0 & \mathbf{V}_{C_R,BDT} & \mathbf{H}_{C_R} \end{pmatrix} \tag{3.1}$$

$$\mathbf{S}_C = \begin{pmatrix} \mathbf{S}_{C_L} & \mathbf{s}_{C_L,BDT} & 0 \\ \mathbf{s}_{BDT,C_L} & \mathbf{S}_{BDT} & \mathbf{s}_{BDT,C_R} \\ 0 & \mathbf{s}_{C_R,BDT} & \mathbf{S}_{C_R} \end{pmatrix} , \tag{3.2}$$

where $\mathbf{H}_{C_L}$, $\mathbf{H}_{BDT}$ and $\mathbf{H}_{C_R}$ are the Hamiltonian matrices of the three clusters and $\mathbf{V}_{BDT,C_j}$ and $\mathbf{V}_{C_j,BDT}$ are the coupling matrices of the clusters BDT and C_j with $j \in \{L, R\}$. Similarly, $\mathbf{S}_{C_L}$, $\mathbf{S}_{BDT}$ and $\mathbf{S}_{C_R}$ are the overlap matrices of orbitals in the same cluster, while the $\mathbf{s}_{C_j,BDT}$ and $\mathbf{s}_{BDT,C_j}$ are the overlap matrices of orbitals within neighboring clusters.

Per construction the left electrode couples only to the cluster C_L and the right electrode couples only to the cluster C_R. The clusters C_L and C_R do not couple with one another. Therefore, we are able to treat the electrodes by use of the SGF of C_L and C_R. We couple the clusters C_L and C_R to the semi-infinite electrodes in the same way as we have done in Sec. 2.4.2. We calculate the SGF of the semi-infinite electrodes using the Sancho-Rubio method and couple the resulting SGFs to the clusters C_L and C_R using Eq. (2.64). The SGF of this system is now

$$\mathbf{G}_{C_j} = \left(E^+\mathbf{S}_{C_j} - \mathbf{H}_{C_j} - \mathbf{V}_{C_j,j}\mathbf{G}_j^{SGF}\mathbf{V}_{j,C_j}\right)^{-1} , \tag{3.3}$$

where $\mathbf{G}_j^{SGF}$ is the SGF of the semi-infinite electrode j calculated by the Sancho-Rubio method. $\mathbf{V}_{C_j,j}$ and $\mathbf{V}_{j,C_j}$ are the coupling matrices of the cluster C_j and the surface cluster of the electrode j. We calculate now the matrix Green's function of the BDT from

$$\mathbf{G}^{BDT}(E) = \left[E^+\mathbf{S}^{BDT} - \mathbf{H}^{BDT} - \mathbf{\Sigma}_{C_L} - \mathbf{\Sigma}_{C_R}\right]^{-1} , \tag{3.4}$$

with the hybridization matrices

$$\mathbf{\Sigma}_{\mathrm{C_j}} = \mathbf{V}_{\mathrm{BDT,C_j}} \mathbf{G}_{\mathrm{C_j}} \mathbf{V}_{\mathrm{C_j,BDT}} \, . \tag{3.5}$$

3.2.2.2 Electrodes

We keep the modeling of the electrodes as simple as possible and consider only details of the electrodes which are necessary to yield qualitatively correct results. For simplicity we treat each electrode as an effective single site. We neglect the hopping processes between the s and d orbitals. Additionally, we describe the d orbitals by a single, effective orbital. Thus the Hamiltonian matrix of the electrode has the form

$$\mathbf{H}_{\mathrm{electrode}} = \begin{pmatrix} \varepsilon_{\mathrm{s}} & 0 \\ 0 & \varepsilon_{\mathrm{d}}^{\mathrm{eff}} \end{pmatrix}, \tag{3.6}$$

where ε_{s} is the onsite energy of the s orbital and $\varepsilon_{\mathrm{d}}^{\mathrm{eff}}$ is the onsite energy of the effective d orbital of the model electrode. The matrix Green's function resulting from this Hamiltonian matrix has the form

$$\mathbf{G}^{\mathrm{R}}_{\mathrm{electrode}}(E) = \begin{pmatrix} G^{\mathrm{R}}_{\mathrm{s}}(E) & 0 \\ 0 & G^{\mathrm{R}}_{\mathrm{d}}(E) \end{pmatrix}, \tag{3.7}$$

where $G^{\mathrm{R}}_{\mathrm{s}}(E)$ and $G^{\mathrm{R}}_{\mathrm{d}}(E)$ are the Green's functions of the s orbital and the effective d orbital, respectively. We describe the Green's function of the s orbital by [26]

$$G^{\mathrm{R}}_{\mathrm{s}}(E) = G^{\mathrm{R}}_{\mathrm{wb}}(E) = -\frac{1}{2D} \ln\left(\frac{E + i0^{+} - D}{E + i0^{+} + D}\right), \tag{3.8}$$

where $2D$ is the bandwidth. It is more adequate to describe the Green's function of the d orbitals by the Green's function of a 1D chain. Therefore we describe the d orbital by [27]

$$G^{\mathrm{R}}_{\mathrm{d}}(E) = G^{\mathrm{R}}_{\mathrm{1D}}(E) = \frac{E + i\eta - \varepsilon_0}{2|t_{\mathrm{1D}}|^2} \left[1 - \sqrt{1 - \frac{4|t_{\mathrm{1D}}|^2}{(E + i\eta - \varepsilon_0)^2}}\right], \tag{3.9}$$

where t_{1D} is the hopping parameter between nearest-neighbor atoms of the 1D chain. ε_0 is the onsite energy of the d orbital and η is the artificial broadening. Figs. 3.3a and 3.3b show the real and imaginary part of the Green's functions $G^{\mathrm{R}}_{\mathrm{wb}}(E)$ and $G^{\mathrm{R}}_{\mathrm{1D}}(E)$, respectively.

We couple each electrode to a single site of the central region and calculate the hybridization matrices

$$\Sigma_{\mathrm{jj}}(E) = \left|t_{\mathrm{S_j s_j}}\right|^2 G^{\mathrm{R}}_{\mathrm{s}}(E) + \left|t_{\mathrm{S_j d_j}}\right|^2 G^{\mathrm{R}}_{\mathrm{d}}(E) \tag{3.10}$$

with $\mathrm{j} \in \{\mathrm{l}, \mathrm{r}\}$, where l and r denote the sites contacted to the left and right electrode, respectively. $t_{\mathrm{S_j s_j}}$ and $t_{\mathrm{S_j d_j}}$ are the coupling strengths of the $\mathrm{p_z}$ orbital of sulfur, denoted by the subscript $\mathrm{S_j}$, to the s and d orbital of the corresponding electrode, denoted by the superscripts $\mathrm{s_j}$ and $\mathrm{d_j}$, respectively.

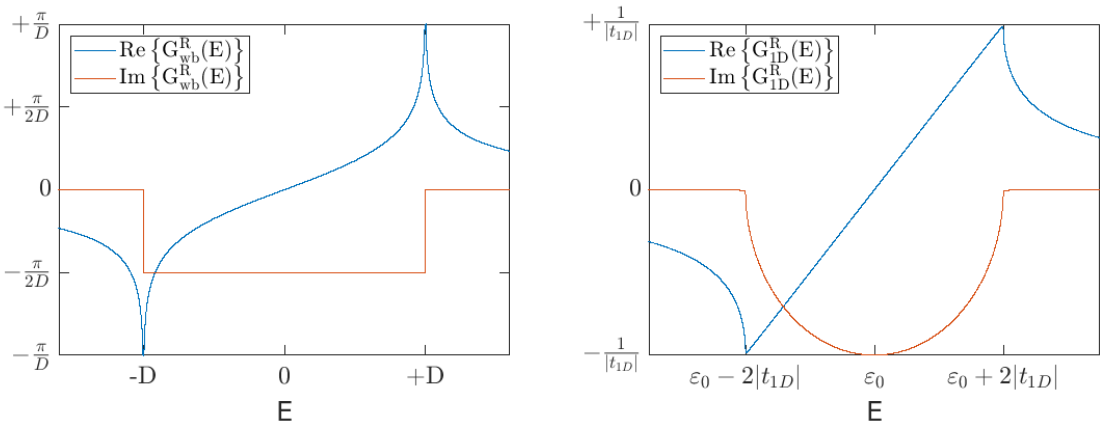

(a) We used:
$D = 25$
$0^+ = 10^{-5}$

(b) We used:
$\varepsilon_0 = 0$
$t_{1D} = 1$
$\eta = 2.5 \cdot 10^{-3}$

Fig. 3.3. Real and imaginary part of the Green's functions we use to model the s orbitals (left) and the d orbitals (right) of the electrodes.

3.2.2.3 BDT

The Hamiltonian of the first-principles calculations contains several orbitals at each site. We reduce the number of orbitals per site to one. The procedure by which we gain the model Hamiltonian from the first-principles calculations can be summarized into following three steps:

1. Keep the orbitals of interest and remove the remaining orbitals
2. Reduce the basis of the orbitals of interest to contain a single orbital per site
3. Orthogonalize the resulting basis

We describe these steps in more detail in the following section. Although the model contains only one orbital per site, we are keeping the following description general.

1. In the first step we extract the Hamiltonian matrix and overlap matrix from the first-principles calculations and keep only the orbitals of interest

$$\mathbf{X}_{\text{sub}} = \mathbf{P}^\dagger \mathbf{X} \mathbf{P}, \tag{3.11}$$

where $\mathbf{X} \in \{\mathbf{H}, \mathbf{S}\}$ is a $n_{\text{FP}} \times n_{\text{FP}}$ matrix with n_{FP} being the total number of basis functions describing the atomic orbitals in the central region of the first-principles calculations. The matrix $\mathbf{P}$ is a $n_{\text{FP}} \times n_{\text{sub}}$ matrix, where n_{sub} is the number of basis functions in the subspace, e.g. only containing the p_z orbitals. The elements of the matrix $\mathbf{P}$ are

$$\mathbf{P}_{ik_j} = \begin{cases} \delta_{ij} & \text{if } j\text{th basis function is within the subspace} \\ 0 & \text{otherwise} \end{cases} \tag{3.12}$$

with $k_j \in \{1, 2, ..., n_{\text{sub}}\}$ being the index of the jth basis function within the subspace.

The basis functions in the SIESTA and TranSIESTA calculations are ordered according to the indices of the atoms they belong to. Therefore the Hamiltonian matrix, and also the overlap matrix, have the form

$$\mathbf{H}_{\text{sub}} = \begin{pmatrix} \mathbf{H}_{\text{s}_1} & \mathbf{V}_{\text{s}_1\text{s}_2} & . & . & \mathbf{V}_{\text{s}_1\text{s}_n} \\ \mathbf{V}_{\text{s}_2\text{s}_1} & \mathbf{H}_{\text{s}_2} & \mathbf{V}_{\text{s}_2\text{s}_3} & & . \\ . & & . & & . \\ . & & & . & . \\ \mathbf{V}_{\text{s}_n\text{s}_1} & . & . & \mathbf{V}_{\text{s}_n\text{s}_{n-1}} & \mathbf{H}_{\text{s}_n} \end{pmatrix}, \tag{3.13}$$

where $\mathbf{H}_{\text{s}_i}$ is the Hamiltonian matrix of site i and the $\mathbf{V}_{\text{s}_i\text{s}_j}$ are matrices describing the hopping between sites i and j.

2. Now we transform the orbitals of the subspace such that hopping occurs only between neighboring sites but not between different orbitals at one site. We do this by finding unitary transformations that diagonalize the $\mathbf{H}_{\text{s}_i}$ and transform the $\mathbf{V}_{\text{s}_i\text{s}_j}$ accordingly. We have to solve the eigenvalue problem

$$\mathbf{H}_{\text{s}_i}\,\vec{c}_{\,\text{s}_i} = E\mathbf{S}_{\text{s}_i}\,\vec{c}_{\,\text{s}_i}, \tag{3.14}$$

where the entries of the eigenvectors $\vec{c}_{\,\text{s}_i}$ are the coefficients of the basis functions at site i. Before solving this eigenvalue problem we reduce it to a standard one. We use $\mathbf{S}_{\text{s}_i}^{-\frac{1}{2}}\mathbf{S}_{\text{s}_i}^{\frac{1}{2}} = \mathbf{I}$ and $\mathbf{S}_{\text{s}_i}^{\frac{1}{2}}\mathbf{S}_{\text{s}_i}^{\frac{1}{2}} = \mathbf{S}_{\text{s}_i}$

$$\mathbf{H}_{\text{s}_i}\mathbf{S}_{\text{s}_i}^{-\frac{1}{2}}\mathbf{S}_{\text{s}_i}^{\frac{1}{2}}\,\vec{c}_{\,\text{s}_i} = E\mathbf{S}_{\text{s}_i}^{\frac{1}{2}}\underbrace{\mathbf{S}_{\text{s}_i}^{\frac{1}{2}}\,\vec{c}_{\,\text{s}_i}}_{=:\vec{c}\,'_{\text{s}_i}}. \tag{3.15}$$

Now we multiply Eq. (3.15) from the left by $\mathbf{S}_{\text{s}_i}^{-\frac{1}{2}}$

$$\tilde{\mathbf{H}}_{\text{s}_i}\,\vec{c}\,'_{\text{s}_i} = E\,\vec{c}\,'_{\text{s}_i}, \tag{3.16}$$

where

$$\tilde{\mathbf{H}}_{\text{s}_i} = \mathbf{S}_{\text{s}_i}^{-\frac{1}{2}}\mathbf{H}_{\text{s}_i}\mathbf{S}_{\text{s}_i}^{-\frac{1}{2}}. \tag{3.17}$$

By solving the eigenvalue problem (3.16) we get the transformation matrices $\mathbf{U}_{\text{s}_i}$ diagonalizing the submatrices $\mathbf{H}_{\text{s}_i}$

$$\mathbf{U}_{\text{s}_i} = \left(\mathbf{S}_{\text{s}_i}^{-\frac{1}{2}}\vec{c}\,'^{1}_{\text{s}_i}, \mathbf{S}_{\text{s}_i}^{-\frac{1}{2}}\vec{c}\,'^{2}_{\text{s}_i}, ..., \mathbf{S}_{\text{s}_i}^{-\frac{1}{2}}\vec{c}\,'^{n_{\text{s}_i}}_{\text{s}_i}\right) = \left(\vec{c}^{\,1}_{\text{s}_i}, \vec{c}^{\,2}_{\text{s}_i}, ..., \vec{c}^{\,n_{\text{s}_i}}_{\text{s}_i}\right), \tag{3.18}$$

where n_{s_i} is the number of orbitals at site i. The $\vec{c}^{\,k}_{\text{s}_i}$ and $\vec{c}\,'^{k}_{\text{s}_i}$ with $k = 1, 2, ..., n_{\text{s}_i}$ are the normalized eigenvectors of Eqs. (3.15) and (3.16), respectively.

We define a single transformation matrix $\mathbf{U}$, which diagonalizes the $\mathbf{H}_{\mathrm{s}_i}$ and transforms the $\mathbf{V}_{\mathrm{s}_i\mathrm{s}_j}$

$$\mathbf{U} = \begin{pmatrix} \mathbf{U}_{\mathrm{s}_1} & & & \\ & \mathbf{U}_{\mathrm{s}_2} & 0 & \\ & & . & \\ & 0 & & . \\ & & & \mathbf{U}_{\mathrm{s}_n} \end{pmatrix} \tag{3.19}$$

and transform the matrices $\mathbf{X}_{\mathrm{sub}}$

$$\tilde{\mathbf{X}} = \mathbf{U}^\dagger \mathbf{X}_{\mathrm{sub}} \mathbf{U}, \tag{3.20}$$

where the submatrices $\tilde{\mathbf{X}}_{\mathrm{s}_i\mathrm{s}_i}$ are diagonal and the submatrices $\tilde{\mathbf{X}}_{\mathrm{s}_i\mathrm{s}_j}$ are of the form

$$\tilde{\mathbf{X}}_{\mathrm{s}_i\mathrm{s}_j} = \mathbf{U}^\dagger_{\mathrm{s}_i} \mathbf{X}_{\mathrm{s}_i\mathrm{s}_j} \mathbf{U}_{\mathrm{s}_j}. \tag{3.21}$$

We keep only the subspace of these new orbitals containing the energetically relevant orbitals. In our case the energetically relevant orbitals are the ones with an energy close to the Fermi level. This is done by a $n_{\mathrm{sub}} \times n_{\mathrm{rel}}$ matrix $\tilde{\mathbf{P}}$, where n_{rel} is the number of relevant orbitals. Similarly to the matrix $\mathbf{P}$, the only non-zero elements are

$$\tilde{\mathbf{P}}_{ik'_j} = \begin{cases} \delta_{ik_j} & \text{if the } k_j\text{th orbital is energetically relevant} \\ 0 & \text{otherwise} \end{cases}, \tag{3.22}$$

where k'_j is the index of the new orbitals in the subspace of the energetically relevant orbitals. The transformations up to now can be summarized by

$$\boxed{\mathbf{X}' = \mathbf{Q}^\dagger \mathbf{X} \mathbf{Q}}, \tag{3.23}$$

where

$$\boxed{\mathbf{Q} = \mathbf{P}\mathbf{U}\tilde{\mathbf{P}}}. \tag{3.24}$$

3. In general the orbitals resulting from this transformation won't be orthonormal and therefore have to be treated properly. We will do so by transforming the Hamiltonian matrix and overlap matrix using the Löwdin orthogonalization (2.18)

$$\mathbf{S}'^{-\frac{1}{2}} \mathbf{H}' \mathbf{S}'^{-\frac{1}{2}} \vec{c} = E \vec{c}\,. \tag{3.25}$$

3.2.2.4 Approximations of the various models

We will examine models with different degrees of approximations. We give here an overview of the different models. We give more details on how we calculate the matrix Green's function of the central region and the transmission within these models in appendix A.

Tight Coupling (TC)

In this model the electrode Green's functions are treated at the same footing as in the first-principles calculations, but we couple each electrode to a single site. We do so by setting matrix elements of the matrices $\mathbf{V}_{\mathrm{BDT,C_j}}$ and $\mathbf{V}_{\mathrm{C_j,BDT}}$ in Eq. (3.1) to zero, which do not correspond to hopping between the electrodes and the sulfur atoms. We do the same for the overlap matrices $\mathbf{s}_{\mathrm{BDT,C_j}}$ and $\mathbf{s}_{\mathrm{C_j,BDT}}$.

Tight Coupling + π-electron approximation (TC_π)

Additionally to the approximations from the TC model, we split the transport system into two channels: the p-channel contains all the basis functions from the first-principles calculations describing the $\mathrm{p_z}$ orbitals of the carbon and sulfur atoms, while the r-channel contains all the basis functions describing the remaining orbitals of the carbon, sulfur and hydrogen atoms. We decouple the p-channel and r-channel by setting the matrix elements of the Hamiltonian matrix $\mathbf{H}_{\mathrm{BDT}}$, and also of the overlap matrix $\mathbf{S}_{\mathrm{BDT}}$, corresponding to hopping processes between the two channels to zero. From this point on, we consider only the p-channel.

Tight Coupling + π-electron approximation + effective single orbital ($\mathrm{TC}_\pi^{\mathrm{SO}}$)

From here on we model the electrodes as described in Sec. 3.2.2.2. Furthermore, we reduce the Hamiltonian matrices from the first-principles calculations to model Hamiltonian matrices according to Sec. 3.2.2.3. The subspace contains only the basis functions describing the $\mathrm{p_z}$ orbitals of the carbon and sulfur atoms. The subspace of the new orbitals contains at each site only the orbital closest to the Fermi energy. By doing so we get the model Hamiltonian matrix $\tilde{\mathbf{H}}_{\mathrm{TC}_\pi^{\mathrm{SO}}}$.

Tight-binding (TB)

We reduce the $\mathrm{TC}_\pi^{\mathrm{SO}}$ model to a tight-binding one by setting all hopping elements of $\tilde{\mathbf{H}}_{\mathrm{TC}_\pi^{\mathrm{SO}}}$ to zero, which correspond to hopping processes other than to nearest-neighboring sites.

Hückel

We do not describe the BDT by a Hückel model but only the benzene ring. The model will therefore contain four parameters instead of two: the average of the onsite energies of the sulfur atoms ε_{S}, the average of the onsite energies of the carbon atoms ε_{C}, the average of the hopping parameters describing hopping between nearest-neighboring carbon atoms t_{C} and the average of the hopping parameters describing hopping between nearest-neighboring carbon and sulfur atoms t_{SC}.

Chapter 4

Application and Results

In this chapter we apply the theoretical and computational methods discussed in chapters 2 and 3 to analyze DQI in benzene and benzenedithiolate (BDT) in and out of equilibrium. We label the carbon sites in this chapter according to Fig. 2.6 and the sulfur sites in the following way: The sulfur at site 0 is the nearest-neighbor of the carbon at site 1, while the sulfur at site 7 is the nearest-neighbor of the carbon at site 3 in the case of benzene-1,3-dithiolate or site 4 in the case of benzene-1,4-dithiolate. We label different configurations of BDT as follows: *meta-BDT* in the case of benzene-1,3-dithiolate and *para-BDT* in the case of benzene-1,4-dithiolate. Consequently, we label benzene coupled at sites 1 and 3 *meta-benzene* and benzene coupled at sites 1 and 4 *para-benzene*. In the case of contacting the molecule to electrodes, we add the suffix *+planar* for planar electrodes and *+pointed* for pointed electrodes. Thus, we write the four systems in Fig. 1.3 as: meta-BDT+planar, meta-BDT+pointed, para-BDT+planar and para-BDT+pointed.

We discuss model systems parametrized from literature in Sec. 4.1. In Sec. 4.2 we apply DFT for relaxing the geometry of meta-BDT+planar, meta-BDT+pointed, para-BDT+planar and para-BDT+pointed and calculate the transmission and PDOS of these systems in equilibrium. We map the results obtained from the first-principles calculations onto models with different levels of approximation in Sec. 4.3. The systems are driven out of equilibrium by a bias voltage in Sec. 4.4. In Sec. 4.5 we map the results of the DFT calculations in non-equilibrium onto the same models as in equilibrium and we discuss the influence of the bias voltage on the DQI.

4.1 Hückel model parametrized from literature

In this section, we study benzene and BDT within the Hückel approximation using parameters from literature. While in Sec. 4.1.1 we consider the pristine benzene and BDT molecule, Sec. 4.1.2 discusses transport properties including the electrodes.

The Hückel Hamiltonian (2.14) considers a single onsite energy and a single hopping parameter. While the assumption of a single onsite energy and a single hopping parameter is reasonable for hydrocarbons like benzene, it is less so for derivatives of hydrocarbons like BDT. Neither the hopping parameters nor the onsite energies of the different atom sorts will have the same value. Additionally, we expect the sulfur atoms to influence the nearest-neighboring carbon atoms. Nevertheless, we will treat the benzene ring in the following calculations within a Hückel approach, allowing some insight in the underlying physics. The influence of the sulfur atoms on the benzene ring will be considered later on.

We describe the Hamiltonian of BDT by the matrix

$$\mathbf{H}^{\mathrm{BDT,pm}}_{\mathrm{Hückel}} = \begin{pmatrix} \varepsilon_{\mathrm{S}} & t_{\mathrm{SC}} & 0 & 0 & 0 & 0 & 0 & 0 \\ t_{\mathrm{SC}} & \varepsilon_{\mathrm{C}} & t_{\mathrm{C}} & 0 & 0 & 0 & t_{\mathrm{C}} & 0 \\ 0 & t_{\mathrm{C}} & \varepsilon_{\mathrm{C}} & t_{\mathrm{C}} & 0 & 0 & 0 & 0 \\ 0 & 0 & t_{\mathrm{C}} & \varepsilon_{\mathrm{C}} & t_{\mathrm{C}} & 0 & 0 & t_{\mathrm{SC}} \cdot \mathrm{pm} \\ 0 & 0 & 0 & t_{\mathrm{C}} & \varepsilon_{\mathrm{C}} & t_{\mathrm{C}} & 0 & t_{\mathrm{SC}} \cdot (1-\mathrm{pm}) \\ 0 & 0 & 0 & 0 & t_{\mathrm{C}} & \varepsilon_{\mathrm{C}} & t_{\mathrm{C}} & 0 \\ 0 & t_{\mathrm{C}} & 0 & 0 & 0 & t_{\mathrm{C}} & \varepsilon_{\mathrm{C}} & 0 \\ 0 & 0 & 0 & t_{\mathrm{SC}} \cdot \mathrm{pm} & t_{\mathrm{SC}} \cdot (1-\mathrm{pm}) & 0 & 0 & \varepsilon_{\mathrm{S}} \end{pmatrix} \tag{4.1}$$

with

$$\mathrm{pm} = \begin{cases} 1 & \text{if meta-BDT} \\ 0 & \text{if para-BDT} \end{cases} , \tag{4.2}$$

where the gray-marked submatrix is the Hamiltonian matrix $\mathbf{H}^{\mathrm{B}}_{\mathrm{Hückel}}$ describing the benzene ring. The parameters ε_{C} and ε_{S} are the onsite energies of the carbon and sulfur atoms, while the t_{C} and t_{SC} are the hopping parameters between neighboring carbon atoms and between carbon and sulfur atoms, respectively. We use the following parameters from literature (see appendix B)

$$\begin{aligned} \varepsilon_{\mathrm{C}} &= 0 \text{ eV} \\ \varepsilon_{\mathrm{S}} &= -1.30 \text{ eV} \\ t_{\mathrm{C}} &= -2.60 \text{ eV} \\ t_{\mathrm{SC}} &= -0.87 \text{ eV} \ . \end{aligned} \tag{4.3}$$

4.1.1 Pristine molecules

We start by examining pristine benzene. In the Hückel approximation the orbitals are assumed to be orthonormal and the eigenvalue problem becomes

$$\mathbf{H}^{\mathrm{B}}_{\mathrm{Hückel}} \vec{c}_{\mathrm{B}} = E^{B} \vec{c}_{\mathrm{B}} \ , \tag{4.4}$$

where $\vec{c}_{\mathrm{B}}$ is the eigenvector containing the coefficients of the basis functions and E^{B} is the corresponding eigenenergy. We calculate the matrix Green's functions from

$$\mathbf{g}^{\mathrm{B}}(E) = \left[E^{+}\mathbf{I} - \mathbf{H}^{\mathrm{B}}_{\mathrm{Hückel}}\right]^{-1} \ . \tag{4.5}$$

Solving Eq. (4.4) we get the following eigenenergies for the benzene ring

$$E^{\mathrm{B}} = \{-5.2, -2.6, -2.6, +2.6, +2.6, +5.2\} \ . \tag{4.6}$$

According to Eq. (2.137) the transmission is proportional to the square of the absolute value of the Green's function $g^{\mathrm{B}}_{lr}(E)$, with $l = 1$ and $r = 4 -$ pm in the case of benzene and $l = 0$ and $r = 7$ in the case of BDT. We set $0^+ = 0.25$ in the Green's function, to see how a non-negligible imaginary part, e.g. due to the molecule lying on a substrate, influences the DQI. We calculate the matrix Green's function using Eq. (4.5) and plot the results in Fig. 4.1.

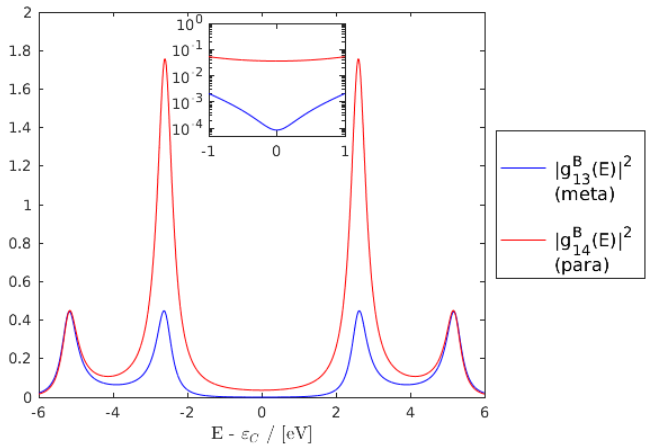

Fig. 4.1. Square of the absolute value of the Green's functions $g^{\mathrm{B}}_{13}(E)$ (meta) and $g^{\mathrm{B}}_{14}(E)$ (para). Peak broadening is due to $0^+ = 0.25$. While the meta configuration shows DQI at $E = \varepsilon_{\mathrm{C}}$, the para configuration has a finite transmission. The GAOS predicts DQI for meta-benzene and para-benzene at $E = \varepsilon_{\mathrm{C}} \pm t_{\mathrm{C}}$, which does not occur.

Strictly speaking, Fig. 4.1 shows that $\left|g^{\mathrm{B}}_{13}(E)\right|^2$ is several orders of magnitude smaller than $\left|g^{\mathrm{B}}_{14}(E)\right|^2$ around the energy $E = \varepsilon_{\mathrm{C}}$ but in the case of a non-negligible 0^+ exact DQI is no longer observed.

We know from Sec. 2.6.3, that the GAOS predicts DQI at $E = \{\varepsilon_{\mathrm{C}} - t_{\mathrm{C}}, \varepsilon_{\mathrm{C}}, \varepsilon_{\mathrm{C}} + t_{\mathrm{C}}\}$ in the case of meta-benzene and at $E = \{\varepsilon_{\mathrm{C}} - t_{\mathrm{C}}, \varepsilon_{\mathrm{C}} + t_{\mathrm{C}}\}$ in the case of para-benzene. We observe in Fig. 4.1 DQI at $E = \varepsilon_{\mathrm{C}}$ in the case of meta-benzene, but we observe neither for meta-benzene nor for para-benzene DQI at $E = \varepsilon_{\mathrm{C}} \pm t_{\mathrm{C}}$. Therefore, we calculate the Green's functions of the benzene from Eq. (2.142). We have calculated the numerator of Eq. (2.142) in the case of meta-benzene and para-benzene in Eqs. (2.149) and (2.150). For the denominator we get

$$\det\left((E + i0^+)\mathbf{I} - \mathbf{H}^{\mathrm{B}}_{\mathrm{Hückel}}\right) = (E - \varepsilon_{\mathrm{C}} + i0^+)^6 - 6(E - \varepsilon_{\mathrm{C}} + i0^+)^4 t_{\mathrm{C}}^2 + 9(E - \varepsilon_{\mathrm{C}} + i0^+)^2 t_{\mathrm{C}}^4 - 4t_{\mathrm{C}}^6 \,. \tag{4.7}$$

Now we set $0^+ \to 0$ and calculate $g^{\mathrm{B}}_{13}(\varepsilon_{\mathrm{C}} \pm t_{\mathrm{C}})$ and $g^{\mathrm{B}}_{14}(\varepsilon_{\mathrm{C}} \pm t_{\mathrm{C}})$. By doing so we get indeterminate expressions, which we have to evaluate using L'Hospital's rule

$$g^{\mathrm{B}}_{13}(\varepsilon_{\mathrm{C}} \pm t_{\mathrm{C}}) = \lim_{E \to \varepsilon_{\mathrm{C}} \pm t_{\mathrm{C}}} \frac{t_{\mathrm{C}}^2 (E - \varepsilon_{\mathrm{C}})^3 - t_{\mathrm{C}}^4 (E - \varepsilon_{\mathrm{C}})}{(E - \varepsilon_{\mathrm{C}})^6 - 6(E - \varepsilon_{\mathrm{C}})^4 t_{\mathrm{C}}^2 + 9(E - \varepsilon_{\mathrm{C}})^2 t_{\mathrm{C}}^4 - 4t_{\mathrm{C}}^6} = \frac{2t_{\mathrm{C}}^4}{0} \tag{4.8}$$

$$g^{\mathrm{B}}_{14}(\varepsilon_{\mathrm{C}} \pm t_{\mathrm{C}}) = \lim_{E \to \varepsilon_{\mathrm{C}} \pm t_{\mathrm{C}}} \frac{2t_{\mathrm{C}}^3 (E - \varepsilon_{\mathrm{C}})^2 - 2t_{\mathrm{C}}^5}{(E - \varepsilon_{\mathrm{C}})^6 - 6(E - \varepsilon_{\mathrm{C}})^4 t_{\mathrm{C}}^2 + 9(E - \varepsilon_{\mathrm{C}})^2 t_{\mathrm{C}}^4 - 4t_{\mathrm{C}}^6} = \frac{4t_{\mathrm{C}}^4}{0} \,. \tag{4.9}$$

We see that the Green's functions $g^{\mathrm{B}}_{13}(E)$ and $g^{\mathrm{B}}_{14}(E)$ diverge at $E - \varepsilon_{\mathrm{C}} = \pm t_{\mathrm{C}}$. The reason we do neither observe the divergence of the Green's functions at $E = \varepsilon_{\mathrm{C}} \pm t_{\mathrm{C}}$ nor exact DQI at $E = \varepsilon_{\mathrm{C}}$ in Fig. 4.1 is the peak broadening due to 0^+.

Now we study pristine BDT. We take the Hamiltonian matrix $\mathbf{H}_{\text{Hückel}}^{\text{BDT,pm}}$ and solve the equations

$$\mathbf{H}_{\text{Hückel}}^{\text{BDT,pm}} \vec{c}_{\text{BDT}} = E_{\text{pm}}^{\text{BDT}} \vec{c}_{\text{BDT}} \tag{4.10}$$

$$\mathbf{g}^{\text{BDT,pm}}(E) = \left[E^{+}\mathbf{I} - \mathbf{H}_{\text{Hückel}}^{\text{BDT,pm}}\right]^{-1} . \tag{4.11}$$

We solve Eq. (4.10) once for meta-BDT and once for para-BDT and get the eigenenergies

$$E_{\text{Meta}}^{\text{BDT}} = \{-5.3, -2.9, -2.7, -1.2, -1.1, +2.6, +2.7, +5.2\} \tag{4.12}$$

$$E_{\text{Para}}^{\text{BDT}} = \{-5.3, -2.9, -2.6, -1.4, -1.0, +2.6, +2.7, +5.2\} . \tag{4.13}$$

Now we calculate $\left|g_{07}^{\text{BDT,pm}}(E)\right|^2$ for meta-BDT and for para-BDT. Fig. 4.2 shows the results. We see that only two eigenstates are close to 0 and therefore contribute to the transmission. The contribution from the remaining eigenstates to the transmission is negligible.

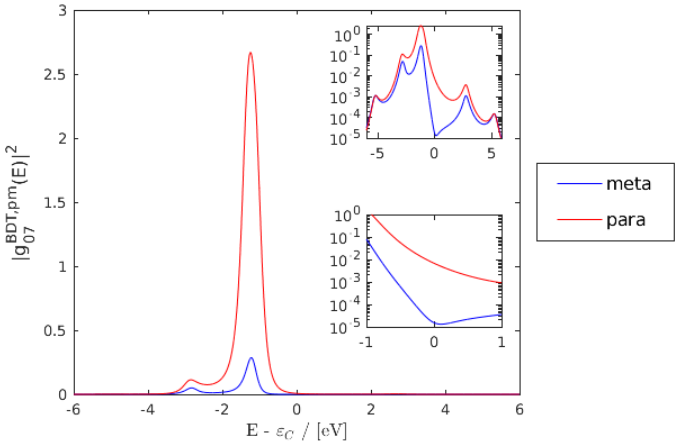

Fig. 4.2. Square of the absolute value of the Green's function $g_{07}^{\text{BDT,pm}}(E)$ of meta-BDT and para-BDT. Peak broadening is due to $0^+ = 0.25$. We see that only the eigenstates close to 0 contribute to the transmission, while the contribution of the remaining eigenstates to the transmission is negligible. We also see that due to 0^+ the transmission minimum is shifted towards higher energies.

Like in the case of the benzene molecule, Fig. 4.2 shows that $\left|g_{07}^{\text{BDT,pm}}(E)\right|^2$ is several orders of magnitude smaller around the energy $E = \varepsilon_{\text{C}}$ in the case of meta-BDT than in the case of para-BDT, but no exact DQI is observed for meta-BDT. Additionally, we observe that in the case of meta-BDT the minimum of $\left|g_{07}^{\text{BDT,pm}}(E)\right|^2$ shifts towards higher energies (see inset).

4.1.2 Transport systems

In this section we include the electrodes. We model the electrodes within the wide band limit and we assume that each electrode couples to a single site (see Sec. 2.6.1). The matrix elements of the hybridization matrix are zero except for $(\mathbf{\Sigma}_{\text{L}}^{\text{pm}})_{ll}$ and $(\mathbf{\Sigma}_{\text{R}}^{\text{pm}})_{rr}$, which we set to be

$$(\mathbf{\Sigma}_{\text{L}}^{\text{pm}})_{ll} = (\mathbf{\Sigma}_{\text{R}}^{\text{pm}})_{rr} = -0.5\text{i} . \tag{4.14}$$

We calculate the level-width functions according to Eq. (2.113). By doing so, Eq. (2.137) becomes

$$T(E) = \left|G_{\mathrm{lr}}(E)\right|^2 . \tag{4.15}$$

Additionally, we reduce the artificial broadening to $0^+ = 2.5 \cdot 10^{-3}$ for the following calculations.

Like in the case of the pristine molecules, we start with the benzene molecule. We calculate the Green's functions $G^{\mathrm{B}}_{13}(E)$ and $G^{\mathrm{B}}_{14}(E)$ from

$$\mathbf{G}^{\mathrm{B,pm}}(E) = \left[E^+\mathbf{I} - \mathbf{H}^{\mathrm{B}}_{\mathrm{Hückel}} - \mathbf{\Sigma}^{\mathrm{pm}}_{\mathrm{L}} - \mathbf{\Sigma}^{\mathrm{pm}}_{\mathrm{R}}\right]^{-1} . \tag{4.16}$$

We calculate the transmission once from $G^{\mathrm{B,pm}}_{13}(E)$ and once from $G^{\mathrm{B,pm}}_{14}(E)$ and plot the results in Fig. 4.3. In the case of meta-benzene DQI occurs now also at $E = \varepsilon_{\mathrm{C}} \pm t_{\mathrm{C}}$, while in the case of para-BDT it does not.

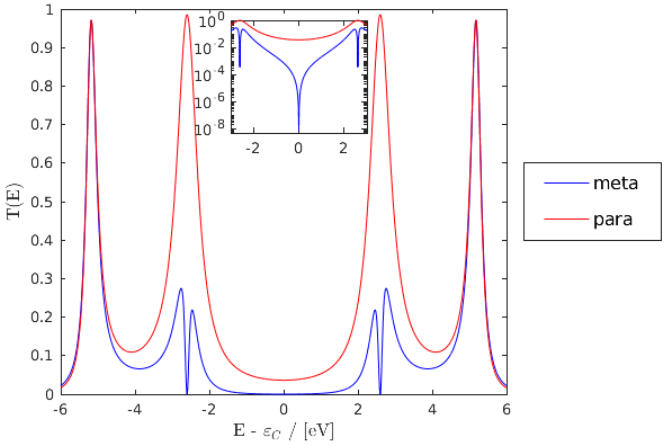

Fig. 4.3. Transmission of meta-benzene and para-benzene including electrodes. We see that by coupling electrodes in meta-position DQI occurs now at $E = \varepsilon_{\mathrm{C}}$ and $E = \varepsilon_{\mathrm{C}} \pm t_{\mathrm{C}}$, while in the case of coupling electrodes in para-position no DQI occurs.

We calculate the denominator of Eq. (2.142) once more for the meta-benzene and once for the para-benzene. We set again $0^+ \to 0$ and write $(E - \varepsilon_{\mathrm{C}}) = E'$. We get

$$\begin{aligned}
&\det\left(E\mathbf{I} - H^{\mathrm{B}}_{\mathrm{Hückel}} - \mathbf{\Sigma}^1_{\mathrm{L}} - \mathbf{\Sigma}^1_{\mathrm{R}}\right) \\
&\quad = E'^6 + iE'^5 - 6E'^4 t_{\mathrm{C}}^2 - \frac{E'^4}{4} - 4iE'^3 t_{\mathrm{C}}^2 + 9E'^2 t_{\mathrm{C}}^4 + \frac{E'^2 t_{\mathrm{C}}^2}{2} + 3iE' t_{\mathrm{C}}^4 - 4t_{\mathrm{C}}^6 \qquad (4.17) \\
&\det\left(E\mathbf{I} - H^{\mathrm{B}}_{\mathrm{Hückel}} - \mathbf{\Sigma}^0_{\mathrm{L}} - \mathbf{\Sigma}^0_{\mathrm{R}}\right) \\
&\quad = E'^6 + iE'^5 - 6E'^4 t_{\mathrm{C}}^2 - \frac{E'^4}{4} - 4iE'^3 t_{\mathrm{C}}^2 + 9E'^2 t_{\mathrm{C}}^4 + \frac{E'^2 t_{\mathrm{C}}^2}{2} + 3iE' t_{\mathrm{C}}^4 - 4t_{\mathrm{C}}^6 - \frac{t_{\mathrm{C}}^4}{4} , \qquad (4.18)
\end{aligned}$$

where we described the matrix elements of the hybridization matrices using Eq. (4.14). Eq. (4.17) does not vanish for $E = \varepsilon_{\mathrm{C}} \pm t_{\mathrm{C}}$ and, in further consequence, we observe in the case of meta-benzene DQI also at $E = \varepsilon_{\mathrm{C}} \pm t_{\mathrm{C}}$. Eq. (4.18) vanishes at $E = \varepsilon_{\mathrm{C}} \pm t_{\mathrm{C}}$ and we have to evaluate the Green's function of the para-benzene using L'Hospital's rule. By doing so we get $G^{\mathrm{B},0}_{14}(\varepsilon_{\mathrm{C}} \pm t_{\mathrm{C}}) = \mp i$. Calculating the transmission from this result gives a transmission of 1 at $E = \varepsilon_{\mathrm{C}} \pm t_{\mathrm{C}}$, while the transmission in Fig. 4.3 is slightly lower than 1. This discrepancy results from Eqs. (4.17) and (4.18) not including the infinitesimal 0^+.

Now we calculate the PDOS of meta-benzene and para-benzene using Eq. (2.127). We are interested only in the DOS of the scattering states and therefore

$$\mathrm{DOS}_{\mathrm{scat}}(E) = A_{\mathrm{L}}(E) + A_{\mathrm{R}}(E)\ . \tag{4.19}$$

We are also interested in the $\mathrm{PDOS}_{\mathrm{scat}}(E, j)$ of each individual carbon atom. We calculate

$$\mathrm{PDOS}_{\mathrm{scat}}(E, j) = \frac{i}{2\pi}\left(\mathbf{G}_{\mathrm{C}}\left(\mathbf{\Sigma}_{\mathrm{L}} - \mathbf{\Sigma}_{\mathrm{L}}^{\dagger}\right)\mathbf{G}_{\mathrm{C}}^{\dagger}\right)_{jj} + \frac{i}{2\pi}\left(\mathbf{G}_{\mathrm{C}}\left(\mathbf{\Sigma}_{\mathrm{R}} - \mathbf{\Sigma}_{\mathrm{R}}^{\dagger}\right)\mathbf{G}_{\mathrm{C}}^{\dagger}\right)_{jj} \tag{4.20}$$

with

$$\mathrm{DOS}_{\mathrm{scat}}(E) = \sum_{j} \mathrm{PDOS}_{\mathrm{scat}}(E, j)\ , \tag{4.21}$$

where j labels the site of the carbon atom. We calculate $\mathrm{PDOS}_{\mathrm{scat}}(E, j)$ for each carbon atom and plot the results in Fig 4.4. We take advantage of the symmetry of benzene and plot only the $\mathrm{PDOS}_{\mathrm{scat}}$ of topologically different sites. We see from Fig. 2.6 that in the case of para-benzene the sites 1 and 4 are identical. Also sites 2, 3, 5 and 6 are identical. For meta-benzene sites 1 and 3 are identical and also sites 4 and 6.

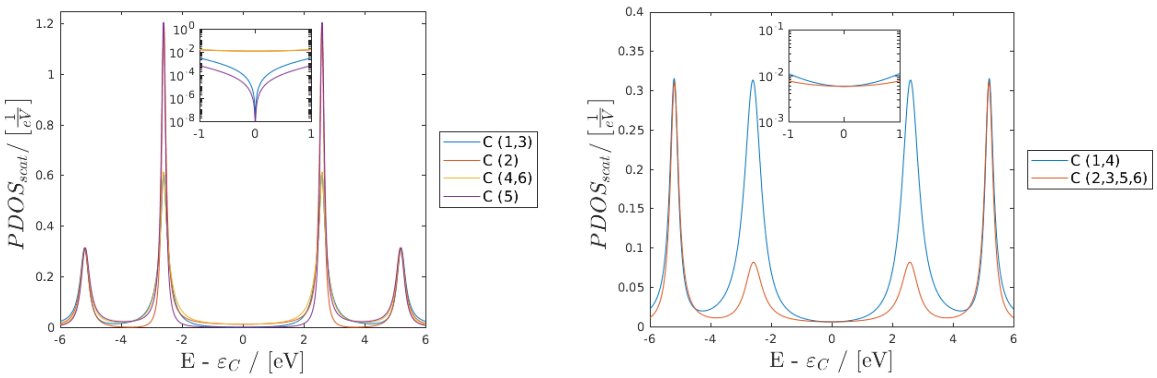

Fig. 4.4. Scattering PDOS of the benzene molecule at the different carbon sites in the case of meta-benzene (left) and para-benzene (right). We calculated the scattering PDOS from Eq. (4.20). The numbers in the curved brackets label the sites of the carbon atoms according to Fig. 2.6. We see that in the case of meta-benzene the sites contacted to the electrodes have no states at the Fermi energy.

Fig. 4.4 shows that in the case of meta-benzene the number of scattering states vanishes at sites 1, 3 and 5 for an energy of $E = \varepsilon_{\mathrm{C}}$, while para-benzene has states at each carbon site.

For our purpose it is more advantageous to consider the PDOS not just energy-resolved, like we do in Fig. 4.4, but to consider also the number of states within an energy interval. Therefore we calculate

$$\Big(\text{Integrated PDOS}\Big)_j = \int_{\mathrm{E_{min}}}^{\mathrm{E_{max}}} \mathrm{PDOS}_{\mathrm{scat}}(E, j)dE\ . \tag{4.22}$$

Fig. 4.5 shows the integrated PDOS of the benzene ring with $E_{\mathrm{min}} = -0.5\,\mathrm{eV}$ and $E_{\mathrm{max}} = 0.5\,\mathrm{eV}$. Meta-benzene has almost no scattering states in the energy range $-0.5\,\mathrm{eV}$ to $0.5\,\mathrm{eV}$ at the sites contacted to the electrodes, while para-benzene has states at these sites.

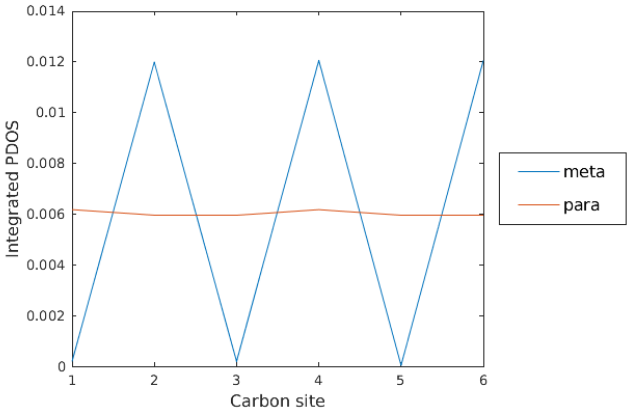

Fig. 4.5. Integrated PDOS of benzene. We integrate the scattering PDOS of the individual carbon atoms numerically over the interval $[-0.5, +0.5]$ eV with an energy resolution of 0.005 eV using the trapezoidal rule. The sites are labeled according to Fig. 2.6. Meta-benzene has almost no states at the sites contacted to the electrodes, while para-benzene has states at the sites contacted to the electrodes.

We consider now meta-BDT and para-BDT. We calculate the matrix Green's function from

$$\mathbf{G}^{\mathrm{BDT,pm}}(E) = \left[E^{+}\mathbf{I} - \mathbf{H}^{\mathrm{BDT,pm}}_{\mathrm{Hückel}} - \mathbf{\Sigma}^{\mathrm{pm}}_{\mathrm{L}} - \mathbf{\Sigma}^{\mathrm{pm}}_{\mathrm{R}}\right]^{-1}, \tag{4.23}$$

We calculate $\mathbf{G}^{\mathrm{BDT,pm}}_{07}(E)$ and the transmission once for meta-BDT and once for para-BDT. Fig. 4.6 shows the resulting transmission.

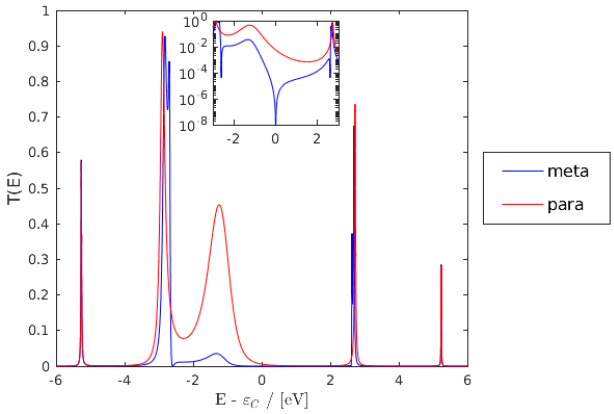

Fig. 4.6. Transmission of meta-BDT and para-BDT including electrodes. Like in the case of meta-benzene and para-benzene, meta-BDT displays DQI at $E = \varepsilon_{\mathrm{C}} \pm t_{\mathrm{C}}$, while para-BDT does not. In contrast to the pristine BDT, all eigenstates contribute to the transmission.

We see in Fig. 4.6 that, similarly to meta-benzene and para-benzene, meta-BDT displays DQI at $E = \varepsilon_{\mathrm{C}} \pm t_{\mathrm{C}}$, while para-BDT does not. Additionally, we observe that unlike in the case of pristine BDT not only the eigenstates close to 0 but all eigenstates contribute to the transmission. In contrast to pristine BDT, the eigenstates close to 0 are additionally broadened by the electrodes, while the remaining eigenstates are not. In consequence, the eigenstates closer to 0 are stronger broadened than the remaining ones. This results in the amplitude of the transmission peaks of all eigenstates being of about the same order.

Now we calculate $\mathrm{PDOS}_{\mathrm{scat}}(E, j)$ for BDT. Fig. 4.7 shows the resulting curves. Like in the case of benzene the carbon atoms at sites 1, 3 and 5 have a small number of states around the energy $E - \varepsilon_{\mathrm{C}} = 0$. By comparing Figs. 4.6 and 4.7 we see that DQI occurs at energies at which either the sulfur atoms or the carbon atoms at sites 1 and 3 have no states.

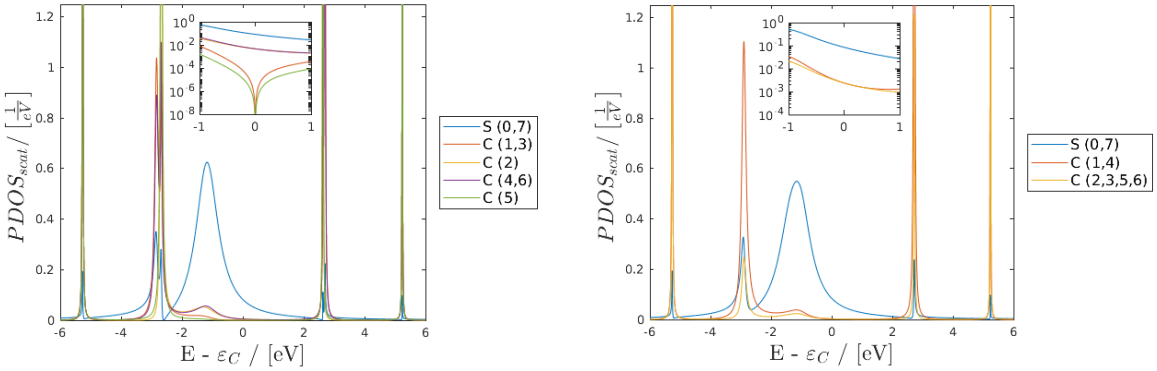

Fig. 4.7. Scattering PDOS of BDT at the different sites in the case of meta-BDT (left) and para-BDT (right). We calculated the scattering PDOS from Eq. (4.20). The numbers $1 - 6$ in the curved brackets label the sites of the carbon atoms according to Fig. 2.6. The sulfur at site 0 is the nearest-neighbor of the carbon at site 1 and the sulfur at site 7 is the nearest-neighbor of the carbon at site 3 or 4 depending on whether meta- or para-BDT is considered. By comparing the scattering PDOS to Fig. 4.6 we see that for transmission the carbon atoms at sites 1 and 3 and the sulfur atoms have to provide states.

4.2 DFT calculations in equilibrium

4.2.1 Settings for the DFT calculations and geometry relaxation

We construct the systems (see Fig. 1.3) based on the results from Ref. [28], where the authors calculated the transmission of systems similar to the para-BDT+planar system. We choose the electrodes to be Au(111) with a lattice constant of 4.175 Å. We set the distance between the surfaces of the two electrodes of the para-BDT+planar system to be 9.680 Å. TranSIESTA calculations require periodicity perpendicular to the transport direction. Therefore we increase the size of the electrodes in these directions to prevent BDT-BDT interactions. According to the results from Ref. [28], the transmission of an Au(111)-BDT-Au(111) system containing 5×5 gold atoms in the electrode layers perpendicular to the transport direction can be considered converged, and in consequence the BDT-BDT interactions are negligible. To keep the coupling of the BDT towards the electrodes as constant as possible, we relax the geometry of the para-BDT+planar system and set the distance between the sulfur atoms and the electrodes of the four systems to be about equally large. The resulting electrode-electrode distances of the systems are summarized in Tab. 4.1. Afterwards we relax the geometry of the remaining three systems. We fix the position of the gold atoms in the four systems and relax only the geometry of the BDT molecules. It shows that the reduction of the number of k-points within the supercell to $1 \times 1 \times 1$ (the first two being the number of k-points in the direction perpendicular and the last one in the direction parallel to the transport direction) during geometry optimization does influence the results only marginally and therefore we relax the BDT molecules by Γ-point-only calculations to reduce the computational cost. We choose the exchange-correlation functional to be a PBE functional during all the DFT calculations. The pseudopotentials used in these calculations are the ones from Ref. [29]. The pseudopotentials for the carbon, hydrogen and sulfur atoms are non-relativistic ones, while the one used for gold is a relativistic one. A complete list of the used options and parameters is found in appendix C.

Tab. 4.1. Distances between the electrodes in the four different systems in units of Angstrom. In the case of pointed electrodes the tip-tip distance is given.

Electrode / Configuration	Para	Meta
Planar	9.680	9.280
Pointed	10.807	10.313

4.2.2 Transmission and DOS

Now we increase the number of k-points within the supercell from $1 \times 1 \times 1$ to $4 \times 4 \times 1$ and calculate the Hamiltonian matrices and overlap matrices of the transport systems using TRANSIESTA (see Sec. 3.1.2). In the end we calculate the transmission and the PDOS of the transport systems using TBTRANS (see Sec. 3.2.1). We choose the limits of the energy grid for the TBTRANS calculations to be $-6\,\mathrm{eV}$ to $6\,\mathrm{eV}$ and the resolution to be $0.05\,\mathrm{eV}$. Fig. 4.8 shows the resulting transmissions and PDOS.

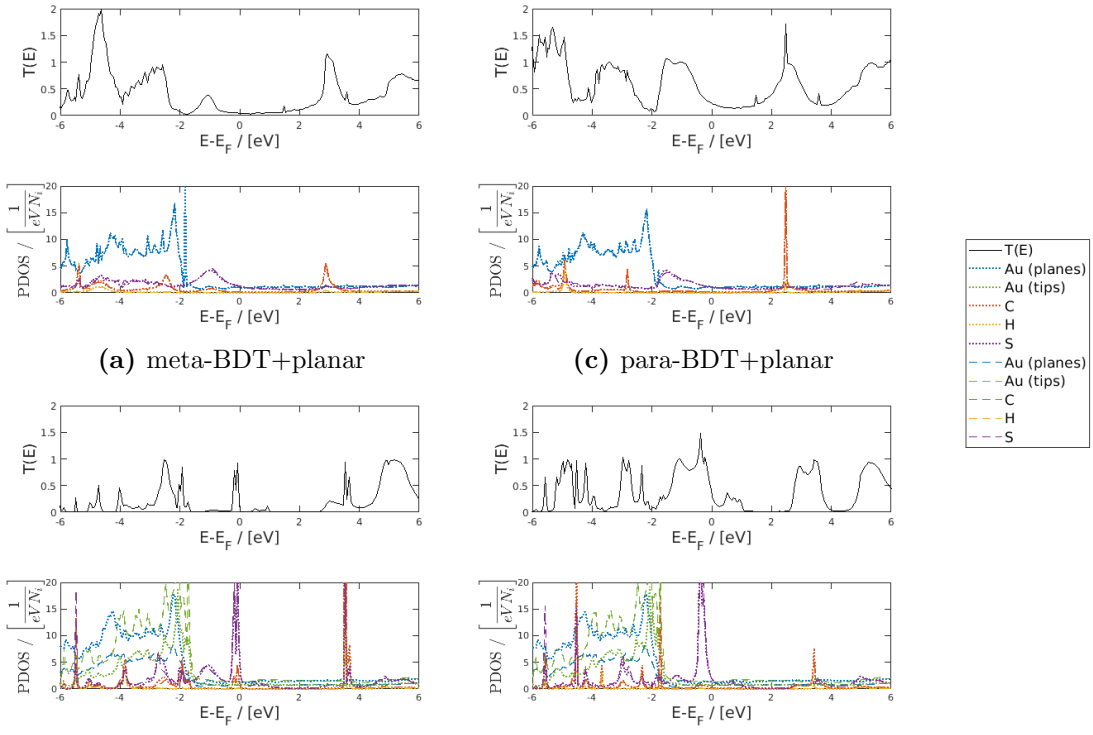

(a) meta-BDT+planar **(c)** para-BDT+planar

(b) meta-BDT+pointed **(d)** para-BDT+pointed

Fig. 4.8. Transmission and PDOS of the left (dotted) and right (dashed) spectral function of the different transport systems in equilibrium. For better comparability the PDOS of each element is divided by the number of atoms of the corresponding element. We see that the meta-BDT systems have a lower transmission around the Fermi energy than the para-BDT systems.

We see in Fig. 4.8 that around the Fermi energy the transmission of the meta-BDT systems is lower than the transmission of the para-BDT systems. The transmission minima around the Fermi energy are summarized in Tab. 4.2. We see from the numerical values that neither the transmission of the meta-BDT+planar system nor of the meta-BDT+pointed system vanishes beyond 0^+: so there is no exact DQI. We also observe that neither of both systems containing meta-BDT display the transmission minimum at the Fermi energy but about $0.2\,\mathrm{eV}$ to $0.4\,\mathrm{eV}$ above it.

Tab. 4.2. Transmission minima around the Fermi energy. Neither does the transmission of the meta-BDT systems vanish nor do the transmission minima occur at the Fermi energy.

	$E - E_\mathrm{F}$ / eV	$T(E - E_\mathrm{F})$
meta-BDT+pointed	0.225	$6.3 \cdot 10^{-3}$
meta-BDT+planar	0.375	$30.8 \cdot 10^{-3}$
para-BDT+pointed	0.275	$107.5 \cdot 10^{-3}$
para-BDT+planar	0.775	$139.1 \cdot 10^{-3}$

4.2.2.1 Contributions of the different transport channels to the transmission

We split the transport system into a p-channel and an r-channel as described in Sec. 3.2.2.4. We give the mathematical details of how we split up the transmission into these contributions in appendix D. We get for the transmission of the DFT calculations

$$\mathrm{T}_\mathrm{DFT}(E) = \mathrm{T}_\mathrm{p}(E) + \mathrm{T}_\mathrm{r}(E) + \mathrm{T}_\mathrm{int}(E)\,, \tag{4.24}$$

where $\mathrm{T}_\mathrm{p}(E)$ and $\mathrm{T}_\mathrm{r}(E)$ are the transmissions of the p-channel and r-channel, respectively. $\mathrm{T}_\mathrm{int}(E)$ is the interference term describing the interaction of the two channels with one another. Fig. 4.9 shows the different contributions from Eq. (4.24) and the total transmission of the BDT+planar systems, while Fig. 4.10 shows the different contributions from Eq. (4.24) and the total transmission of the BDT+pointed systems.

Fig. 4.9 shows that in the case of para-BDT+planar the p-channel makes a major contribution to the total transmission around the Fermi energy, while the r-channel contributes only marginally to the total transmission. The transmission $\mathrm{T}_\mathrm{p}(E)$ through the p-channel of the meta-BDT+planar system is very small around the Fermi energy. In contrast to the model calculations from Sec. 4.1.2 the transmission $\mathrm{T}_\mathrm{p}(E)$ of the meta-BDT+planar system does not vanish. Unlike in the case of para-BDT+planar the transmission through the r-channel of the meta-BDT+planar system is quite low but the r-channel makes major contributions to the total transmission of meta-BDT+planar around the Fermi energy. We see in Fig. 4.9 that the interference term is small throughout most parts of the energy range.

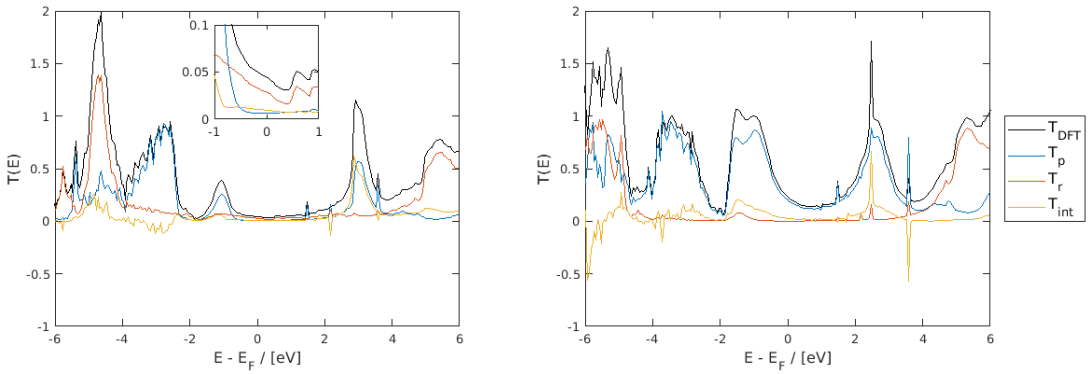

Fig. 4.9. Contributions of the different transport channels to the transmission of meta-BDT+planar (left) and para-BDT+planar (right). The transmission around the Fermi energy of para-BDT+planar is dominated by the p-channel, while the transmission around the Fermi energy of meta-BDT+planar is dominated by the r-channel. Additionally, the p-channel of meta-BDT+planar shows no exact DQI.

Fig. 4.10 shows that, except for the transmission peak right below the Fermi energy, not the p-channel but the r-channel of both the BDT+pointed systems makes major contributions to the transmission around the Fermi energy. This result is in qualitative agreement to the results in Fig. 4.9 in the case of meta-BDT but not so in the case of para-BDT. While the BDT molecules in the remaining systems lie quite well in the xy-plane, the tilt of the BDT in the para-BDT+pointed system with respect to the xy-plane is considerable. We assume therefore that the p-channel of the para-BDT+pointed system does not describe sufficiently well the actual p_z orbitals of the BDT, i.e. the orbitals orthonormal to the benzene ring, and a basis transformation is unavoidable for a sufficiently good description of this system.

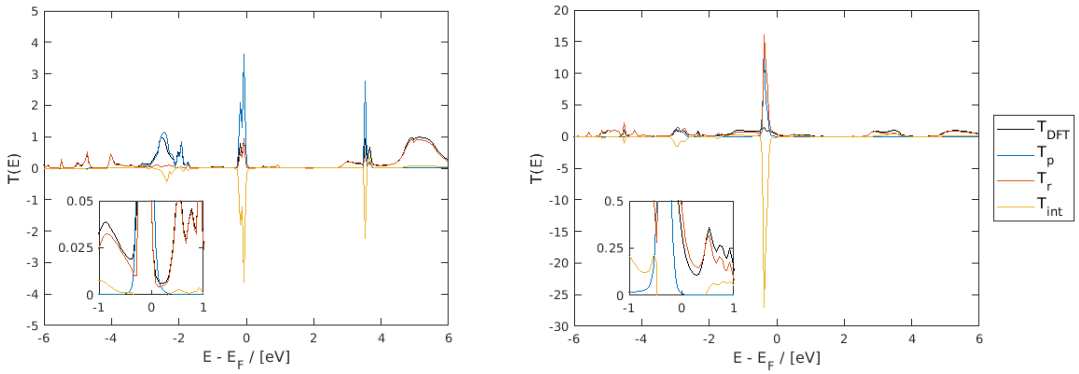

Fig. 4.10. Contributions of the different transport channels to the transmission of meta-BDT+pointed (left) and para-BDT+pointed (right). The transmission around the Fermi energy of both systems is dominated by the r-channel, which is in good agreement with the results from Fig. 4.9 in the case of meta-BDT but not in the case of para-BDT. We assume in the case of para-BDT+pointed that the p_z orbitals of the p-channel do not describe sufficiently well the p_z orbitals of the BDT, requiring a basis transformation (see main text).

4.3 Model calculations in equilibrium

The Hückel calculations in Sec. 4.1.2 show DQI in the case of meta-benzene and meta-BDT, while the first-principles calculations of the meta-BDT+planar system show a small but finite transmission through the p-channel. The difference between the first-principles calculations and the Hückel calculations from Sec. 4.1.2 are the following assumptions:

- Each electrode couples solely to one sulfur atom
- Only p_z orbitals of sulfur and carbon are considered. The remaining orbitals are neglected.
- Hopping processes are limited to nearest neighboring atoms
- The BDT is described only by four parameters: ε_C, ε_S, t_C and t_{SC}

We examine the impact of these assumptions on the first-principles results in more detail. We do so by taking the Hamiltonian matrices and overlap matrices from the first-principles calculations and applying the approximations discussed Sec. 3.2.2.4.

4.3.1 Electrodes

In the first step we analyze the PDOS of the electrodes. Due to the localization of the atomic orbitals the coupling of gold atoms spatially closer to the sulfur atom is more important than the coupling of gold atoms spatially further away. Therefore we examine the PDOS of the nearest-neighbor gold atoms in more detail. The PDOS of the nearest-neighbor gold atoms in the case of planar and pointed electrodes are plotted in Fig. 4.11. We see that the PDOS of the tips of the pointed electrodes have too much structure and cannot be approximated by a simple analytic function. The PDOS for the nearest-neighboring gold atoms of the sulfur atoms in the case of BDT+planar can be approximated very well by the analytic expressions from Eqs. (3.8) and (3.9). Therefore we analyze only the BDT+planar systems within the models.

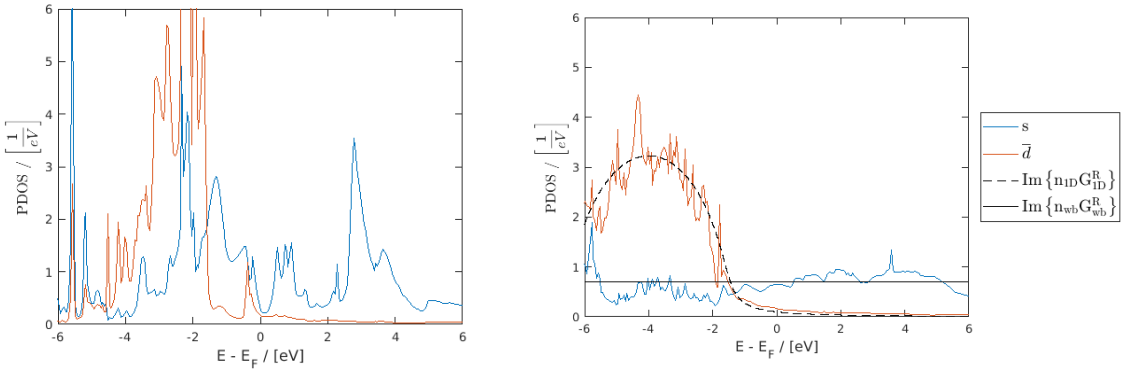

Fig. 4.11. PDOS of the gold atom at the tip of the left pointed electrode (left) and one of the nearest-neighbor gold atoms (see Fig. 1.3) of the left planar electrode (right) of the para-BDT systems. The Green's functions (3.8) and (3.9) model the planar electrodes quite well, while the pointed electrodes have to much structure for being modeled by simple analytic functions. We discuss the scaling factors n_{wb} and $n_{1\mathrm{D}}$ and the Green's functions in more detail in the main text.

We want the model electrodes to have the same DOS as in the first-principles calculations. We know from Sec. 2.4.4 that we can calculate the DOS from the Green's function. Therefore we want the electrode Green's functions (3.8) and (3.9) to fulfill the condition

$$\mathrm{PDOS}^{i}_{\mathrm{Au}}(E) = -\frac{1}{\pi}\mathrm{Im}\Big(n_i G^{\mathrm{R}}_i(E)\Big) \tag{4.25}$$

with $i \in \{1\mathrm{D}, \mathrm{wb}\}$, where n_i takes care of the correct normalization of the Green's functions. n_i and $\mathrm{PDOS}^{\mathrm{wb}}_{\mathrm{Au}}$ are constants with $n_i, \mathrm{PDOS}^{\mathrm{wb}}_{\mathrm{Au}} \in \mathbb{R}$. We determine $\mathrm{PDOS}^{\mathrm{wb}}_{\mathrm{Au}}$ by fitting a constant to the PDOS of the nearest-neighboring gold atoms and choose n_{wb} such that Eq. (4.25) is fulfilled. We find $\mathrm{PDOS}^{\mathrm{wb}}_{\mathrm{Au}} \approx 0.7$. Therefore we choose the bandwidth of the Green's function (3.8) to be 24 eV and rescale it to have an imaginary part of $-0.7\pi\ \frac{1}{\mathrm{eV}}$. In Fig. 4.11 we have chosen the scaling factor $n_{1\mathrm{D}}$ to be 14 and the remaining parameters are

$$\begin{aligned} \varepsilon_0 &= -4.00 \\ \eta &= 0.25 \\ t &= -1.25\,. \end{aligned} \tag{4.26}$$

While these parameters fit $G^{\mathrm{R}}_{1\mathrm{D}}$ well to the mean value of the PDOS of the d orbitals, a smaller value for η leads to better results regarding the transmission and PDOS in the $\mathrm{TC}^{\mathrm{SO}}_{\pi}$, TB and Hückel model. Therefore we use $\eta = 2.5 \cdot 10^{-3}$ and take the remaining parameters of the Green's function $G_{1\mathrm{D}}$ to be the same as the parameters (4.26) in the model calculations.

We model the electrodes according to Sec. 3.2.2.2. Therefore we will not calculate the coupling of the BDT towards the electrodes from the results of the first-principles calculations. We estimate the coupling $t_{\mathrm{S_j s_j}}$ of the $\mathrm{p_z}$ orbitals of the sulfur atoms towards the s orbitals of the electrodes, with $\mathrm{j} \in \{\mathrm{l}, \mathrm{r}\}$ being the site the electrodes couple to and $\mathrm{S_j}$ and $\mathrm{s_j}$ denoting the $\mathrm{p_z}$ orbital of the sulfur atoms and the s orbitals of the electrodes, respectively, in the following way: We take the coupling of the $\mathrm{p_z}$ orbitals of the sulfur atoms and the s orbitals of the electrodes, transform them to match the new orbitals in the model system and project the resulting couplings on the basis function energetically closer to the Fermi energy. Finally, we take into account the Löwdin orthogonalization by normalizing the coupling. This procedure is described by the equation

$$t_{\mathrm{S_j s_j}} = \left(\mathbf{S'}^{-\frac{1}{2}}\right)_{oo} [1, 0]\, \mathbf{U}^{\dagger}_{\mathrm{S_j}} \begin{bmatrix} t^{\zeta_1}_{\mathrm{S_j s_j}} \\ t^{\zeta_2}_{\mathrm{S_j s_j}} \end{bmatrix} . \tag{4.27}$$

$t^{\zeta_1}_{\mathrm{S_j s_j}}$ and $t^{\zeta_2}_{\mathrm{S_j s_j}}$ are the couplings of the first and second basis function describing the $\mathrm{p_z}$ orbital of the sulfur atoms towards the basis function describing the s orbital of the nearest-neighboring gold atom. $\mathbf{U}^{\dagger}_{\mathrm{S_j}}$ is the unitary transformation matrix diagonalizing the Hamiltonian matrix of the sulfur (see Sec. 3.2.2.3). The weighting $\left(\mathbf{S'}^{-\frac{1}{2}}\right)_{oo}$ results from the Löwdin orthogonalization of the orbitals of the model with $\mathbf{S'}$ being the overlap matrix of the model system.

We estimate the coupling of the sulfur atoms and the nearest-neighboring gold atoms according to Eq. (4.27) and average the resulting coupling strengths, where it shows to be convenient to include only the orbitals having a positive overlap. Therefore we neglect the gold orbitals having a negative overlap with the effective orbital of the sulfur atoms. Although this procedure is very heuristic it serves our purpose. We calculate the overlap of the model electrodes in the exact same way. The model parameters resulting from this procedure are summarized in Tab. 4.3.

Tab. 4.3. Coupling strength t and overlap S of the $\mathrm{p_z}$ orbitals of the sulfur atoms and the s orbitals of the electrodes entering the model. $\mathrm{S_j}$ and $\mathrm{s_j}$ denote the $\mathrm{p_z}$ orbital of the sulfur atoms and the s orbitals of the electrodes, respectively. We estimated the coupling strengths using Eq. (4.27) and the procedure described in the main text. We estimated the overlaps in the same way as the coupling strengths.

Configuration	$\mathrm{t_{S_l s_l}}$ / eV	$\mathrm{t_{S_r s_r}}$ / eV	$\mathrm{S_{S_l s_l}}$	$\mathrm{S_{S_r s_r}}$
Meta	-0.67	-0.68	0.08	0.08
Para	-0.81	-0.83	0.10	0.10

Due to the strong angular dependence of the d orbitals, the coupling strength of the d orbitals depends strongly on the exact position of the sulfur atoms relative to the electrodes. Therefore we do not estimate the coupling of the d orbitals, but choose it to be $t_{\mathrm{Cd}} = -0.5$ for both electrodes. We also assume that the modeled d orbitals of the electrodes and the orbitals of the BDT are orthonormal ($\mathrm{S_{S_j d_j}} = 0$).

4.3.2 TC model and TC_π model

Now we calculate the transmissions of the different channels within the TC approximation. We see in Fig. 4.12 that the transmission of the p-channel is greatly reduced at the Fermi energy for meta-BDT+planar compared to the transmission of the p-channel in Fig. 4.9. The transmission of the meta-BDT+planar system within the TC model has a reduced transmission also around $-2\,\mathrm{eV}$ and at $2.825\,\mathrm{eV}$, which is in qualitative agreement with the transmission from Fig. 4.6. For DQI one has to consider only the p-channel and enforce tight coupling.

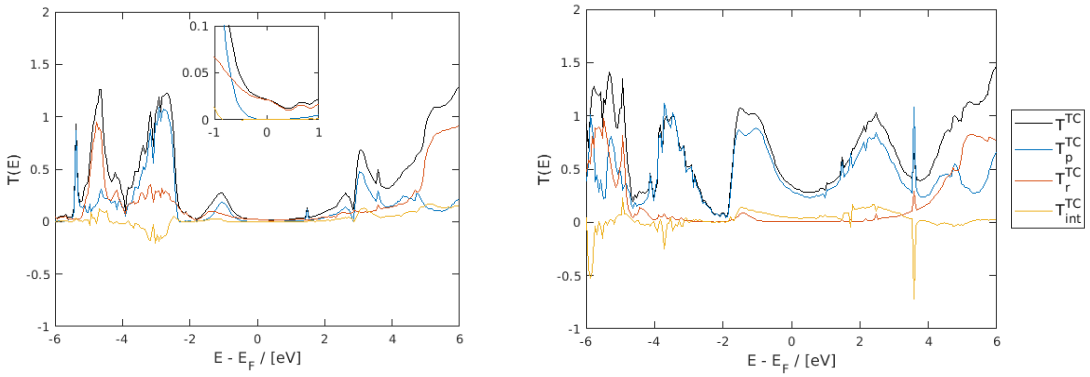

Fig. 4.12. Transmission of meta-BDT+planar (left) and para-BDT+planar (right) in the TC model. DQI occurs in the case that tight-coupling is enforced and only the p-channel is considered. In the case of meta-BDT+planar the p-channel has also a very small transmission at about $-2\,\mathrm{eV}$ and at $2.825\,\mathrm{eV}$, which is in qualitative agreement with the results of the Hückel model from Sec. 4.1.2.

The Hückel model considers only the p_z orbitals of hydrocarbons explicitly and treats the remaining orbitals as an additional contribution to the potential the electrons of the p_z orbitals feel (see Sec. 2.2). For this approach the π-electron approximation has to be reasonable. To see how the π-electron approximation influences the transmission, we rearrange the Hamiltonian matrix, the overlap matrix and hybridization matrices of the BDT molecule and weight the coupling of the two channels

$$E^+\mathbf{S}_{\mathrm{BDT}} - \mathbf{H}_{\mathrm{BDT}} - \mathbf{\Sigma}^{\mathrm{TC}}_{\mathrm{C_L}} - \mathbf{\Sigma}^{\mathrm{TC}}_{\mathrm{C_R}} = \overline{\mathbf{H}}_{\mathrm{BDT}}(E) = \begin{pmatrix} \overline{\mathbf{H}}_{\mathrm{p}} & \epsilon\overline{\mathbf{H}}_{\mathrm{pr}} \\ \epsilon\overline{\mathbf{H}}_{\mathrm{rp}} & \overline{\mathbf{H}}_{\mathrm{r}} \end{pmatrix} \tag{4.28}$$

with $\epsilon \in [0, 1]$. $\overline{\mathbf{H}}_{\mathrm{p}}$ and $\overline{\mathbf{H}}_{\mathrm{r}}$ are the Hamiltonian matrices of the two channels. $\overline{\mathbf{H}}_{\mathrm{pr}}$ and $\overline{\mathbf{H}}_{\mathrm{rp}}$ describe the coupling of the two channels to one another. $\mathbf{\Sigma}^{\mathrm{TC}}_{\mathrm{C_L}}$ and $\mathbf{\Sigma}^{\mathrm{TC}}_{\mathrm{C_R}}$ are the hybridization matrices within the TC model. Using the Hamiltonian matrix (4.28) we calculate the transmission for various values of ϵ, where $\epsilon = 1$ results in the TC model and $\epsilon = 0$ in the TC_π model. Fig. 4.13 shows the results.

Fig. 4.13 shows that the π-electron approximation is a quite good approximation for the para-BDT+planar system, while it seems to be less so for the meta-BDT+planar system. By taking a closer look at the transmission of the meta-BDT+planar system, we see that the reduction of the coupling of the p-channel and r-channel shifts the energy, at which DQI occurs, towards lower energies. The seemingly bad agreement of the transmission peaks at about $-3\,\mathrm{eV}$ and $3\,\mathrm{eV}$ in Fig. 4.13 arises from shifting the DQI towards lower energies. Due to the shifting towards lower energies the DQI "cuts" these two transmission peaks at different energies. In consequence, the transmission changes more drastically in the case of meta-BDT+planar.

While the transmission of the meta-BDT+planar changes considerably, we see in Fig. 4.13 that also the transmission of the para-BDT+planar system changes at higher energies, which we assume to result from the first-principles calculations containing orbitals which are not considered in the π-electron approximation. The π-electron approximation considers hydrocarbons having only π orbitals and σ orbitals. The basis of the BDT within the first-principles calculations, being a DZP basis, contains also d orbitals, and in consequence δ orbitals. These d orbitals are several eV higher in energy than the remaining orbitals of carbon and sulfur and therefore they make greater contributions to the transmission of the p-channel at higher energies.

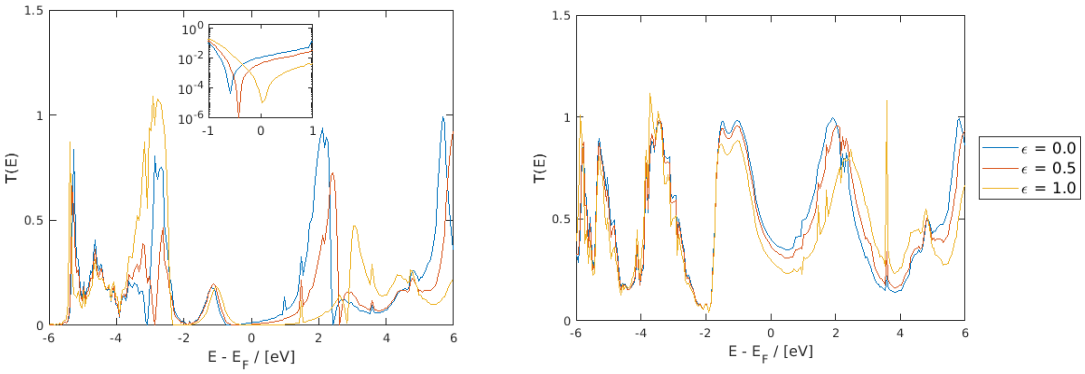

Fig. 4.13. Impact of the π-electron approximation on the transmission of the p-channel of the tightly coupled meta-BDT+planar (left) and para-BDT+planar (right). $\epsilon = 1$ corresponds to the TC model, while $\epsilon = 0$ corresponds to the TC_π model. The π-electron approximation is reasonable for the para-BDT, while the transmission of the meta-BDT changes considerably due to the DQI being shifted.

4.3.3 TC_π^{SO} model, TB model and Hückel model

Using the procedure from Sec. 3.2.2.3, we reduce the Hamiltonian matrices of the first-principles calculations to obtain the Hamiltonian matrices of the TC_π^{SO} model. We further reduce the Hamiltonian matrices of the TC_π^{SO} model to Hamiltonian matrices of the TB model and in one further step to Hamiltonian matrices of the Hückel model. We calculate the transmission for all three of the models and plot the results in Fig. 4.14. By comparing Figs. 4.13 and 4.14 we see that the TB and Hückel model compensate the shift of the transmission peaks, which was introduced by decoupling the p-channel and r-channel within the π-electron approximation.

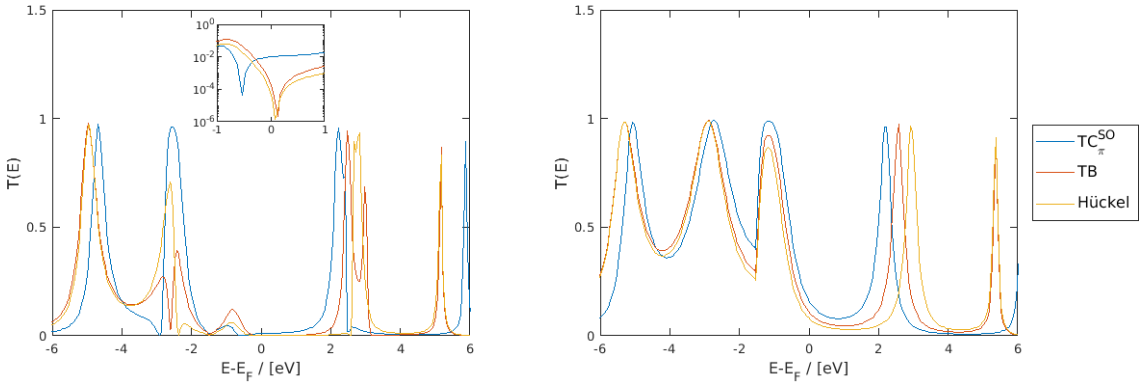

Fig. 4.14. Comparison of the TC_π^{SO} model, TB model and Hückel model of meta-BDT+planar (left) and para-BDT+planar (right). The TB model and Hückel model correct the shift introduced by the π-electron approximation to some extent.

We compare now the parameters of the Hückel model taken from literature and taken from the first-principles calculations. The parameters are summarized in Tab. 4.4.

Tab. 4.4. Comparison of the Hückel parameters from literature to the ones from the first-principles calculations. As we see the parameters of the Hückel model taken from literature and the parameters we obtained from the first-principles calculations differ considerably.

	first-principles / [eV]		Literature/ [eV]
	Meta	Para	
$\varepsilon_S - \varepsilon_C$	-2.31	-2.99	-1.30
t_C	-2.48	-2.65	-2.60
t_{SC}	-1.58	-1.80	-0.87

As we see in Tab. 4.4, the hopping parameters t_{SC} and the difference of the onsite energies $\varepsilon_S - \varepsilon_C$ gained from the first-principles calculations and from literature differ considerably. For examining the hopping parameters we compare the bond lengths of the BDT molecules of the DFT systems to the system considered in Sec. 4.1. The electrodes in the first-principles calculations exhibit forces on the BDT, resulting in the sulfur atoms being pressed closer to the carbon ring. Therefore the carbon-sulfur bond length from literature and from the DFT calculations differ (by about 35 %) and in consequence also t_{SC}. The carbon ring is more stable and the carbon-carbon bond length is about the same as the one from literature. The onsite energies of the atoms depend considerably on the effective potential of the Kohn-Sham Hamiltonian.

We compare the results from the first-principles calculations to the results from the Hückel model parametrized from the first-principles calculations in Fig. 4.15. We see in Figs. 4.15d and 4.15f that the sharp peaks at about $-3\,\mathrm{eV}$ and $3\,\mathrm{eV}$ present in the PDOS from the first-principles calculations of the para-BDT+planar system are not present in the Hückel model. We also see in Fig. 4.15e that the PDOS of the carbon atoms at site 1 and 3 of the meta-BDT vanish around the Fermi energy in the Hückel model but not in the first-principles calculations. By calculating the total PDOS of the model system, from e.g. Eq. (2.121), instead of calculating only the scattering PDOS according to Eq. (4.20), the sharp peaks at about $-3\,\mathrm{eV}$ and $3\,\mathrm{eV}$ in the case of the para-BDT appear also in the Hückel model and the PDOS of the carbon atoms at site 1 and 3 in the case of the meta-BDT are finite at the Fermi energy. We see that in the first-principles calculations the p-channel contains contributions, which the hybridization matrices within the Hückel model do not support, namely contributions from the direct coupling of the carbon atoms to the electrodes. This result is in good agreement with the fact that DQI is only observed after we turn off the additional coupling in the TC model.

We see in Fig. 4.15a that the transmission of the Hückel model does not occur at the Fermi energy but at an energy of (0.075 ± 0.05) eV. This shift of the DQI results from the onsite energy of the carbon atoms within the Hückel model being $0.09\,\mathrm{eV}$ higher in energy than the Fermi energy and therefore according to Sec. 2.6.3 also the DQI. We recalculate the transmission of the meta-BDT+planar system within the Hückel model with an energy resolution of $0.001\,\mathrm{eV}$. We find the transmission minimum now at (0.091 ± 0.001) eV.

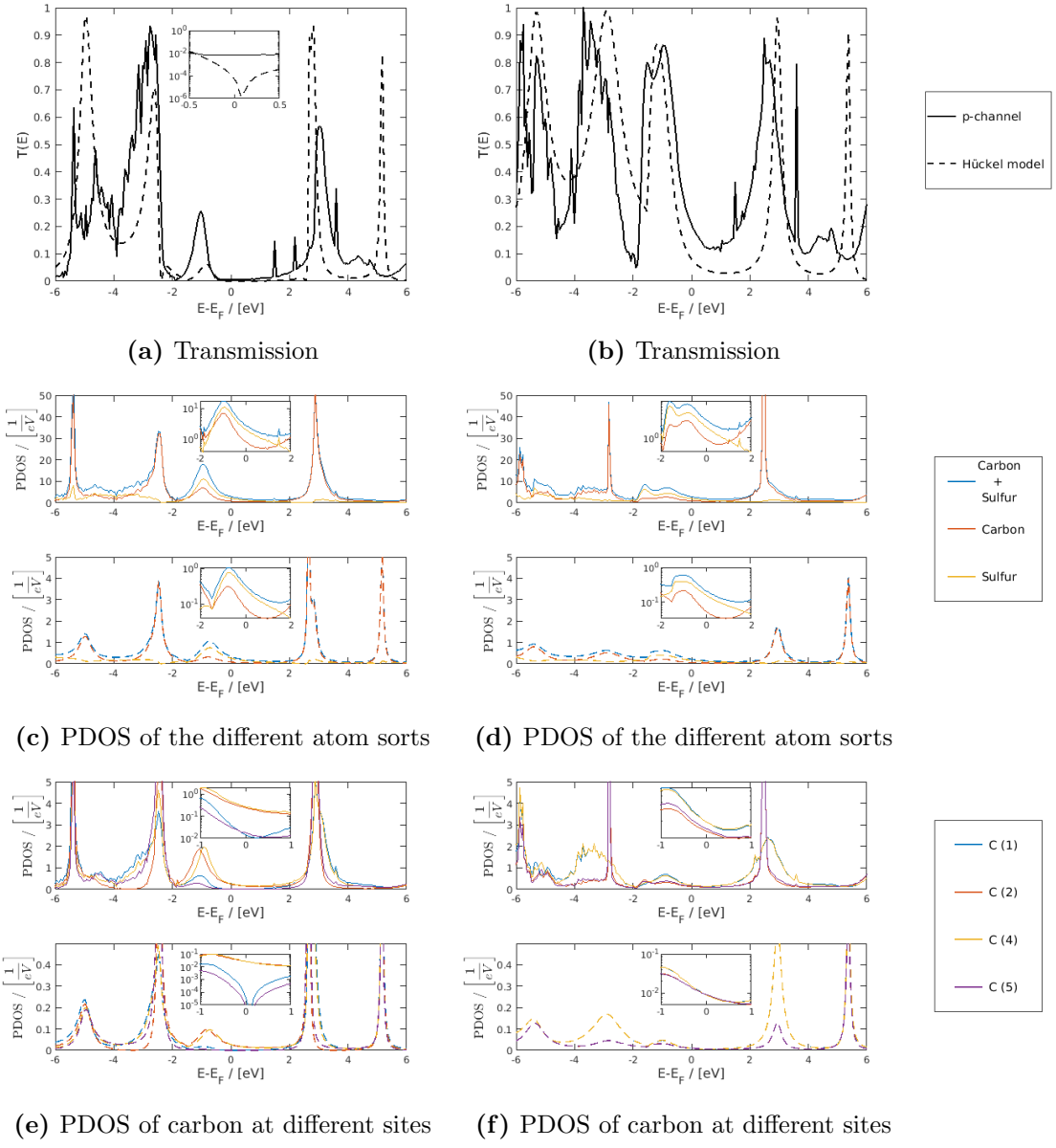

(a) Transmission **(b)** Transmission

(c) PDOS of the different atom sorts **(d)** PDOS of the different atom sorts

(e) PDOS of carbon at different sites **(f)** PDOS of carbon at different sites

Fig. 4.15. Comparison of the p-channel of the DFT calculations to the Hückel model parametrized from the first-principles calculations of meta-BDT+planar (left) and para-BDT+planar (right). We calculated the transport properties with the same energy resolution as the first-principles calculation, i.e. ΔE =0.05 eV. **Note:** We compare the PDOS of both basis functions describing the p_z orbitals in the first-principles calculations to the PDOS of the effective orbitals in the model.

4.4 DFT calculations out of equilibrium

We drive the transport systems out of equilibrium by a bias voltage U_B. According to Sec. 2.5 this results in the chemical potential being shifted. We consider this shift within the TRANSIESTA calculations in the following way: The chemical potential of the left electrode is increased by $\frac{|eU_B|}{2}$ and the chemical potential of the right electrode reduced by the same amount.

In Sec. 4.4.1 we study how the transmission and PDOS of the transport systems change in non-equilibrium. Sec. 4.4.2 deals with the influence of the bias voltage on the system Hamiltonians, while Sec. 4.4.3 focuses on the onsite energies. In Sec. 4.4.4 the focus lies on the benzene rings and their PDOS. Sec. 4.4.5 takes a look at the currents across the transport systems.

4.4.1 Transmission and DOS

We calculate the transmission and PDOS of the different transport systems in non-equilibrium. The PDOS of gold is several times larger than the PDOS of the remaining atom species due to the large difference in the atomic numbers. To allow for better comparability, we divide the PDOS of each atom species by the number of atoms of that species. Additionally, we split the PDOS of the pointed electrodes into contributions from the electrode tips and contributions from the gold atoms not part of the tips. We plot the PDOS and the transmission of the BDT+planar systems in Fig. 4.16 and of the BDT+pointed systems in Fig. 4.17.

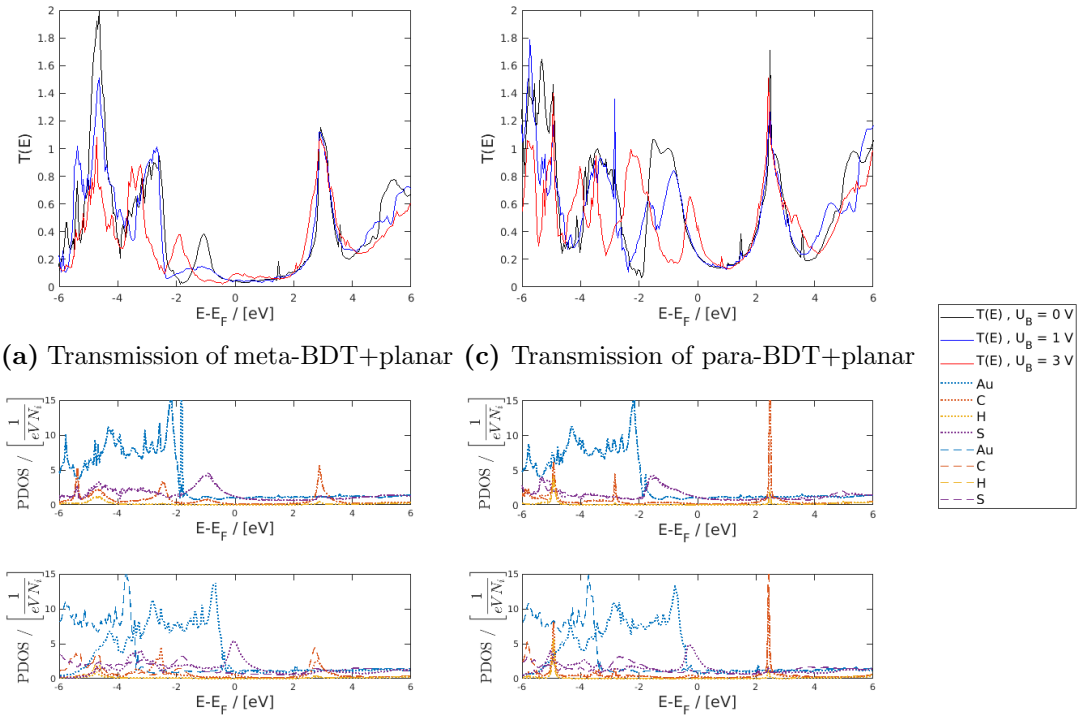

(a) Transmission of meta-BDT+planar

(c) Transmission of para-BDT+planar

(b) PDOS of meta-BDT+planar for $U_B = 0\,V$ (above) and $U_B = 3\,V$ (below)

(d) PDOS of para-BDT+planar for $U_B = 0\,V$ (above) and $U_B = 3\,V$ (below)

Fig. 4.16. Transmission and PDOS from the left (dotted) and right (dashed) spectral function of the BDT+planar systems. For better comparability, the PDOS of each element is divided by the number of atoms of the corresponding element. The transmission peaks right below the Fermi energy and the transmission in the energy range of the d-orbitals change considerably with respect to the bias voltage.

By comparing Figs. 4.16 and 4.17 we see that the bias voltage changes the transmission of the BDT+planar system considerably below the Fermi energy, while the transmission of the BDT+pointed systems change across the whole energy range with respect to the bias voltage. We know from Fig. 4.11 that the PDOS of the d orbitals of the planar electrodes and the s and d orbitals of the pointed electrodes have an energy-dependent structure. By applying bias voltage the PDOS of the electrodes changes and in further consequence the transmission.

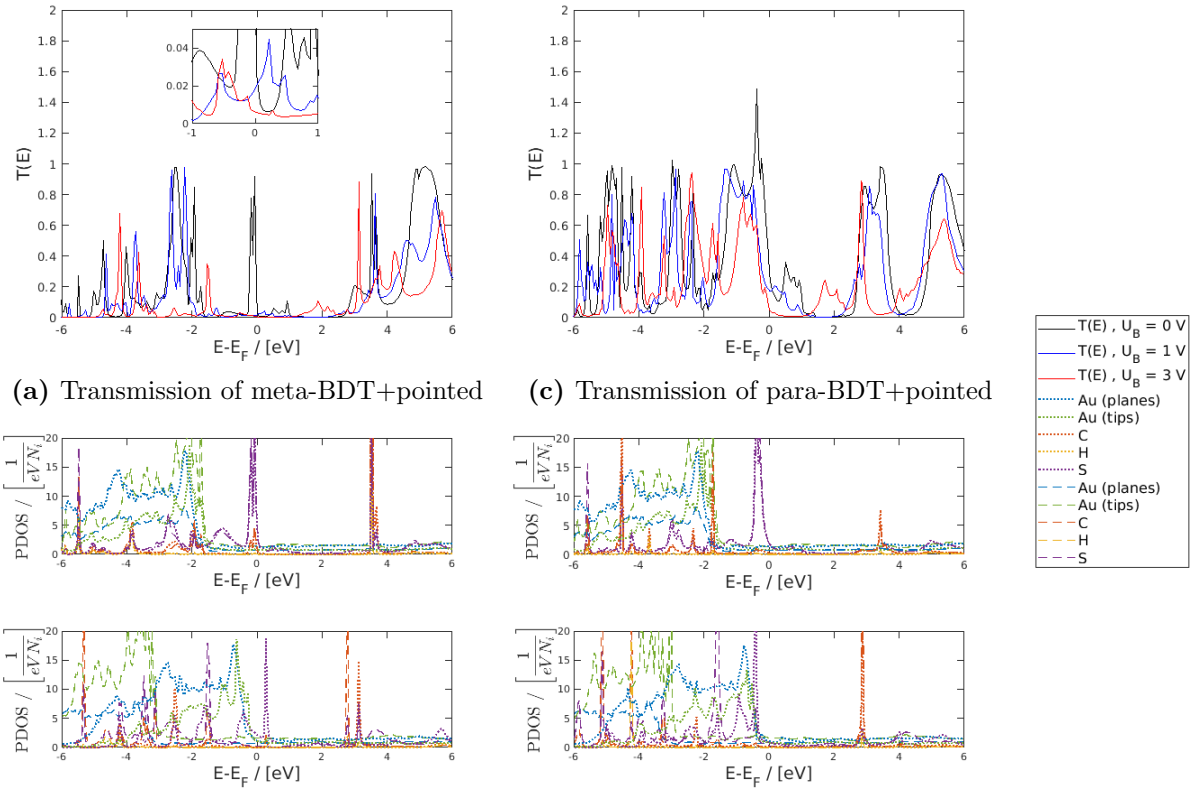

(a) Transmission of meta-BDT+pointed

(c) Transmission of para-BDT+pointed

(b) PDOS of meta-BDT+pointed for $U_B = 0\,V$ (above) and $U_B = 3\,V$ (below)

(d) PDOS of para-BDT+pointed for $U_B = 0\,V$ (above) and $U_B = 3\,V$ (below)

Fig. 4.17. Transmission and PDOS from the left (dotted) and right (dashed) spectral function of the BDT+pointed systems. For better comparability the PDOS of each element is divided by the number of atoms of the corresponding element. Unlike in the case of the BDT+planar systems the transmission changes considerably throughout the whole energy range.

We observe in Figs. 4.16 and 4.17 that the PDOS of the carbon atoms are less shifted by U_B than the PDOS of the sulfur atoms. The sulfur atoms couple stronger to the electrodes than the carbon atoms and therefore the influence of the bias voltage on the sulfur atoms is stronger than on the carbon atoms.

We also observe the shift of the PDOS of the sulfur atoms in some of the systems, e.g. Fig. 4.16b, to be smaller than the applied bias voltage. The PDOS of the carbon atoms of all four of the systems is even less shifted. In the case of pointed electrodes the bias voltage also shifts the PDOS of the sulfur contacted to the left electrode less than the sulfur contacted to the right electrode as we see in Figs. 4.17b and 4.17d. To understand why the carbon and sulfur peaks show this behavior, we study the influence of the bias voltage on the system Hamiltonian in Sec. 4.4.2 and take a closer look at the energy shift of these Hamiltonians due to the bias voltage in Sec. 4.4.3.

4.4.2 Influence of the bias voltage on the system Hamiltonian

We determine the influence of the bias voltage on the matrix elements of the Hamiltonians by calculating the difference of the Hamiltonian matrices resulting from the first-principles calculations in equilibrium and in non-equilibrium

$$\Delta\mathbf{H} = \mathbf{H}_{\mathrm{TS}}^{\mathrm{NEQ}} - \mathbf{H}_{\mathrm{TS}}^{\mathrm{EQ}} \,, \tag{4.29}$$

where $\mathbf{H}_{\mathrm{TS}}^{\mathrm{EQ}}$ and $\mathbf{H}_{\mathrm{TS}}^{\mathrm{NEQ}}$ are the Hamiltonian matrices from the TRANSIESTA calculations in equilibrium and non-equilibrium, respectively. We take $\mathbf{H}_{\mathrm{TS}}^{\mathrm{NEQ}}$ to be the Hamiltonian matrices from the calculations with $\mathrm{U_B} = 3\,\mathrm{V}$. Fig. 4.18 shows $\Delta\mathbf{H}$ of the Hamiltonian matrices at the Γ-point. The influence of the bias voltage on the hopping parameters is small in comparison to the influence on the onsite energies.

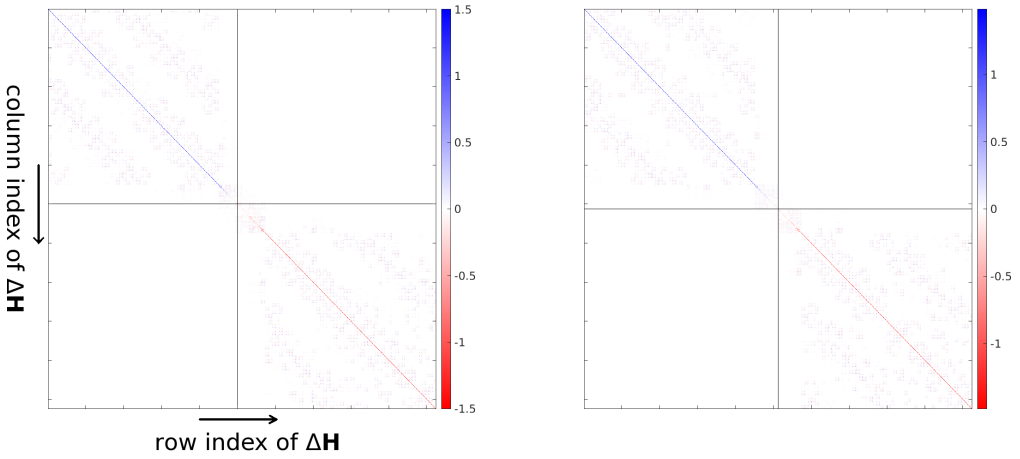

(a) meta-BDT+planar

(c) para-BDT+planar

(b) meta-BDT+pointed

(d) para-BDT+pointed

Fig. 4.18. Influence of the bias voltage on the Hamiltonian matrices of the transport systems. The horizontal and vertical lines mark the center of the central region along the transport direction. The plots show only the influence on the atoms, which are part of the central region but not of the electrode clusters within the central region. The bias voltage influences the onsite energy, while the hopping parameters are less affected. We observe that the bias voltage influences the onsite energy of the BDT+pointed systems asymmetrically. We study this asymmetry in more detail in the next section.

4.4.3 Voltage drop across the transport system

We know from Sec. 4.4.2 that a bias voltage shifts the onsite energies of the Hamiltonians. We determine this energy shift by calculating the difference of the onsite energies in equilibrium and non-equilibrium for the various voltages. Fig. 4.19 shows the shift of the onsite energies at the sites along the transport direction.

We observe that only a small part of the voltage drop occurs in the planar electrodes and in the parts of the pointed electrodes not part of the tips, while the voltage drop in the tips of the pointed electrodes is larger. We understand this behavior in terms of the states, each electrode layer provides. Within the tips the number of gold atoms, and therefore the number of states supporting electron transport, decreases. In consequence, the conductivity of the electrodes decreases within the tips resulting in a larger voltage drop.

The benzene ring is only little influenced by the bias voltages as we see in Fig. 4.19. We also observe that on average the BDT molecule is shifted towards lower energies. This shift has to arise from an asymmetry within the transport systems. We also observe that the BDT+pointed systems display a larger shift of the onsite energies than the BDT+planar systems. Therefore we discuss this asymmetry at the example of the meta-BDT+pointed system in more detail. We take a closer look at the distances involved. The left electrode and the left sulfur are 2.51 Å apart, while the right electrode and the right sulfur are 2.49 Å apart. In the next step, we compare the overlap of the BDT orbitals with the orbitals of the electrodes. Tab. 4.5 shows the overlap of the s orbitals of the gold atoms at the electrode tips and the p_z orbitals of the neighboring sulfur atoms.

Tab. 4.5. Overlap of the s orbital of the electrode tip and the p_z orbital of the nearest-neighboring sulfur atom of the meta-BDT+pointed system. We calculated the overlap of the orbitals by summing the four overlaps of the two basis functions describing the s orbital and the two basis functions describing the p_z orbital. We see that the asymmetry of the BDT position results in the orbitals of the left and right electrodes having different overlaps with the BDT molecule, causing the asymmetrical energy shift.

Left side	Right side
0.03	0.07

While the difference in the distances of the sulfur atoms towards the corresponding electrodes is small, Tab. 4.5 shows that the resulting overlaps differ considerably. In consequence, also the coupling of the left and right electrode towards the BDT differ. The smaller energy shift of the BDT+planar systems results from a smaller difference of the coupling of the BDT molecule towards the electrodes as the couplings from Tab. 4.3 indicate, where we estimated the parameters of Tab. 4.3 from the DFT calculations. We see that small deviations in the BDT position relative to the electrodes impact the results considerably. Therefore the coupling of the BDT, especially the coupling of the sulfur atom, towards the electrodes is of major importance.

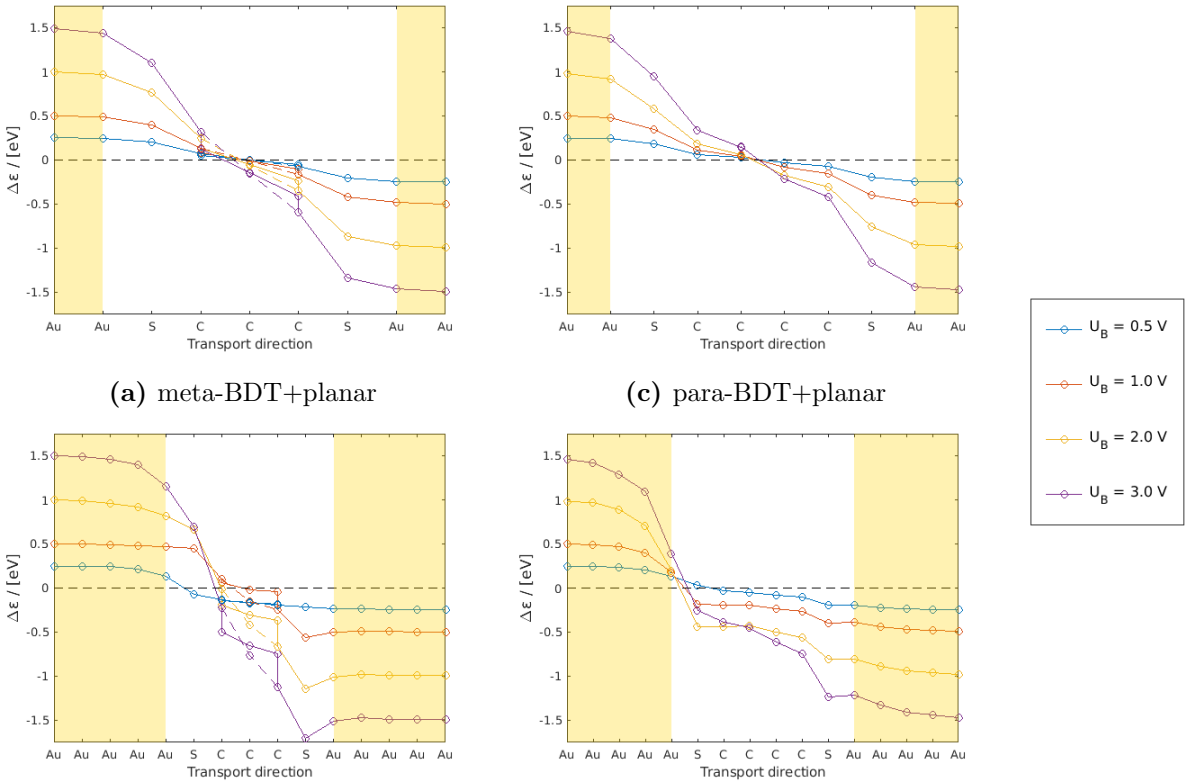

(a) meta-BDT+planar **(c)** para-BDT+planar

(b) meta-BDT+pointed **(d)** para-BDT+pointed

Fig. 4.19. The energy shift $\Delta\varepsilon$ introduced by the bias voltage U_B. We calculated $\Delta\varepsilon$ by averaging the energy shift of all orbitals of the same atom. In the case of gold atoms we further averaged the energy shift of the gold atoms of the same electrode layer. In the case of the meta-BDT systems we distinguish the shorter (dashed) and longer (solid) path of the benzene rings. The golden background marks the electrode parts of the systems, while the white background marks the BDT molecule. We do not plot the energy shift of the hydrogen atoms here. We see that part of the voltage drop occurs at the electrodes, where a large part of the voltage drop occurs at the tips of the pointed electrodes. We also observe that the benzene rings of the BDT molecules are effectively shifted towards lower energies.

4.4.4 Integrated PDOS of the benzene ring

In this section we study how the bias voltage influences the PDOS of the benzene rings. Similarly to Sec. 4.1.2, we calculate the integrated PDOS of the benzene ring

$$\Big(\text{Integrated PDOS}\Big)_i = \int_{-0.5}^{+0.5} \Big[\Big(\text{PDOS}_\text{L}(E)\Big)_i + \Big(\text{PDOS}_\text{R}(E)\Big)_i\Big] dE \,, \tag{4.30}$$

where PDOS_L and PDOS_R are the PDOS calculated by TBTRANS from the left and right spectral function. Fig. 4.20 shows the integrated PDOS of the systems at different bias voltages.

By comparing Figs. 4.5 and 4.20 we see that the integrated PDOS from the Hückel model parametrized with values taken from literature and the first-principles calculations of the meta-BDT+planar, meta-BDT+pointed and para-BDT+planar are in good agreement. The para-BDT+pointed system however, does not agree with the Hückel model. As we discussed in Sec. 4.2.2.1, we assume this discrepancy to result from the TRANSIESTA orbitals not coinciding with the orbitals of the benzene ring. In the case of the meta-BDT+pointed system we observe the integrated PDOS to decrease considerably with respect to U_B. As we have seen in Sec. 4.4.1, the bias voltage shifts the prominent sulfur peak out of the considered interval. In consequence, also the number of states, the sulfur atoms induce at the benzene ring, decreases in non-equilibrium.

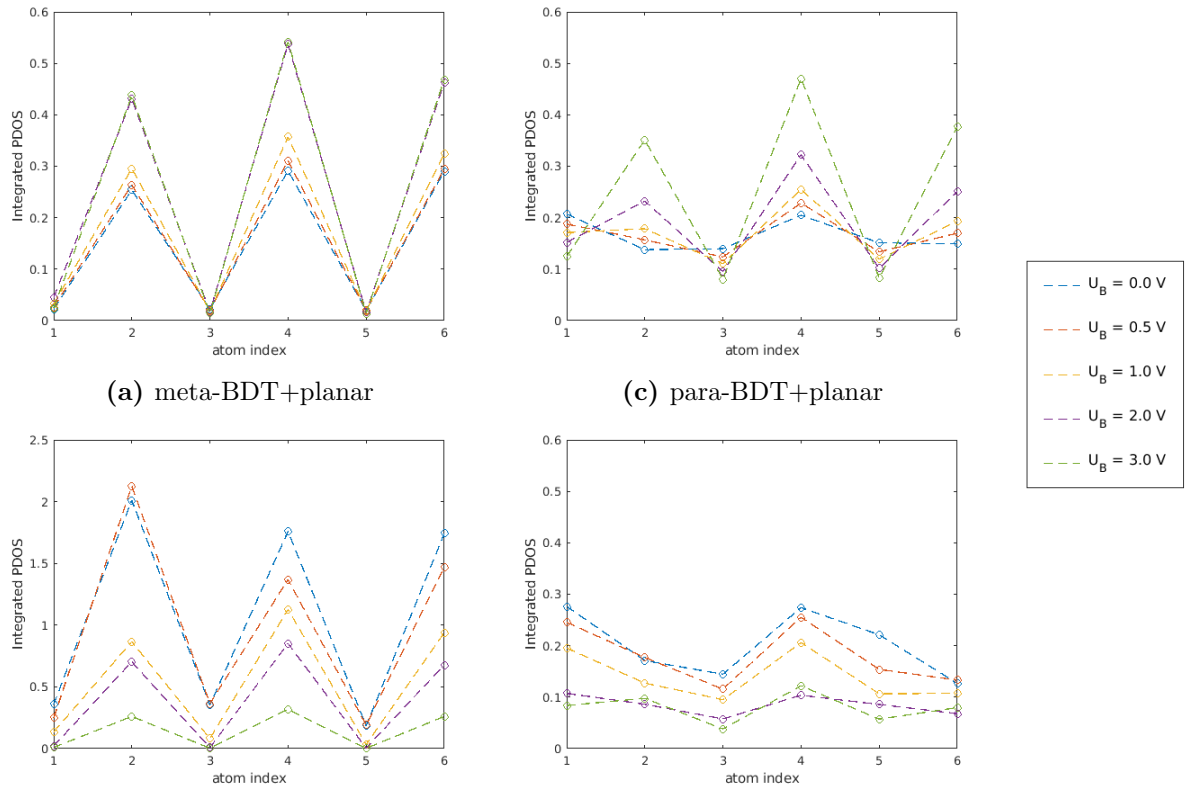

(a) meta-BDT+planar **(c)** para-BDT+planar

(b) meta-BDT+pointed **(d)** para-BDT+pointed

Fig. 4.20. PDOS of the p_z orbitals of the TRANSIESTA calculations integrated over the interval [-0.5 0.5] eV. We calculated the integrated PDOS from the TBTRANS results using the trapezoidal rule. The atom indices are chosen according to Fig. 2.6. Like the benzene ring of the model calculations from Sec. 4.1.2, the benzene ring of the meta-BDT systems has considerably less states at odd sites. At higher bias voltages the para-BDT+planar system displays a zigzag characteristic like the meta-BDT systems.

We observe in Fig. 4.20c that in the case of the para-BDT+planar system the number of states at even sites increases and decreases at odd sites. By examining Fig. 4.16 we are able to explain this behavior of the para-BDT+planar system. In equilibrium both sulfur atoms induce about an equal number of states at the different carbon sites. By applying a bias voltage the right sulfur atom is energetically shifted out of the considered energy interval and therefore also the states that are induced by it, resulting in a reduction of the number of states at odd sites in the process. The left sulfur atom, and therefore the states induced by it, is energetically shifted into the considered interval, resulting in an increase of the number of states at even sites in the process.

4.4.5 I-U-characteristics

Being another important property of the transport systems, we study the current through the molecules in this section. Fig. 4.21 shows the I-U-characteristics and the current ratio of the different systems resulting from the first-principles calculations. The currents of the meta-BDT systems are lower than the currents of the para-BDT systems. Additionally, we see that the current in the case of the meta-BDT+pointed system is lower than in the case of the meta-BDT+planar system providing a better meta-to-para-current ratio.

We see in Fig. 4.21 that the meta-BDT+pointed system displays a negative differential conductivity. The current for a bias voltage of 0.5 V is higher than the current for a bias voltage of 1.0 V. We understand this negative differential conductivity by considering Fig. 4.17 and Eq. (2.120). The current depends on the transmission as well as on the Fermi window $[f_{\mathrm{L}}(E,\mu_{\mathrm{L}}) - f_{\mathrm{R}}(E,\mu_{\mathrm{R}})]$as we see in Eq. (2.120). The sulfur atoms of the meta-BDT+pointed system provide a high PDOS across a small energy range right next to the Fermi energy. As we see in Fig. 4.17 the bias voltage shifts this PDOS of the sulfur atoms, reducing the PDOS supporting the transmission of the meta-BDT+pointed system. By doing so the bias voltage reduces the transmission of the meta-BDT+pointed system, while the bias voltage also increases the Fermi window. The negative differential conductivity of the meta-BDT+pointed system results from the transmission decreasing faster than the Fermi window increases.

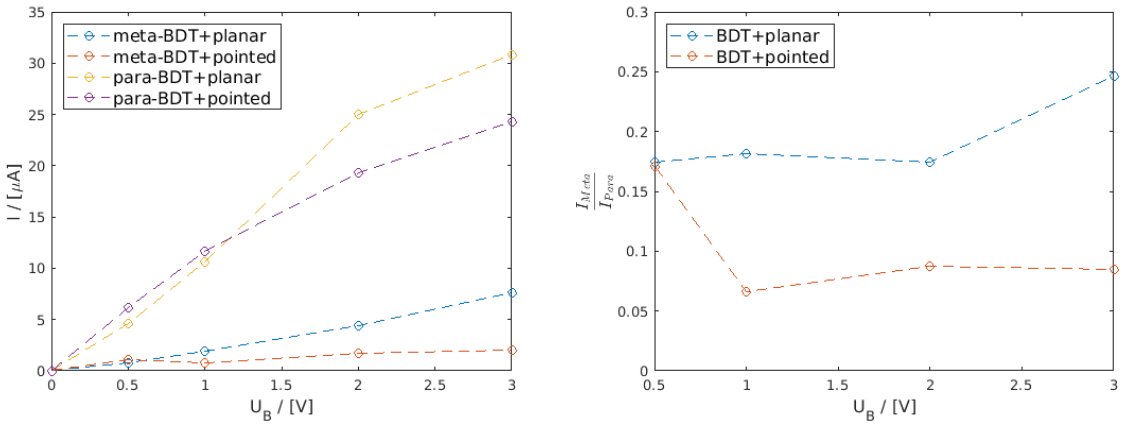

Fig. 4.21. I-U-characteristics (left) and current ratio $\frac{I_{\mathrm{Meta}}}{I_{\mathrm{Para}}}$ (right) for the different systems. The current through the para-BDT systems is higher than through the meta-BDT systems. The current through the meta-BDT+planar system is higher than through the meta-BDT+pointed system resulting in a better current ratio $\frac{I_{\mathrm{Meta}}}{I_{\mathrm{Para}}}$ for the BDT+pointed systems.

4.5 Model calculations out of equilibrium

In this section we model the systems in non-equilibrium. We limit the model calculations to the simple models, namely the TC_π^{SO} model and the Hückel model. In Sec. 4.5.1 we study the influence of the bias voltage on the Hamiltonian matrices of the TC_π^{SO} model. Using the results from Sec. 4.5.1, we apply in Sec. 4.5.2 the GAOS to meta-benzene in non-equilibrium. In Sec. 4.5.3 we calculate the transmission of the BDT+planar systems within the TC_π^{SO} model and study how the non-equilibrium influences the DQI.

4.5.1 Influence of the bias voltage on the model parameters

We reduce the TRANSIESTA Hamiltonian matrices of the BDT+planar systems in equilibrium and in non-equilibrium to TC_π^{SO} Hamiltonian matrices using the procedure from Sec. 3.2.2.3. To determine the influence of the bias voltage on the model parameters we calculate the difference of the model Hamiltonian matrices. The difference of the model Hamiltonian matrices of the meta-BDT+planar system with a bias voltage of 3 eV and in equilibrium gives

$$\Delta\mathbf{H}_{\text{Meta}}=\mathbf{H}^{\text{NEQ}}_{\text{Meta}}-\mathbf{H}^{\text{EQ}}_{\text{Meta}}=\begin{pmatrix} 1.11 & 0.01 & 0.00 & 0.00 & -0.00 & 0.00 & 0.00 & 0.00 \\ 0.01 & 0.30 & 0.00 & -0.00 & -0.00 & -0.01 & -0.01 & -0.00 \\ 0.00 & 0.00 & -0.15 & -0.00 & 0.01 & 0.00 & -0.01 & -0.00 \\ 0.00 & -0.00 & -0.00 & -0.59 & 0.00 & 0.00 & 0.00 & -0.01 \\ -0.00 & -0.00 & 0.01 & 0.00 & -0.40 & 0.00 & -0.00 & -0.00 \\ 0.00 & -0.01 & 0.00 & 0.00 & 0.00 & -0.15 & -0.01 & -0.00 \\ 0.00 & -0.01 & -0.01 & 0.00 & -0.00 & -0.01 & 0.11 & 0.00 \\ 0.00 & -0.00 & -0.00 & -0.01 & -0.00 & -0.00 & 0.00 & -1.37 \end{pmatrix}. \tag{4.31}$$

Eq. (4.31) shows that the bias voltage influences the onsite energy considerably, while the influence of the bias voltage on the hopping parameters is small in comparison. By calculating the influence of the bias voltage on the model parameters of the para-BDT+planar system we get the same result: the onsite energies are strongly influenced by the bias voltage, while the influence on the hopping parameters is small in comparison.

4.5.2 GAOS

By taking advantage of the results from Sec. 4.5.1 we are able to use the GAOS also in non-equilibrium. We restrict ourselves once again to a Hückel model and a benzene molecule. We consider the bias voltage in the Hückel Hamiltonian by shifting the onsite energies of the benzene ring according to Eq. (2.132), where we take the shift of the onsite energies from Eq. (4.31). Before applying the GAOS to the systems in non-equilibrium we rewrite the onsite energy and the energy shift to serve our purpose better. We know from Sec. 4.4.3 that the onsite energies are shifted effectively towards lower energies. We split the energy shifts of the carbon atoms into a contribution containing the effective shift and a contribution containing the remaining shift

$$\varepsilon_{\mathrm{j}}^{\mathrm{U_B}} = \varepsilon_{\mathrm{j}}^{\mathrm{U_B}=0V} + \Delta\varepsilon_{\mathrm{j}} = \underbrace{\varepsilon_{\mathrm{j}}^{\mathrm{U_B}=0V} - \Delta\varepsilon_{\mathrm{shift}}}_{\varepsilon'_{\mathrm{j}}} + \Delta\varepsilon'_{\mathrm{j}} \,, \tag{4.32}$$

where $\varepsilon_{\mathrm{j}}^{\mathrm{U_B}}$ is the non-equilibrium onsite energy of the carbon atom at site j. $\varepsilon_{\mathrm{j}}^{\mathrm{U_B}=0}$ and $\Delta\varepsilon_{\mathrm{j}}$ are the onsite energy in equilibrium and the energy shift due to the bias voltage of the carbon atom at site j. $\Delta\varepsilon_{\mathrm{Shift}}$ and $\Delta\varepsilon'_{\mathrm{j}}$ are the effective shift resulting from the asymmetry of the system and the energy shift arising from the bias voltage reduced by the effective shift, respectively.

Using the GAOS we analyze the occurrence of DQI in meta-benzene in non-equilibrium. We take the energy shift $\Delta\varepsilon_{\mathrm{j}}$ of each carbon atom of meta-benzene for a bias voltage of 3 V to be the ones from Eq. (4.31) and set $\Delta\varepsilon_{\mathrm{shift}} = 0.15$. Tab. 4.6 contains the resulting energy shifts $\Delta\varepsilon'_{\mathrm{j}}$. Fig. 4.22 shows the labeling of the carbon sites we use in Tab. 4.6.

Tab. 4.6. Energy shift of the carbon atoms of the meta-BDT+planar system ($\mathrm{U_B} = 3\,\mathrm{V}$). The effective energy shift of the benzene ring has been subtracted (see main text). The carbon sites are labeled according to Fig. 4.22

j	$\Delta\varepsilon'_{\mathrm{j}}$ / eV
1	0.45
2	0.00
3	-0.44
4	-0.25
5	0.00
6	0.26

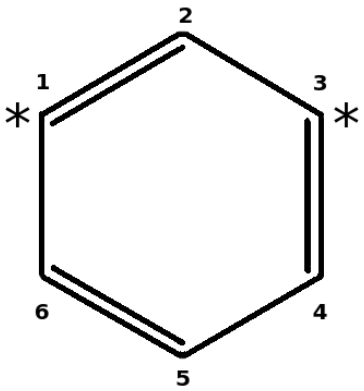

Fig. 4.22. Labeling of the carbon atoms in Tab. 4.6. The stars indicate the sites coupled to the electrodes

Due to the symmetry of the benzene molecule the energy shifts are given as $\Delta\varepsilon'_1 \approx -\Delta\varepsilon'_3$ and $\Delta\varepsilon'_4 \approx -\Delta\varepsilon'_6$ as we see in Tab. 4.6. To simplify the calculation we assume equality of these pairs. Now we assume a Hückel model and we set the onsite energy to be $\varepsilon'_{\mathrm{j}} = \varepsilon_{\mathrm{C}} - 0.15$. By doing so we can use Eq. (2.150), which becomes

$$\begin{aligned} M_{13}(E) = {} & (-1)^0 t_{\mathrm{C}}^2 (E - \varepsilon_{\mathrm{C}} + 0.15)(E - \varepsilon_{\mathrm{C}} + 0.15 + \Delta\varepsilon)(E - \varepsilon_{\mathrm{C}} + 0.15 - \Delta\varepsilon) \\ & + (-1)^1 t_{\mathrm{C}}^4 (E - \varepsilon_{\mathrm{C}} + 0.15 + \Delta\varepsilon) + (-1)^1 t_{\mathrm{C}}^4 (E - \varepsilon_{\mathrm{C}} + 0.15 - \Delta\varepsilon) \\ & + (-1)^0 t_{\mathrm{C}}^4 (E - \varepsilon_{\mathrm{C}} + 0.15) \,, \end{aligned} \tag{4.33}$$

where $\Delta\varepsilon = \Delta\varepsilon_4 = -\Delta\varepsilon_6$. This equation becomes zero for $E = \varepsilon_{\mathrm{C}} - 0.15$

$$M_{13}(\varepsilon_{\mathrm{C}} - 0.15) = (-1)^1 t^4 \Delta\varepsilon + (-1)^1 t^4 \,(-\Delta\varepsilon) = 0 \,. \tag{4.34}$$

We see that within a Hückel model, where the bias voltage is considered by shifting the onsite energy accordingly, the GAOS predicts DQI also in non-equilibrium. We also see that the effective energy shift discussed in Sec. 4.4.3 results in DQI being shifted towards lower energies within the GAOS.

4.5.3 TC_{π}^{SO} model

Now we calculate the transmission of the model systems taking advantage of the knowledge we gained up to now. While the hopping parameters are also influenced by the bias voltage, we know from Secs. 4.4.2 and 4.5.1 that the influence is small in comparison to the energy shift of the onsite energies. Furthermore, it shows that the inclusion of the influence of the bias voltage on the hopping parameter without also improving the description of the effective d orbitals does not improve the agreement of the model results and first-principles results. Therefore we use the same parameters for modeling the electrodes as in equilibrium, except for the onsite energy of the effective d orbitals. We shift the onsite energy of the d orbitals according to

$$\varepsilon_{\mathrm{d,j}}^{\mathrm{U_B}} = \varepsilon_{\mathrm{d,j}}^{\mathrm{U_B}=0V} + \Delta\varepsilon_{\mathrm{d,j}} \,, \tag{4.35}$$

where $\mathrm{j} \in \{\mathrm{L}, \mathrm{R}\}$. We set $\varepsilon_{\mathrm{d,j}}^{\mathrm{U_B}=0V} = -4$ (see Sec. 4.3.1) and take the energy shift $\Delta\varepsilon_{\mathrm{d,j}}$ of the effective d orbitals to have the same value as the energy shift of the gold atoms at the electrode surfaces in Fig. 4.19. Tab. 4.7 contains the energy shifts of the d orbitals we use in the model calculations.

Tab. 4.7. Energy shift $\Delta\varepsilon_{\mathrm{d,j}}$ of the surface orbitals of the left (j = L) and right (j = R) electrode entering the TC_{π}^{SO} model.

(a) meta-BDT

U_B / V	$\Delta\varepsilon_{d,L}$ / eV	$\Delta\varepsilon_{d,R}$ / eV
0	0.00	0.00
1	0.49	-0.49
3	1.44	-1.45

(b) para-BDT

U_B / V	$\Delta\varepsilon_{d,L}$ / eV	$\Delta\varepsilon_{d,R}$ / eV
0	0.00	0.00
1	0.48	-0.48
3	1.38	-1.44

We reduce the TRANSIESTA Hamiltonian matrices of the BDT+planar systems to TC_{π}^{SO} Hamiltonian matrices using the procedure from Sec. 3.2.2.3. The resulting Hamiltonian matrices rounded off to the second decimal are given in appendix E. The results of the DFT calculations and the model calculations agree better in the case of not rounding off the Hamiltonian matrices. Therefore we do not round off the Hamiltonian matrices in the following calculations. Fig. 4.23 shows the transmission curves of the model systems. The energies at which DQI occurs are summarized in Tab. 4.8. By comparing Figs. 4.16 and 4.23 we see that the simple TC_{π}^{SO} model reproduces the trends of the first-principles calculations. The model shows that the effective energy shift of the benzene rings we observe in Fig. 4.19 results in the DQI shifting towards lower energies.

We see in Tab. 4.8 that the DQI is shifted towards lower energies in the same way the onsite energies of the carbon atoms are. Using the results of Tab. 4.8 we calculate by how many eV the DQI of the meta-BDT+planar system in non-equilibrium is shifted relative to the DQI of this system in equilibrium. We compare in Tab. 4.9 the shift of the DQI in the TC_{π}^{SO} model to the effective energy shifts of the benzene ring from Sec. 4.4.3. We see that the shift of the DQI is in good agreement with the effective shift of the benzene ring.

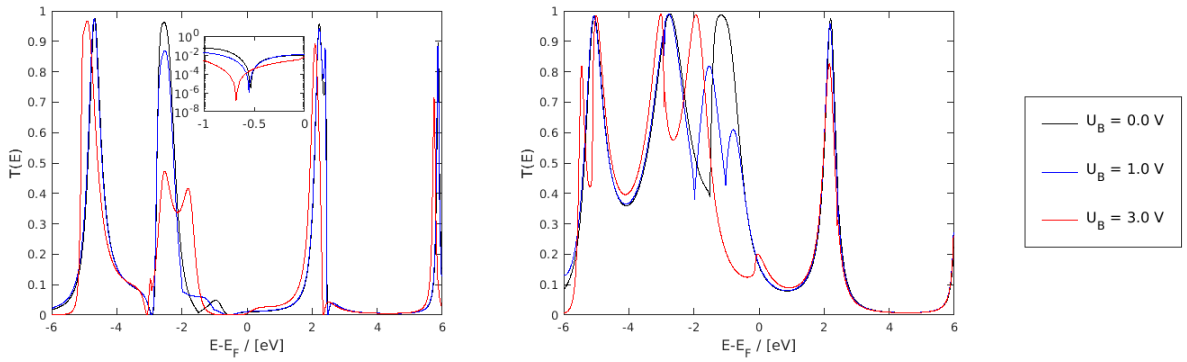

Fig. 4.23. Transmission of meta-BDT (left) and para-BDT (right) for an energy resolution of $\Delta E = 0.005$. The simple $\mathrm{TC}_{\pi}^{\mathrm{SO}}$ model reproduces the trends we observe in Fig. 4.16. The model also shows that, due to the effective energy shift of the benzene rings we observe in Fig. 4.19, DQI is shifted towards lower energies.

Tab. 4.8. Energies at which DQI occurs in Fig. 4.23 (inlay plot).

$\mathrm{U_B}$ / V	$E - E_{\mathrm{F}}$ / eV
0	-0.535
1	-0.550
3	-0.680

Tab. 4.9. Comparison of the shift of the DQI and the average energy shift of the benzene ring $\Delta\varepsilon_{\mathrm{eff}}$. We take $\Delta\varepsilon_{\mathrm{eff}}$ to be the change of the onsite energies of the carbon atoms of the meta-BDT+planar system at sites 2 and 5 with respect to the bias voltage. The energy at which DQI occurs is shifted by about the same amount the onsite energies of the benzene ring are effectively shifted.

$\mathrm{U_B}$ / V	$E - E_{\mathrm{F}} + 0.535$ / eV	$\Delta\varepsilon_{\mathrm{eff}}$ / eV
0	-0.000	-0.000
1	-0.015	-0.011
3	-0.145	-0.151

Chapter 5

Conclusion

In this work we studied destructive quantum interference (DQI) upon benzenedithiolate using a density functional theory and non-equilibrium Green's function (DFT+NEGF) approach. We contacted benzene-1,3-dithiolate (meta-BDT) and benzene-1,4-dithiolate (para-BDT) to Au(111) electrodes to study, how contacting different sites of a benzene ring influences the transmission of the transport systems. We contacted meta-BDT and para-BDT to planar and to pointed electrodes to study also the impact of the electrode shape on the transmission.

Firstly, we studied in Sec. 4.1 benzene and benzenedithiolate within a simple Hückel model with parameters taken from literature. In Sec. 4.1.1 we studied the pristine molecules. We broadened the energy levels of the molecules artificially to study the impact of level broadening at sites other than the ones coupled to the electrodes, e.g. due to the molecule lying on a substrate. Exact DQI is no longer observable, while in the case of meta-BDT DQI also appears to have shifted to higher energies. We studied benzene and BDT being contacted to electrodes modeled in the wide-band limit in Sec. 4.1.2. By contacting benzene at meta-position states are induced around the Fermi energy at various carbon sites but not at the carbon sites contacted to the electrodes. Likewise meta-BDT has no states around the Fermi energy at the carbon sites contacted to the sulfur atoms. Contacting benzene at para-position and para-BDT induced states around the Fermi energy at every carbon site. We observe that DQI in meta-benzene and meta-BDT is accompanied by the absence of states around the Fermi energy at sites contacted to the electrodes and the sulfur atoms, respectively.

We calculated in Sec. 4.2 the transmission and the PDOS of the different systems in equilibrium using a DFT+NEGF approach. In Sec. 4.2.1 we relaxed the geometry of the systems. We observed in Sec. 4.2.2, that the transmission of meta-BDT around the Fermi energy is lower than the transmission of the para-BDT, but the transmisson of meta-BDT neither vanishes nor has its minimum at the Fermi energy. We also found that the transmission in the case of meta-BDT being contacted to planar electrodes is about 5 times the transmission of it being contacted to pointed electrodes. In Sec. 4.2.2.1 we split the transmission into contributions from a p-channel and a r-channel, where the former channel is supposed to display DQI while the latter is not. The p-channel contains the basis functions of the TranSIESTA calculations describing the p_z orbitals of the carbon and sulfur atoms, and the r-channel contains the basis functions describing the remaining orbitals of the BDT molecule. In the case of planar electrodes the transport of the meta-BDT is dominated by the r-channel, while the transport of para-BDT is dominated by the p-channel. We observed that the transmission of the p-channel of the meta-BDT contacted to planar electrodes has a small but finite transmission around the Fermi energy.

In Sec. 4.3 we mapped the first-principles calculations of the meta-BDT and para-BDT contacted to planar electrodes onto various models with different degrees of approximation. In Sec. 4.3.1 we showed that the planar electrodes can be modeled in terms of simple analytic functions, while the PDOS of the pointed electrodes displays too much structure for doing so. In Sec. 4.3.2 we observed that part of the transmission of the p-channel arises from the electrodes coupling not just to the sulfur atoms but to further atoms of the BDT molecule. Therefore exact DQI is only observable in the case that one considers only the p-channel and enforces the electrodes to couple only to the sulfur atoms. We saw that the π-electron approximation, within which only electrons in the p_z orbitals of the carbon and sulfur atoms are treated explicitly and the remaining electrons of the BDT solely as an contribution to the potential, is a reasonably good approximation in the case of para-BDT contacted to planar electrodes. In the case of meta-BDT contacted to planar electrodes, DQI is predicted at slightly lower energies within the π-electron approximation and thereby changes the transmission of several transmission peaks considerably. We also observed in Sec. 4.3.3 that by further simplifying the model to a Hückel one, DQI is predicted at slightly higher energies, resulting in a quite good prediction of the energy at which DQI is observed. The Hückel model shows once more that by coupling the electrodes only to the sulfur atoms we do not fully support the p-channel. Aside from the unsupported contributions of the p-channel, the results of the Hückel model and the first-principles calculations are in good agreement.

Finally, in Sec. 4.4 we drove the four systems out of equilibrium by applying various bias voltages to the transport systems. In Sec. 4.4.1 we saw that the influence of the bias voltage on the transmission of the systems depends considerably on the PDOS of the electrodes. The transmission of each system changes considerably in the energy range, in which the PDOS of the electrodes is strongly energy-dependent. We also observed that the energy shift of the carbon atoms induced by the bias voltage corresponds to a fraction of this bias voltage indicating that part of the voltage drop occurs at the electrodes. Therefore we studied the influence of the bias voltage on the Hamiltonian matrices of the systems in Sec. 4.4.2. The bias voltage changes the diagonal elements of the Hamiltonian matrices considerably, while the off-diagonal terms are less influenced. We calculated the energy shift of the onsite energies in Sec. 4.4.3 and observed, that only part of the bias voltage drops at the benzene ring. On average the benzene rings are shifted towards lower energies, especially when contacted to pointed electrodes, which is a consequence of the systems not being perfectly symmetric. In Sec. 4.4.4 we studied the behavior of the PDOS of the benzene rings in non-equilibrium in more detail. Except for para-BDT being contacted to pointed electrodes, the PDOS of the systems are in qualitative agreement with the PDOS from the Hückel model in Sec. 4.1.2. Also in non-equilibrium, the benzene rings of the meta-BDT molecules have close to no states around the Fermi energy at the carbon sites next to the sulfur atoms, while para-BDT has a large number of states at this sites around the Fermi energy. In Sec. 4.4.5 we dealt with the current-voltage characteristics of the systems. The current across the para-BDT molecule is higher than across the meta-BDT molecule. In the case of planar electrodes the current ratio $\frac{I_{\text{Meta}}}{I_{\text{Para}}}$ is larger than in the case of pointed electrodes. In Sec. 4.4.5 we also saw that meta-BDT contacted to pointed electrodes displays a negative differential conductivity.

In Sec. 4.5 we mapped the first-principles calculations in non-equilibrium onto the same models as we did in equilibrium. In Sec. 4.5.1 we analyzed to which extent the bias voltage changes the model parameters. Like in the first-principles calculations, the influence on the off-diagonal elements is small compared to the influence on the diagonal elements. By considering the energy shifts from Sec. 4.5.1 we showed in Sec. 4.5.2, that DQI is also predicted in non-equilibrium, with DQI being shifted towards lower energies by the same amount the benzene ring is effectively shifted towards lower energies.

Appendix A

Degrees of approximations within the different models

Tight Coupling (TC)

We split the central region of the transport systems into the clusters $\mathbf{C}_\mathrm{L}$, BDT and $\mathbf{C}_\mathrm{R}$ as we have discussed in Sec. 3.2.2.1. We enforce "tight coupling" by setting all elements of the coupling matrices $\mathbf{V}_{\mathrm{j,BDT}}$ and $\mathbf{V}_{\mathrm{BDT,j}}$ with $\mathrm{j} \in \{\mathrm{C_L}, \mathrm{C_R}\}$ to zero, which do not correspond to hopping processes between the electrodes and the nearest-neighbor sulfur atoms. Similarly, we set all elements of the overlap matrices $\mathbf{s}_{\mathrm{j,BDT}}$ and $\mathbf{s}_{\mathrm{BDT,j}}$ to zero, which do not correspond to overlap elements of the electrodes and nearest-neighbor sulfur atoms. We label the resulting coupling and overlap matrices with the superscript TC. We calculate the matrix Green's function and the transmission of the TC model from

$$\mathbf{G}_\mathrm{TC}(E) = \left[E\mathbf{S}_\mathrm{BDT} - \mathbf{H}_\mathrm{BDT} - \mathbf{\Sigma}^\mathrm{TC}_\mathrm{C_L} - \mathbf{\Sigma}^\mathrm{TC}_\mathrm{C_R}\right]^{-1} \tag{A.1}$$

$$\mathrm{T}^\mathrm{TC}(E) = \mathrm{Tr}\left((\mathbf{G}_\mathrm{TC})^\dagger \mathbf{\Gamma}^\mathrm{C_R}_\mathrm{TC} \mathbf{G}_\mathrm{TC} \mathbf{\Gamma}^\mathrm{C_L}_\mathrm{TC}\right) \tag{A.2}$$

with

$$\mathbf{\Gamma}^\mathrm{j}_\mathrm{TC} = i\left(\mathbf{\Sigma}^\mathrm{TC}_\mathrm{j} - \left(\mathbf{\Sigma}^\mathrm{TC}_\mathrm{j}\right)^\dagger\right) = i\left(\mathbf{V}^\mathrm{TC}_\mathrm{BDT,j}\mathbf{G}_\mathrm{j}\mathbf{V}^\mathrm{TC}_\mathrm{j,BDT} - \left(\mathbf{V}^\mathrm{TC}_\mathrm{BDT,j}\mathbf{G}_\mathrm{j}\mathbf{V}^\mathrm{TC}_\mathrm{j,BDT}\right)^\dagger\right) , \tag{A.3}$$

where we used the notation (2.102). $\mathbf{G}_\mathrm{j}$ is the matrix Green's function (3.3).

Tight Coupling + π-electron approximation (TC_π)

The d orbitals (polarization orbitals) of the BDT are several eV higher in energy than the $\mathrm{p_z}$ orbitals and therefore we expect the contribution from these d orbitals to be negligible. Additionally, the $\mathrm{p_z}$ orbitals of the BDT can be treated decoupled from the s, $\mathrm{p_x}$ and $\mathrm{p_y}$ orbitals according to the π-electron approximation [15]. Therefore we set entries of the Hamiltonian matrix $\mathbf{H}_\mathrm{BDT}$ and of the overlap matrix $\mathbf{S}_\mathrm{BDT}$ as well as of the hybridization matrices $\mathbf{\Sigma}^\mathrm{TC}_\mathrm{j}$, corresponding to hopping between $\mathrm{p_z}$ orbitals and other orbitals to zero. We label the resulting Hamiltonian matrix, overlap matrix and hybridization matrices as $\mathbf{H}_{\mathrm{TC}_\pi}$, $\mathbf{S}_{\mathrm{TC}_\pi}$ and $\mathbf{\Sigma}^{\mathrm{TC}_\pi}_\mathrm{j}$, respectively. We calculate the matrix Green's function and transmission of the TC_π model from

$$\mathbf{G}_{\mathrm{TC}_\pi}(E) = \left[E\mathbf{S}_{\mathrm{TC}_\pi} - \mathbf{H}_{\mathrm{TC}_\pi} - \mathbf{\Sigma}^{\mathrm{TC}_\pi}_\mathrm{C_L} - \mathbf{\Sigma}^{\mathrm{TC}_\pi}_\mathrm{C_R}\right]^{-1} \tag{A.4}$$

$$\mathrm{T}^{\mathrm{TC}_\pi}(E) = \mathrm{Tr}\left((\mathbf{G}_{\mathrm{TC}_\pi})^\dagger \mathbf{\Gamma}^{\mathrm{C_R}}_{\mathrm{TC}_\pi} \mathbf{G}_{\mathrm{TC}_\pi} \mathbf{\Gamma}^{\mathrm{C_L}}_{\mathrm{TC}_\pi}\right) , \tag{A.5}$$

where the level-width functions $\mathbf{\Gamma}^{\mathrm{j}}_{\mathrm{TC}_\pi}$ are calculated from the hybridization matrices $\mathbf{\Sigma}^{\mathrm{TC}_\pi}_{\mathrm{j}}$.

Tight Coupling + π-electron approximation + effective single orbital ($\mathrm{TC}^{\mathrm{SO}}_{\boldsymbol{\pi}}$)

We reduce the Hamiltonian matrices and overlap matrices from the first-principles calculations using the procedure discussed in Sec. 3.2.2.3. We label the matrices resulting from this procedure as $\mathbf{H}_{\mathrm{TC}^{\mathrm{SO}}_\pi}$ and $\mathbf{S}_{\mathrm{TC}^{\mathrm{SO}}_\pi}$. We calculate the matrix Green's function and transmission of the $\mathrm{TC}^{\mathrm{SO}}_{\boldsymbol{\pi}}$ model from

$$\tilde{\mathbf{G}}_{\mathrm{TC}^{\mathrm{SO}}_\pi}(E) = \left[E\mathbf{I} - \tilde{\mathbf{H}}_{\mathrm{TC}^{\mathrm{SO}}_\pi} - \tilde{\mathbf{\Sigma}}^{\mathrm{TC}^{\mathrm{SO}}_\pi}_{\mathrm{C_L}} - \tilde{\mathbf{\Sigma}}^{\mathrm{TC}^{\mathrm{SO}}_\pi}_{\mathrm{C_R}}\right]^{-1} \tag{A.6}$$

$$\mathrm{T}^{\mathrm{TC}^{\mathrm{SO}}_\pi}(E) = \mathrm{Tr}\left((\tilde{\mathbf{G}}_{\mathrm{TC}^{\mathrm{SO}}_\pi})^\dagger \tilde{\Gamma}^{\mathrm{C_R}}_{\mathrm{TC}^{\mathrm{SO}}_\pi} \tilde{\mathbf{G}}_{\mathrm{TC}^{\mathrm{SO}}_\pi} \tilde{\Gamma}^{\mathrm{C_L}}_{\mathrm{TC}^{\mathrm{SO}}_\pi}\right) , \tag{A.7}$$

where the tilde denotes the orthonormality of the basis functions. The entries of the hybridization matrices are described by Eq. (3.10). We calculate the level-width functions from

$$\tilde{\Gamma}^{\mathrm{j}}_{\mathrm{TC}^{\mathrm{SO}}_\pi} = i\left(\tilde{\mathbf{\Sigma}}^{\mathrm{TC}^{\mathrm{SO}}_\pi}_{\mathrm{j}} - \left(\tilde{\mathbf{\Sigma}}^{\mathrm{TC}^{\mathrm{SO}}_\pi}_{\mathrm{j}}\right)^\dagger\right) . \tag{A.8}$$

Tight-binding (TB)

We reduce the Hamiltonian matrix $\tilde{\mathbf{H}}_{\mathrm{TC}^{\mathrm{SO}}_\pi}$ to a tight-binding one by setting all hopping elements of $\tilde{\mathbf{H}}_{\mathrm{TC}^{\mathrm{SO}}_\pi}$ to zero, which do not correspond to nearest-neighboring ones. We calculate the matrix Green's function and transmission of the TB model from

$$\tilde{\mathbf{G}}_{\mathrm{TB}}(E) = \left[E\mathbf{I} - \tilde{\mathbf{H}}_{\mathrm{TB}} - \tilde{\mathbf{\Sigma}}^{\mathrm{TC}^{\mathrm{SO}}_\pi}_{\mathrm{C_L}} - \tilde{\mathbf{\Sigma}}^{\mathrm{TC}^{\mathrm{SO}}_\pi}_{\mathrm{C_R}}\right]^{-1} \tag{A.9}$$

$$\mathrm{T}^{\mathrm{TB}}(E) = \mathrm{Tr}\left((\tilde{\mathbf{G}}_{\mathrm{TB}})^\dagger \tilde{\Gamma}^{\mathrm{C_R}}_{\mathrm{TC}^{\mathrm{SO}}_\pi} \tilde{\mathbf{G}}_{\mathrm{TB}} \tilde{\Gamma}^{\mathrm{C_L}}_{\mathrm{TC}^{\mathrm{SO}}_\pi}\right) . \tag{A.10}$$

Hückel

We describe only the benzene ring of the BDT by a Hückel model (see Eq. (4.1)). We reduce the number of parameters from the TB Hamiltonian matrix to a total of four: the average of the onsite energies of the sulfur atoms ε_{S}, the average of the onsite energies of the carbon atoms ε_{C}, the average of the hopping elements describing hopping between nearest-neighboring carbon atoms t_{C} and the hopping elements describing hopping between nearest-neighboring carbon and sulfur atoms t_{SC}. We calculate the matrix Green's function and transmission of the Hückel model from

$$\tilde{\mathbf{G}}_{\mathrm{Hückel}}(E) = \left[E\mathbf{I} - \tilde{\mathbf{H}}_{\mathrm{Hückel}} - \tilde{\mathbf{\Sigma}}^{\mathrm{TC}^{\mathrm{SO}}_\pi}_{\mathrm{C_L}} - \tilde{\mathbf{\Sigma}}^{\mathrm{TC}^{\mathrm{SO}}_\pi}_{\mathrm{C_R}}\right]^{-1} \tag{A.11}$$

$$\mathrm{T}^{\mathrm{Hückel}}(E) = \mathrm{Tr}\left((\tilde{\mathbf{G}}_{\mathrm{Hückel}})^\dagger \tilde{\Gamma}^{\mathrm{C_R}}_{\mathrm{TC}^{\mathrm{SO}}_\pi} \tilde{\mathbf{G}}_{\mathrm{Hückel}} \tilde{\Gamma}^{\mathrm{C_L}}_{\mathrm{TC}^{\mathrm{SO}}_\pi}\right) . \tag{A.12}$$

Appendix B

Hückel parameters taken from literature

We take the onsite energies, the radii of the atoms and also the formula to calculate the interatomic matrix elements (hopping parameters) from Ref. [30]. Tab. B.1 summarizes the parameters taken from Ref. [30]. The energies of the orbitals can be taken directly as the corresponding onsite energies. The hopping terms are calculated by

$$V_{ll'm} = \eta_{ll'm}\frac{\hbar^2}{m_e d^2} = \eta_{ll'm}\frac{7.62}{d^2}\ , \tag{B.1}$$

where $\eta_{ll'm}$ is a fitting parameter. m_e is the electron mass and d is the distance between the two atoms involved. For calculating the hopping parameter t_{SC} we assume that the radius of the carbon atom bound to the sulfur is $\frac{d_C}{2}$.

Tab. B.1. Parameters taken from literature.
The energies are in units of eV and the radii in units of Å

Parameter	value	additional info
ε_C	-8.97	energy of the p orbitals of carbon
ε_S	-10.27	energy of the p orbitals of sulfur
d_C	1.54	length of the covalent C-C bond (no ionic radius provided)
r_S	1.90	radius of ionic sulfur
$\eta_{pp\pi}$	-0.81	fitting parameter for two p orbitals forming a π bond
t_{SC}	-0.87	calculated using above formula
t_C	-2.60	calculated using above formula

We won't take the onsite energies of the orbitals as shown in Tab. B.1 but set the onsite energy of the carbon atoms to be at 0 eV. We do so in the following way

$$\mathbf{H}\vec{c} = E\mathbf{S}\vec{c}\ \ /\ -\varepsilon_C\mathbf{S}\vec{c}\ \ . \tag{B.2}$$

We will use these parameters within the Hückel model, which assumes an orthonormal basis. Therefore we get

$$\underbrace{(\mathbf{H} - \varepsilon_{\mathrm{C}}\mathbf{I})}_{\mathbf{H}'} \vec{c} = \underbrace{(E - \varepsilon_{\mathrm{C}})}_{E'} \vec{c} \quad . \tag{B.3}$$

The parameters of the primed Hamiltonian matrix are now

$$\begin{aligned} \varepsilon'_{\mathrm{C}} &= \quad 0 \text{ eV} \\ \varepsilon'_{\mathrm{S}} &= -1.30 \text{ eV} \\ t'_{\mathrm{C}} &= -0.87 \text{ eV} \\ t'_{\mathrm{SC}} &= -2.60 \text{ eV} , \end{aligned}$$

where we omit the prime in the main text to shorten the notation.

Appendix C

List of DFT parameters

Tab. C.1 lists the parameters, which we use in the first-principles calculations throughout this thesis. We take the pseudopotentials from Ref. [29], where a similar system to the one in Fig. 1.3c was calculated with an 3×3 gold atoms wide electrode and a lattice constant of 4.18 Å. We choose the electronic temperature to be 25 meV. We limit the basis size of the calculations in this thesis to *DZP*. A thorough analysis of the band structure of a gold bulk shows that the choice of a SZP or DZP basis describing the gold atoms does influence the results only marginally. Therefore we describe gold atoms not part of the tips by a SZP basis. We converge the number of k-points in the direction perpendicular to the transport direction with respect to the transmission. It shows that the trend of the transmission converges pretty fast, but convergence needs a considerably larger number of k-points. Therefore we consider a 4×4 k-grid to be converged. We converged the parameter *MeshCutoff* using the energy difference of the total energy and the Fermi energy from the SIESTA calculations as convergence criterion. For the remaining parameters the convergence criterion was the transmission. For further information on the parameters listed below we refer the reader to the SIESTA and TBTRANS manuals.

Tab. C.1. Parameter settings in the DFT calculations

Option / Parameter	**Value**	additional information
BasisSize	DZP	for BDT and gold tips
ElectronicTemperature	25	in units of meV (≈ 290 K)
k-points	4 × 4 × 1	used in the TRANSIESTA calculations
k-points	4 × 4 × 20	used in the electrode calculations
MeshCutoff	550	in units of Rydberg
EnergyShift	0.01	in units of Rydberg
SplitNorm	0.40	fraction of norm carried by 2nd basis function of an orbital
MD.MaxForceTol	0.04	in units of $\frac{\text{eV}}{\text{Å}}$
circle part of the contour	75	number of contour points
tail part of the contour	17	number of contour points
TS.Contours.Eq.Pole	5.5	in eV, imaginary part of tail part at the Fermi energy
E_{min}	-40	in eV, lower limit of circle part of the contour

Appendix D

Transmission through different transport channels

We split up the Hamiltonian matrix of the central region according to Sec. 3.2.2.1. We are interested in the transmission of the p_z orbitals of the carbon and sulfur atoms. Therefore we further split up the Hamiltonian matrix $\mathbf{H}_{\mathrm{BDT}}$ in Eq. (3.1)

$$\mathbf{H}_{\mathrm{C}} = \begin{pmatrix} \mathbf{H}_{\mathrm{C_L}} & \mathbf{V}_{\mathrm{C_L,BDT}} & 0 \\ \mathbf{V}_{\mathrm{BDT,C_L}} & \mathbf{H}_{\mathrm{BDT}} & \mathbf{V}_{\mathrm{BDT,C_R}} \\ 0 & \mathbf{V}_{\mathrm{C_R,BDT}} & \mathbf{H}_{\mathrm{C_R}} \end{pmatrix} = \begin{pmatrix} \mathbf{H}_{\mathrm{C_L}} & \mathbf{V}_{\mathrm{C_L,p}} & \mathbf{V}_{\mathrm{C_L,r}} & 0 \\ \mathbf{V}_{\mathrm{p,C_L}} & \mathbf{H}_{\mathrm{p}} & \mathbf{V}_{\mathrm{pr}} & \mathbf{V}_{\mathrm{p,C_R}} \\ \mathbf{V}_{\mathrm{r,C_L}} & \mathbf{V}_{\mathrm{rp}} & \mathbf{H}_{\mathrm{r}} & \mathbf{V}_{\mathrm{r,C_R}} \\ 0 & \mathbf{V}_{\mathrm{C_R,p}} & \mathbf{V}_{\mathrm{C_R,r}} & \mathbf{H}_{\mathrm{C_R}} \end{pmatrix}, \quad \text{(D.1)}$$

where the gray areas mark the same submatrices. $\mathbf{H}_{\mathrm{p}}$ is the Hamiltonian matrix of the p-channel, while $\mathbf{H}_{\mathrm{r}}$ is the Hamiltonian matrix of the r-channel. We split up the overlap matrix $\mathbf{S}_{\mathrm{C}}$ in the exact same way.

We treat the clusters $\mathrm{C_L}$ and $\mathrm{C_R}$ as discussed in Sec. 3.2.2.1. We use the notation (2.102) and calculate the hybridization matrices of Eq. (D.1) according to Eqs (2.56) and (2.57)

$$\mathbf{\Sigma}_{\mathrm{j}} = \begin{pmatrix} \mathbf{V}_{\mathrm{pj}}\mathbf{G}_{\mathrm{j}}\mathbf{V}_{\mathrm{jp}} & \mathbf{V}_{\mathrm{pj}}\mathbf{G}_{\mathrm{j}}\mathbf{V}_{\mathrm{jr}} \\ \mathbf{V}_{\mathrm{rj}}\mathbf{G}_{\mathrm{j}}\mathbf{V}_{\mathrm{jp}} & \mathbf{V}_{\mathrm{rj}}\mathbf{G}_{\mathrm{j}}\mathbf{V}_{\mathrm{jr}} \end{pmatrix} = \begin{pmatrix} \mathbf{\Sigma}_{\mathrm{j}}^{\mathrm{pp}} & \mathbf{\Sigma}_{\mathrm{j}}^{\mathrm{pr}} \\ \mathbf{\Sigma}_{\mathrm{j}}^{\mathrm{rp}} & \mathbf{\Sigma}_{\mathrm{j}}^{\mathrm{rr}} \end{pmatrix} \quad \text{(D.2)}$$

with $\mathrm{j} \in \{\mathrm{C_L}, \mathrm{C_R}\}$. We calculate the matrix Green's function $\mathbf{G}^{\mathrm{BDT}}$ from

$$\mathbf{G}^{\mathrm{BDT}} = \left[E^{+}\mathbf{S}_{\mathrm{BDT}} - \mathbf{H}_{\mathrm{BDT}} - \mathbf{\Sigma}_{\mathrm{C_L}} - \mathbf{\Sigma}_{\mathrm{C_R}}\right]^{-1}, \quad \text{(D.3)}$$

where $\mathbf{G}^{\mathrm{BDT}}$ has now the form

$$\mathbf{G}^{\mathrm{BDT}} = \begin{pmatrix} \mathbf{G}_{\mathrm{p}} & \mathbf{G}_{\mathrm{pr}} \\ \mathbf{G}_{\mathrm{rp}} & \mathbf{G}_{\mathrm{r}} \end{pmatrix}. \quad \text{(D.4)}$$

We calculate the level-width functions from Eq. (D.2) and split them up into

$$\mathbf{\Gamma}_{\mathrm{j}} = i\left(\mathbf{\Sigma}_{\mathrm{j}} - \mathbf{\Sigma}_{\mathrm{j}}^{\dagger}\right) = \underbrace{\begin{pmatrix} \mathbf{\Gamma}_{\mathrm{j}}^{\mathrm{pp}} & \mathbf{0} \\ \mathbf{0} & \mathbf{0} \end{pmatrix}}_{\mathbf{\Gamma}_{\mathrm{j}}^{\mathrm{p}}} + \underbrace{\begin{pmatrix} \mathbf{0} & \mathbf{0} \\ \mathbf{0} & \mathbf{\Gamma}_{\mathrm{j}}^{\mathrm{rr}} \end{pmatrix}}_{\mathbf{\Gamma}_{\mathrm{j}}^{\mathrm{r}}} + \underbrace{\begin{pmatrix} \mathbf{0} & \mathbf{\Gamma}_{\mathrm{j}}^{\mathrm{pr}} \\ \mathbf{\Gamma}_{\mathrm{j}}^{\mathrm{rp}} & \mathbf{0} \end{pmatrix}}_{\mathbf{\Gamma}_{\mathrm{j}}^{\mathrm{int}}} . \tag{D.5}$$

Now we calculate the transmission using Eq. (D.5) and get

$$\begin{aligned} \mathrm{T}(E) &= \mathrm{Tr}\left(\left(\mathbf{G}^{\mathrm{BDT}}\right)^{\dagger}\mathbf{\Gamma}_{\mathrm{C_R}}\mathbf{G}^{\mathrm{BDT}}\mathbf{\Gamma}_{\mathrm{C_L}}\right) \\ &= \mathrm{Tr}\Big(\left(\mathbf{G}^{\mathrm{BDT}}\right)^{\dagger}\mathbf{\Gamma}^{\mathrm{p}}_{\mathrm{C_R}}\mathbf{G}^{\mathrm{BDT}}\mathbf{\Gamma}^{\mathrm{p}}_{\mathrm{C_L}} + \left(\mathbf{G}^{\mathrm{BDT}}\right)^{\dagger}\mathbf{\Gamma}^{\mathrm{p}}_{\mathrm{C_R}}\mathbf{G}^{\mathrm{BDT}}\mathbf{\Gamma}^{\mathrm{r}}_{\mathrm{C_L}} + \left(\mathbf{G}^{\mathrm{BDT}}\right)^{\dagger}\mathbf{\Gamma}^{\mathrm{p}}_{\mathrm{C_R}}\mathbf{G}^{\mathrm{BDT}}\mathbf{\Gamma}^{\mathrm{int}}_{\mathrm{C_L}} \\ &\quad + \left(\mathbf{G}^{\mathrm{BDT}}\right)^{\dagger}\mathbf{\Gamma}^{\mathrm{r}}_{\mathrm{C_R}}\mathbf{G}^{\mathrm{BDT}}\mathbf{\Gamma}^{\mathrm{p}}_{\mathrm{C_L}} + \left(\mathbf{G}^{\mathrm{BDT}}\right)^{\dagger}\mathbf{\Gamma}^{\mathrm{r}}_{\mathrm{C_R}}\mathbf{G}^{\mathrm{BDT}}\mathbf{\Gamma}^{\mathrm{r}}_{\mathrm{C_L}} + \left(\mathbf{G}^{\mathrm{BDT}}\right)^{\dagger}\mathbf{\Gamma}^{\mathrm{r}}_{\mathrm{C_R}}\mathbf{G}^{\mathrm{BDT}}\mathbf{\Gamma}^{\mathrm{int}}_{\mathrm{C_L}} \\ &\quad + \left(\mathbf{G}^{\mathrm{BDT}}\right)^{\dagger}\mathbf{\Gamma}^{\mathrm{int}}_{\mathrm{C_R}}\mathbf{G}^{\mathrm{BDT}}\mathbf{\Gamma}^{\mathrm{p}}_{\mathrm{C_L}} + \left(\mathbf{G}^{\mathrm{BDT}}\right)^{\dagger}\mathbf{\Gamma}^{\mathrm{int}}_{\mathrm{C_R}}\mathbf{G}^{\mathrm{BDT}}\mathbf{\Gamma}^{\mathrm{r}}_{\mathrm{C_L}} + \left(\mathbf{G}^{\mathrm{BDT}}\right)^{\dagger}\mathbf{\Gamma}^{\mathrm{int}}_{\mathrm{C_R}}\mathbf{G}^{\mathrm{BDT}}\mathbf{\Gamma}^{\mathrm{int}}_{\mathrm{C_L}}\Big) . \end{aligned} \tag{D.6}$$

We take advantage of the following property of the trace

$$\mathrm{Tr}\left(\mathbf{A}+\mathbf{B}\right) = \mathrm{Tr}\left(\mathbf{A}\right) + \mathrm{Tr}\left(\mathbf{B}\right) \tag{D.7}$$

and rewrite the transmission

$$\begin{aligned} \mathrm{T}(E) &= \mathrm{Tr}\left(\left(\mathbf{G}^{\mathrm{BDT}}\right)^{\dagger}\mathbf{\Gamma}^{\mathrm{p}}_{\mathrm{C_R}}\mathbf{G}^{\mathrm{BDT}}\mathbf{\Gamma}^{\mathrm{p}}_{\mathrm{C_L}}\right) + \mathrm{Tr}\left(\left(\mathbf{G}^{\mathrm{BDT}}\right)^{\dagger}\mathbf{\Gamma}^{\mathrm{r}}_{\mathrm{C_R}}\mathbf{G}^{\mathrm{BDT}}\mathbf{\Gamma}^{\mathrm{r}}_{\mathrm{C_L}}\right) \\ &\quad + \mathrm{Tr}\Big(\left(\mathbf{G}^{\mathrm{BDT}}\right)^{\dagger}\mathbf{\Gamma}^{\mathrm{p}}_{\mathrm{C_R}}\mathbf{G}^{\mathrm{BDT}}\mathbf{\Gamma}^{\mathrm{r}}_{\mathrm{C_L}} + \left(\mathbf{G}^{\mathrm{BDT}}\right)^{\dagger}\mathbf{\Gamma}^{\mathrm{p}}_{\mathrm{C_R}}\mathbf{G}^{\mathrm{BDT}}\mathbf{\Gamma}^{\mathrm{int}}_{\mathrm{C_L}} + \left(\mathbf{G}^{\mathrm{BDT}}\right)^{\dagger}\mathbf{\Gamma}^{\mathrm{r}}_{\mathrm{C_R}}\mathbf{G}^{\mathrm{BDT}}\mathbf{\Gamma}^{\mathrm{p}}_{\mathrm{C_L}} \\ &\quad + \left(\mathbf{G}^{\mathrm{BDT}}\right)^{\dagger}\mathbf{\Gamma}^{\mathrm{r}}_{\mathrm{C_R}}\mathbf{G}^{\mathrm{BDT}}\mathbf{\Gamma}^{\mathrm{int}}_{\mathrm{C_L}} + \left(\mathbf{G}^{\mathrm{BDT}}\right)^{\dagger}\mathbf{\Gamma}^{\mathrm{int}}_{\mathrm{C_R}}\mathbf{G}^{\mathrm{BDT}}\mathbf{\Gamma}^{\mathrm{p}}_{\mathrm{C_L}} + \left(\mathbf{G}^{\mathrm{BDT}}\right)^{\dagger}\mathbf{\Gamma}^{\mathrm{int}}_{\mathrm{C_R}}\mathbf{G}^{\mathrm{BDT}}\mathbf{\Gamma}^{\mathrm{r}}_{\mathrm{C_L}} \\ &\quad + \left(\mathbf{G}^{\mathrm{BDT}}\right)^{\dagger}\mathbf{\Gamma}^{\mathrm{int}}_{\mathrm{C_R}}\mathbf{G}^{\mathrm{BDT}}\mathbf{\Gamma}^{\mathrm{int}}_{\mathrm{C_L}}\Big) . \end{aligned} \tag{D.8}$$

We evaluate the first and second trace in Eq. (D.8) using Eq. (D.4) and get

$$\mathrm{Tr}\left(\left(\mathbf{G}^{\mathrm{BDT}}\right)^{\dagger}\mathbf{\Gamma}^{\mathrm{p}}_{\mathrm{C_R}}\left(\mathbf{G}^{\mathrm{BDT}}\right)\mathbf{\Gamma}^{\mathrm{p}}_{\mathrm{C_L}}\right) = \mathrm{Tr}\left(\mathbf{G}_{\mathrm{p}}^{\dagger}\mathbf{\Gamma}^{\mathrm{pp}}_{\mathrm{C_R}}\mathbf{G}_{\mathrm{p}}\mathbf{\Gamma}^{\mathrm{pp}}_{\mathrm{C_L}}\right) = \mathrm{T_p}(E) \tag{D.9}$$

$$\mathrm{Tr}\left(\left(\mathbf{G}^{\mathrm{BDT}}\right)^{\dagger}\mathbf{\Gamma}^{\mathrm{r}}_{\mathrm{C_R}}\left(\mathbf{G}^{\mathrm{BDT}}\right)\mathbf{\Gamma}^{\mathrm{r}}_{\mathrm{C_L}}\right) = \mathrm{Tr}\left(\mathbf{G}_{\mathrm{r}}^{\dagger}\mathbf{\Gamma}^{\mathrm{rr}}_{\mathrm{C_R}}\mathbf{G}_{\mathrm{r}}\mathbf{\Gamma}^{\mathrm{rr}}_{\mathrm{C_L}}\right) = \mathrm{T_r}(E) \ , \tag{D.10}$$

where we identify the first trace as the transmission across the $\mathrm{p_z}$ orbitals of the carbon and sulfur atoms and the second trace as the transmission across the remaining orbitals. Therefore we write the transmission as

$$\mathrm{T}(E) = \mathrm{T_p}(E) + \mathrm{T_r}(E) + \mathrm{T_{int}}(E) \ , \tag{D.11}$$

where $\mathrm{T_{int}}(E)$ is an interference term containing all the remaining terms from Eq. (D.8).

Appendix E

Model Hamiltonian matrices

We consider only the BDT+planar systems as discussed in Sec. 4.3.1. Below, we give the Hamiltonian matrices we gained by applying the procedure described in Sec. 3.2.2.3 to the Hamiltonian matrices resulting from the TRANSIESTA calculations. The blue highlighted parts of the matrices describe the sulfur sites, the red highlighted parts describe the benzene ring, the green highlighted parts describe the hopping of the electrons between the sulfur atoms and the benzene ring, while the yellow highlighted parts describe the hopping of the electrons between the sulfur atoms with one another. The order of the carbon atoms is chosen according to Sec. 2.6.2 with the sulfur atoms being the nearest-neighbors of the starred carbon atoms.

Matrices of the meta-BDT

$$H_{\text{Meta}}^{\text{U}_\text{B}=0V} = \begin{pmatrix} -2.23 & -1.58 & -0.04 & 0.06 & 0.02 & -0.00 & 0.15 & -0.01 \\ -1.58 & -0.26 & -2.54 & 0.09 & -0.26 & 0.27 & -2.23 & 0.06 \\ -0.04 & -2.54 & 0.26 & -2.59 & 0.31 & -0.15 & 0.33 & -0.03 \\ 0.06 & 0.09 & -2.59 & -0.20 & -2.25 & 0.30 & -0.25 & -1.59 \\ 0.02 & -0.26 & 0.31 & -2.25 & 0.16 & -2.60 & 0.15 & 0.16 \\ -0.00 & 0.27 & -0.15 & 0.30 & -2.60 & 0.42 & -2.65 & -0.01 \\ 0.15 & -2.23 & 0.33 & -0.25 & 0.15 & -2.65 & 0.17 & 0.02 \\ -0.01 & 0.06 & -0.03 & -1.59 & 0.16 & -0.01 & 0.02 & -2.21 \end{pmatrix} \tag{E.1}$$

$$H_{\text{Meta}}^{\text{U}_\text{B}=1V} = \begin{pmatrix} -1.83 & -1.58 & -0.04 & 0.06 & 0.02 & -0.00 & 0.16 & -0.01 \\ -1.58 & -0.13 & -2.54 & 0.09 & -0.26 & 0.27 & -2.23 & 0.06 \\ -0.04 & -2.54 & 0.25 & -2.59 & 0.31 & -0.15 & 0.32 & -0.03 \\ 0.06 & 0.09 & -2.59 & -0.35 & -2.25 & 0.30 & -0.25 & -1.59 \\ 0.02 & -0.26 & 0.31 & -2.25 & 0.06 & -2.60 & 0.15 & 0.16 \\ -0.00 & 0.27 & -0.15 & 0.30 & -2.60 & 0.41 & -2.65 & -0.01 \\ 0.16 & -2.23 & 0.32 & -0.25 & 0.15 & -2.65 & 0.25 & 0.02 \\ -0.01 & 0.06 & -0.03 & -1.59 & 0.16 & -0.01 & 0.02 & -2.64 \end{pmatrix} \tag{E.2}$$

$$H_{\text{Meta}}^{\text{U}_\text{B}=3V} = \begin{pmatrix} -1.12 & -1.57 & -0.03 & 0.06 & 0.02 & -0.00 & 0.16 & -0.01 \\ -1.57 & 0.04 & -2.54 & 0.09 & -0.26 & 0.27 & -2.23 & 0.06 \\ -0.03 & -2.54 & 0.10 & -2.59 & 0.31 & -0.15 & 0.32 & -0.03 \\ 0.06 & 0.09 & -2.59 & -0.78 & -2.25 & 0.30 & -0.24 & -1.59 \\ 0.02 & -0.26 & 0.31 & -2.25 & -0.24 & -2.60 & 0.15 & 0.15 \\ -0.00 & 0.27 & -0.15 & 0.30 & -2.60 & 0.27 & -2.65 & -0.01 \\ 0.16 & -2.23 & 0.32 & -0.24 & 0.15 & -2.65 & 0.28 & 0.02 \\ -0.01 & 0.06 & -0.03 & -1.59 & 0.15 & -0.01 & 0.02 & -3.58 \end{pmatrix} \tag{E.3}$$

Matrices of the para-BDT

$$H_{\text{Para}}^{\text{U}_\text{B}=0V} = \begin{pmatrix} -3.05 & -1.80 & 0.03 & 0.04 & 0.04 & 0.03 & 0.07 & -0.01 \\ -1.80 & -0.40 & -2.54 & 0.19 & -0.32 & 0.19 & -2.54 & 0.04 \\ 0.03 & -2.54 & 0.13 & -2.87 & 0.19 & -0.20 & 0.36 & 0.04 \\ 0.04 & 0.19 & -2.87 & 0.14 & -2.54 & 0.36 & -0.20 & 0.02 \\ 0.04 & -0.32 & 0.19 & -2.54 & -0.39 & -2.54 & 0.19 & -1.80 \\ 0.03 & 0.19 & -0.20 & 0.36 & -2.54 & 0.13 & -2.85 & 0.08 \\ 0.07 & -2.54 & 0.36 & -0.20 & 0.19 & -2.85 & 0.12 & 0.03 \\ -0.01 & 0.04 & 0.04 & 0.02 & -1.80 & 0.08 & 0.03 & -3.02 \end{pmatrix} \tag{E.4}$$

$$H_{\text{Para}}^{\text{U}_\text{B}=1V} = \begin{pmatrix} -2.70 & -1.79 & 0.03 & 0.04 & 0.04 & 0.03 & 0.07 & -0.01 \\ -1.79 & -0.30 & -2.54 & 0.19 & -0.32 & 0.19 & -2.54 & 0.04 \\ 0.03 & -2.54 & 0.18 & -2.87 & 0.19 & -0.20 & 0.36 & 0.04 \\ 0.04 & 0.19 & -2.87 & 0.06 & -2.54 & 0.36 & -0.20 & 0.02 \\ 0.04 & -0.32 & 0.19 & -2.54 & -0.53 & -2.54 & 0.19 & -1.80 \\ 0.03 & 0.19 & -0.20 & 0.36 & -2.54 & 0.05 & -2.85 & 0.08 \\ 0.07 & -2.54 & 0.36 & -0.20 & 0.19 & -2.85 & 0.17 & 0.03 \\ -0.01 & 0.04 & 0.04 & 0.02 & -1.80 & 0.08 & 0.03 & -3.42 \end{pmatrix} \tag{E.5}$$

$$H_{\text{Para}}^{\text{U}_\text{B}=3V} = \begin{pmatrix} -2.12 & -1.79 & 0.04 & 0.04 & 0.04 & 0.03 & 0.07 & -0.01 \\ -1.79 & -0.09 & -2.54 & 0.19 & -0.32 & 0.19 & -2.54 & 0.04 \\ 0.04 & -2.54 & 0.28 & -2.87 & 0.19 & -0.20 & 0.35 & 0.04 \\ 0.04 & 0.19 & -2.87 & -0.08 & -2.53 & 0.37 & -0.20 & 0.02 \\ 0.04 & -0.32 & 0.19 & -2.53 & -0.78 & -2.54 & 0.19 & -1.81 \\ 0.03 & 0.19 & -0.20 & 0.37 & -2.54 & -0.08 & -2.85 & 0.07 \\ 0.07 & -2.54 & 0.35 & -0.20 & 0.19 & -2.85 & 0.28 & 0.03 \\ -0.01 & 0.04 & 0.04 & 0.02 & -1.81 & 0.07 & 0.03 & -4.19 \end{pmatrix} \tag{E.6}$$

List of Figures

List of Tables

Bibliography

[1] Dong Xiang, Xiaolong Wang, Chuancheng Jia, Takhee Lee, and Xuefeng Guo. Molecular-scale electronics: From concept to function. Chem. Rev., 116(7):4318–4440, 2016.

[2] R Stadler, S Ami, C Joachim, and M Forshaw. Integrating logic functions inside a single molecule. Nanotechnology, 15(4):S115–S121, 2004.

[3] Marcus D Hanwell, Donald E Curtis, David C Lonie, Tim Vandermeersch, Eva Zurek, and Geoffrey R Hutchison. Avogadro: an advanced semantic chemical editor, visualization, and analysis platform. J. Cheminformatics, 4:17, 2012.

[4] M. A. Reed, C. Zhou, C. J. Muller, T. P. Burgin, and J. M. Tour. Conductance of a molecular junction. Science, 278(5336):252–254, 1997.

[5] M. Di Ventra, S. T. Pantelides, and N. D. Lang. First-principles calculation of transport properties of a molecular device. Phys. Rev. Lett., 84(5):979–982, 2000.

[6] Troels Markussen, Robert Stadler, and Kristian S. Thygesen. The relation between structure and quantum interference in single molecule junctions. Nano Lett., 10(10):4260–4265, 2010.

[7] Mads Brandbyge, José-Luis Mozos, Pablo Ordejón, Jeremy Taylor, and Kurt Stokbro. Density-functional method for nonequilibrium electron transport. Phys. Rev. B, 65:165401, 2002.

[8] Nick Papior, Nicolás Lorente, Thomas Frederiksen, Alberto García, and Mads Brandbyge. Improvements on non-equilibrium and transport green function techniques: The next-generation TRANSIESTA. Comput. Phys. Commun., 212:8–24, 2017.

[9] Jmol: an open-source Java viewer for chemical structures in 3D. http://www.jmol.org/.

[10] P. Hohenberg and W. Kohn. Inhomogeneous electron gas. Phys. Rev., 136(3B):B864–B871, 1964.

[11] W. Kohn and L. J. Sham. Self-consistent equations including exchange and correlation effects. Phys. Rev., 140(4A):A1133–A1138, 1965.

[12] Wolfgang Nolting. Grundkurs Theoretische Physik 7. Springer Spektrum. 8. Auflage, 2015.

[13] C M Goringe, D R Bowler, and E Hernández. Tight-binding modelling of materials. Rep. Prog. Phys., 60:1447–1512, 1997.

[14] Hermann Haken and Hans Christoph Wolf. Molekülphysik und Quantenchemie. Springer-Verlag Berlin Heidelberg. 5. Auflage, 2006.

[15] Peter G. Lykos and Robert G. Parr. On the pi-electron approximation and its possible refinement. J. Chem. Phys., 24(6):1166–1173, 1956.

[16] Per-Olov Löwdin. On the non-orthogonality problem connected with the use of atomic wave functions in the theory of molecules and crystals. J. Chem. Phys., 18(3):365–375, 1950.

[17] Dmitry A. Ryndyk. Theory of quantum transport at nanoscale. Springer International Publishing, 2016.

[18] M P Lopez Sancho, J M Lopez Sancho, and J Rubio. Quick iterative scheme for the calculation of transfer matrices: application to Mo(100). J. Phys. F: Met. Phys., 14:1205–1215, 1984.

[19] Michael Rumetshofer. First-principles molecular transport calculations. Master's thesis, Graz University of Technology, 2016.

[20] Magnus Paulsson. Non equilibrium green's functions for dummies: Introduction to the one particle NEGF equations. eprint arXiv:cond-mat/0210519v2 [cond-mat.mes-hall], 2006.

[21] Ryndyk D.A., Gutiérrez R., Song B., Cuniberti G. (2009) Green Function Techniques in the Treatment of Quantum Transport at the Molecular Scale. In: Burghardt I., May V., Micha D., Bittner E. (eds) Energy Transfer Dynamics in Biomaterial Systems. Springer Series in Chemical Physics, vol 93. Springer, Berlin, Heidelberg.

[22] Rui Li, Jiaxing Zhang, Shimin Hou, Zekan Qian, Ziyong Shen, Xingyu Zhao, and Zengquan Xue. A corrected NEGF + DFT approach for calculating electronic transport through molecular devices: Filling bound states and patching the non-equilibrium integration. Chem. Phys., 336:127–135, 2007.

[23] Kim G. L. Pedersen, Anders Borges, Per Hedegård, Gemma C. Solomon, and Mikkel Strange. Illusory connection between cross-conjugation and quantum interference. J. Phys. Chem. C, 119(48):26919–26924, 2015.

[24] José M Soler, Emilio Artacho, Julian D Gale, Alberto García, Javier Junquera, Pablo Ordejón, and Daniel Sánchez-Portal. The SIESTA method for ab initio order-N materials simulation. J. Phys.: Condens. Matter, 14(11):2745–2779, 2002.

[25] Nick Rübner Papior. Computational Tools and Studies of Graphene Nanostructures. PhD thesis, Technical University of Denmark, 2016.

[26] Eleftherios N. Economou. Green's Functions in Quantum Physics. Springer-Verlag Berlin Heidelberg, 3rd edition, 2010.

[27] Mariana M. Odashima, Beatriz G. Prado, and E. Vernek. Pedagogical introduction to equilibrium Green's functions: condensed-matter examples with numerical implementations. Rev. Bras. Ens. Fis., 39(1):e1303, 2017.

[28] M. Strange, I. S. Kristensen, K. S. Thygesen, and K. W. Jacobsen. Benchmark density functional theory calculations for nanoscale conductance. J. Chem. Phys., 128:114714, 2008.

[29] http://dipc.ehu.es/frederiksen/tstutorial/index.php/Au-BDT, December 2018.

[30] Walter A. Harrison. Electronic Structure and the Properties of Solids. W.H. Freeman and Comany, 1980.